ABSTRACT

CHADWICK, CHRISTOPHER T. Resonance Raman Spectroscopy Utilizing Tunable Deep Ultraviolet Excitation for Materials Characterization. (Under the direction of Dr. Hans D. Hallen).

Resonance Raman spectroscopy offers some key benefits over other spectroscopy methods. In one facet, resonance Raman provides a level of specificity not present in non-resonant Raman scattering. In another facet, resonance Raman can provide increased scattering cross-sections that rival those associated with the intensities of species fluorescence. These features provide mechanisms for improved trace species detection in current Raman remote sensing applications; as well as signal level enhancement in tiny volume regimes, such as those typical in near-field optical microscopy. This dissertation presents three main thrusts that are not well documented in the previous resonance Raman studies.

- We demonstrate fine resolution ($\sim 0.1\,nm$) resonance tuning of the excitation wavelength corresponding to sharp absorption bands in liquid benzene and liquid toluene. The Raman spectra for these materials show an appreciable increase in scattering intensity of fundamental vibrational modes and show significant enhancements in scattering intensities for overtone and combination vibrational modes not observed with non-resonant excitation. Resonantly excited fundamental modes are observed to be enhanced by 3 to 5 orders of magnitude over non-resonant excitation; and several resonantly excited overtone modes are observed for both liquid benzene and liquid toluene.
- We have observed, that for liquid benzene and liquid toluene, the maximum Raman scattering intensity is realized when the excitation wavelength corresponds to that of the vapor phase absorption maximum, not the liquid phase absorption maximum as expected. We present a simple model of the time-dependent energy accumulation in the scattering volume that suggests that the scattering medium is a highly disorganized fluid. The observed Raman scattering intensity originates from this metastable fluid observed during the liquid-vapor phase transition.

- Using different concentration solutions of liquid benzene in heptane, we illustrate the influence species absorption has on the potential level of signal enhancement offered by resonance Raman scattering. In low concentration environments, resonance Raman signal levels can be 1 to 3 orders of magnitude larger than those of non-resonant Raman. As concentration increases, the signal levels of both resonant and non-resonant Raman become comparable. Using the species absorption to normalize the number of scattering molecules, the resonance enhancement is shown to be 3 to 5 orders of magnitude over the non-resonant excitation.

Resonance Raman Spectroscopy Utilizing Tunable Deep Ultraviolet Excitation for Materials Characterization

by
Christopher Todd Chadwick

A dissertation submitted to the Graduate Faculty of
North Carolina State University
in partial fullfillment of the
requirements for the Degree of
Doctor of Philosophy

Physics

Raleigh, North Carolina

2009

APPROVED BY:

Dr. David E. Aspnes	Dr. Christopher M. Roland
Dr. Hans D. Hallen Chair of Advisory Committee	Dr. C. Russell Philbrick

DEDICATION

I dedicate this work to my family whose patience and support of my endeavors can never be justly rewarded.

May this proud accomplishment shine in the loving memory of:
Amanda Congleton Chadwick,
Guion Graydon Chadwick,
and
William Vance Fulford.

. . . you are greatly missed.

BIOGRAPHY

I was prematurely born in December 1976, on the 30^{th} in Morehead City, NC. Ask anyone in my family; this was one of the first and last times I was to be early. From what I can deduce, the year of 1976 was a mixed bag: the *Concorde*, the Ramones, Son of Sam, the *Face on Mars*, Jimmy Carter, *Hotel California*, Ebola.

I spent my early years in neighboring Beaufort, next door (if next door is a 15-minute walk) to my father's parents, tucked on the edge of the farm. Memorable moments include: cutting down a Dogwood tree in the front yard, using an icy ditch to learn how to ride a bike, hitting my brother with both a tennis racket and the heel of a cowboy boot, sticking a key into a live electrical socket (twice), learning origami, and moving about 4 hours northeast to Cape Hatteras, NC. Here I developed a skill for copying my brother, who I can say is responsible for helping develop my scientific interests.

Cape Hatteras offered a new set of memorable moments: developing a taste for travel with my grandmother Amanda, spending my first paycheck on a Swiss Army knife, cutting meat at Conner's with my brother during the summer, Hurricane Emily, and second and third degree improvised pyrotechnic burns which ultimately lead to a change in after school activities (music). After a brief stay in Charlottesville, VA during my junior year, I found way to Fuquay-Varina, NC to finish my last year of high school.

I graduated NC State University with a Bachelor of Science degree in physics in 2001 in the summer (that early problem again). While in undergraduate studies I had two significant opportunities: to spend 13+ years at WKNC-FM as an on-air DJ and join the NSOM Group working for Dr. Hans Hallen. The first resulted in a collection of approximately 4000 vinyl albums. The later, needless to say, lead to earning a Doctor of Philosophy degree in physics which will be the easiest thing move when my lease expires although, it certainly took much more work to obtain.

ACKNOWLEDGMENTS

I would like to take this opportunity to pay special tribute to some of the people I credit with assisting and supporting me during my graduate studies.

To my advisory committee (Dr. Hans Hallen, Dr. C. Russell Philbrick, Dr. Dave Aspnes, and Dr. Chris Roland) for your input on all phases of my work, and helping me sculpt this dissertation into a document I am proud to have authored. I extend a special thank you to Dr. Hallen for suggesting I take advantage of the opportunity to pursue my degree and for the innumerable skills I have managed to pick up while in his lab. I am certainly grateful for the patience, insights, and relaxed environment he made available in the Optics Lab. Also, a special thank you is extended to Dr. Philbrick for offering his experience, advice, and assistance in my work and for giving me the opportunity to work with Dr. Adam Willitsford.

To Dr. Adam Willitsford for his friendship, sense of humor, and dedication in our research efforts and extra-curricular activities. Many weights lifted, tennis balls relocated, and Mexican Feasts devoured, all to remove the fatigue of the mind numbing $10\,Hz$ ticking and long hours standing making nanometer size adjustments. The times, good and bad, have found a permanent residence in the memories brother; it was a pleasure to work with you and I trust we will in the future.

To two outstanding individuals I am honored to call colleagues, Dr. Mike Taylor and the soon to be anointed Dr. Bev Clark: we share a common history in the Optics Lab: same roads traveled, same trials and tribulations in obtaining these degrees. A sort of battle-hardened, band of brothers and I feel that our paths will be interlaced to the end.

To the illustrious members of the NCSU Optics Group both current and former: especially to Trey Walker, Ryan Neely, Jeremy Peters for the stimulating conversions on politics, society, music, and markets.

To the two women who kept the Physics Department's gears well greased (at least from my perspective); Ms. Jenny Allen for her seemingly infinite scope of graduate school information and Ms. Rebecca Savage for the extra steps she took to help me with the details of dealing with the powers that be.

To the very talented crew of the PAMS College Instrument Shop, most notably Frank and Tim whom I talked with most concerning the contraptions we managed to devise

in the Optics Lab.

To the several accomplished and learned scientists I had the opportunity with which to discuss my dissertation work; Dr. Stewart Kurtz (Penn State University) and Dr. Ray Tsu for their unique affinity for benzene, Dr. Sanford Asher (University of Pittsburgh) and Dr. Arthur Sedlacek (Brookhaven National Lab) for sharing their experiences with and knowledge of the phenomenon of resonance Raman scattering.

To Dr. Diane Knight for her generosity in loaning Adam and myself the diamond sample used in our work.

To Michigan Aerospace Corporation for their loan of the ANDOR CCD camera and Dr. Rob Nemanich (Arizona State University) for his loan of the SPEX spectrometer system.

To "Dr." Lynell Williamson for sharing his wisdom and friendship during my tenure at Amedeo's Italian Restaurant and his open door at the College of Textiles where I found myself occasionally exchanging the gossip of the day.

To Mr. Amedeo DeAngelis, who I had the opportunity to work for during much of my undergraduate and graduate studies; I found many lessons on responsibility and ethics inside those walls at 3905 Western Blvd.

To my confederates, Brian Harris and Ervin Brandon, the friendship is beyond the capability of describing; you gentlemen are truly part of my family.

And to Angie, you are a very, very special woman to me... distant lover... I love you ...

TABLE OF CONTENTS

LIST OF TABLES . . . . . **ix**

LIST OF FIGURES . . . . . **xi**

1 Introduction **1**
1.1 Overview 1
1.2 Goal of This Work 2

2 Background **5**
2.1 Overview 5
2.2 Survey of Previous Work 5
2.3 Historical Notes on the Raman Effect 9
2.4 Optical Scattering Phenomena 10
2.5 Raman and Resonance Raman Scattering 15
2.6 Forms of the Polarizabiltiy Tensor 19
2.6.1 General Form of the Polarizability Tensor 20
2.6.2 Improving the Polarizability Tensor 22
2.7 Polarizability for Resonance Raman 23
2.7.1 A-Term Contribution 23
2.7.2 B-Term Contribution 25
2.7.3 C- and D-Term Contributions 26
2.8 Considerations Relative to this Study 26

3 Instrumentation **29**
3.1 Overview 29
3.2 General Apparatus 29
3.2.1 Sample Positioning 29
3.2.2 Spectrometer Coupling 30
3.2.3 Other Sample Control 33
3.3 Data Acquisition 34
3.4 Optical Parametric Oscillator 35
3.4.1 Phase-Matching Conditions 36
3.4.2 Nonlinear Crystal Properties 37
3.4.3 Angular Tuning Curves 40
3.4.4 Output Characteristics 41
3.5 Spectrometer Model 45
3.5.1 Overview 45
3.5.2 Spectrometer Characterization and Specifications 45
3.5.3 Lens and Mirror Considerations 49
3.5.4 Diffraction Grating Considerations 50

3.5.5 Camera Considerations . . . 52
3.5.6 Final Spectral Efficiency Results . . . 53

4 Methods . . . 54
4.1 Overview . . . 54
4.2 Image Processing . . . 54
4.3 Absorption Correction Model . . . 57
4.4 Discussion of Experimental Uncertainties . . . 60
4.5 Peak Classification . . . 63

5 Overview of Key Experimental Spectra . . . 68
5.1 Overview . . . 68
5.2 Diamond Raman Spectra . . . 69
5.3 Benzene Absorption and Raman Spectra . . . 71
5.4 Toluene Absorption and Raman Spectra . . . 79
5.5 Raman Spectra of Benzene-Heptane Solutions . . . 84

6 Resonance Raman Scattering from Vapor-Phase Absorption in Liquids . 86
6.1 Overview . . . 86
6.2 Laser Induced Bubble Formation . . . 87
6.3 Metastable Phase Model . . . 91
6.4 Mass Spectroscopy Examination and Results . . . 94

7 Utility and Limitations of Resonance Raman Scattering . . . 99
7.1 Article Abstract . . . 99
7.2 Article Introduction . . . 100
7.3 Experimental Description . . . 101
7.4 Results and Discussion . . . 102
7.5 Conclusions . . . 108

8 Conclusion . . . 109
8.1 Future Work . . . 111

Bibliography . . . 113

Appendices . . . 129

A Electronics Designs . . . 130
A.1 NSOM probe signal integrator/peak-hold schematic and PCB . . . 132
A.2 Photodiode discriminator schematic and PCB . . . 133
A.3 Adjustable digital pulse delay schematic and PCB . . . 134

B Mechanical Designs . . . 136
B.1 Stainless steel vapor cube . . . 137
B.2 PTFE sample holder base . . . 138
B.3 ANDOR to SPEX camera adapter . . . 139

B.4 Aluminum base plate for Faraday box 140
B.5 Copper Faraday box input panel 141
B.6 Toy motor mounting bracket for vacuum deposition system 142

LIST OF TABLES

Table 2.1 Intensity cross-section magnitudes, $d\sigma/d\Omega$, for different optical interaction mechanisms. 12

Table 3.1 Summary of calculated coupling optics parameters. 31

Table 3.2 Comparison of SBIG and ANDOR camera parameters. 35

Table 3.3 BBO crystal parameters for the NCSU OPO system. 41

Table 3.4 Values of d_{eff} for BBO and KDP for common phase-matching schemes under Kleinman symmetry approximation. 42

Table 3.5 SPEX Triplemate 1877 spectrometer specifications utilized in the spectral efficiency estimate, from [Spex, 1985]. 46

Table 3.6 Alternate configuration specifications for the Spex Triplemate 1877 with ANDOR camera adaptation. 49

Table 3.7 Calculated mirror and lens parameters. 51

Table 3.8 Summary of the estimated spectrometer spectral efficiency (η) statistics. ... 53

Table 4.1 Calculated effective path length, EPL_d, for liquid benzene and liquid toluene for resonant (R) and non-resonant (NR) excitation. 60

Table 4.2 Summary of experimental uncertainties. 61

Table 4.3 Concentrations, absorption coefficients, and effective path lengths with calculated uncertainties for different liquid benzene in heptane solutions. 64

Table 5.1 Vibrational assignments for the experimental Raman spectra of liquid benzene, in Herzberg notation. 78

Table 5.2 Vibrational assignments for the experimental Raman spectra of liquid toluene, in Herzberg notation. 83

Table 5.3 Summary of benzene solution concentrations and excitation wavelengths. .. 84

Table 6.1 List of acoustic model parameter definitions and physical constants. 89

Table 6.2 List of calculated bubble acoustic model parameters. 90

Table 6.3 Estimated number densities and mean free paths for benzene, toluene, and air. 93

Table 6.4 Calculated penetration depth for experimental excitation wavelengths and average laser power in pure liquid benzene. 94

Table A.1 Electronics bill of materials associated with the three prior schematic and PCB designs. 135

LIST OF FIGURES

Figure 2.1 Jablonski energy transfer diagrams for Rayleigh, Raman, and fluorescence optical processes. 13

Figure 2.2 Relationship between the Rayleigh and Raman spectral peaks showing the rotational sidebands that straddle the more intense Rayleigh and vibrational Raman peaks. 14

Figure 2.3 Illustration of the Franck-Condon effect in a two state scattering system. . 25

Figure 2.4 90 degree Raman scattering configuration showing how the observed signal originates from a spatial average of a random ensemble of scattering agents. 27

Figure 3.1 Illustration of the typical experimental configuration. 30

Figure 3.2 Schematic used for calculating the coupling optics' parameters. 31

Figure 3.3 Schematic of the NCSU OPO system. 36

Figure 3.4 Illustration of uniaxial nonlinear crystal conventions. 38

Figure 3.5 Sellmeier's dispersion for KDP (left) and BBO (right) between 190 nm and 800 nm. Shaded regions indicate values conducive to phase-matching. 39

Figure 3.6 Theoretical angular tuning curve for BBO in the Type I (ooe) phase-matching scheme. 41

Figure 3.7 Theoretical power conversion efficiency of KDP and BBO for different incident power densities and crystal lengths. 43

Figure 3.8 Configuration of the Type I phase-matching OPO cavity of the NCSU OPO system. 44

Figure 3.9 The NCSU OPO system in operation. The Nd:YAG laser and SHG/THG system are on right concealed by protective fabric. 44

Figure 3.10 Schematic of the SPEX Triplemate 1877 spectrometer. M, L, and G represent the mirrors, lenses, and gratings respectively. 46

Figure 3.11 Angle conventions for the Czerny-Turner configuration. The angles of incidence (i) and diffraction (r) are both positive angles referenced from the grating normal, $n_{grating}$. 47

Figure 3.12 Dependence of the linear dispersion on turret angle for a 2400 gr/mm grating, an instrument angle $\phi \approx 13°$, and diffraction order $m = 1$. 48

Figure 3.13 Variation of field of view with wavelength for a 2400 gr/mm grating, an instrument angle $\phi \approx 13°$, and diffraction order $m = 1$. 49

Figure 3.14 Estimated reflectance profile for an anti-reflection coated aluminum mirror. 50

Figure 3.15 Estimated transmittance profile for an anti-reflection coated fused silica lens. 51

Figure 3.16 Spectral efficiency profiles for the filter and main stage diffraction gratings. 52

Figure 3.17 ANDOR camera CCD array quantum efficiency. 52

Figure 3.18 Estimated total spectral efficiency of the SPEX spectrometer system. 53

Figure 4.1 Unprocessed ANDOR camera image of the $\sim 1332\,cm^{-1}$ Stokes Raman line of diamond for 240 nm excitation. Intensity scales from red (min) to white (max). 55

Figure 4.2 Configuration and conventions for calculating the Beer-Lambert-Bouguer Law attenuation of the excitation and scattered light. 58

Figure 4.3 Detector polarization state for randomly polarized (left) and horizontally polarized (right) incident light. 59

Figure 4.4 Illustration of spectral peak area (shaded region) calculation for resonant and non-resonant artificial data series. 65

Figure 4.5 Bandwidth of the NCSU OPO system in wavelength (left) and wavenumber (right) as indicated by the manufacturer. 66

Figure 4.6 Illustration of different classification schemes for spectral features without instrument slit function and excitation laser lineshape information. 66

Figure 5.1 Diamond Stokes Raman spectra for three excitation wavelengths. 71

Figure 5.2 Integrated intensity of the Stokes Raman band at $1332\,cm^{-1}$ for diamond for various excitation wavelengths. Solid line: absorption coefficient (scaled $10\times$), from [Edwards and Philipp, 1985]. The A indicates the band gap edge at $\sim 5.5\,eV$. 72

Figure 5.3 Photograph of diamond specimen, under magnification, showing internal contamination. 73

Figure 5.4 Eztkorn, Inagaki, and API ultraviolet absorption spectra for benzene. 74

Figure 5.5 Absorption region of interest from Figure 5.4. 74

Figure 5.6 Stokes Raman spectra for liquid benzene for near resonance and off resonance wavelength excitations. 75

Figure 5.7 Full Stokes Raman spectra for pure benzene with 430 nm and 259 nm excitation wavelengths. 77

Figure 5.8 Eztkorn and API ultraviolet absorption spectra for toluene. 80

Figure 5.9 Absorption region of interest from Figure 5.8. 80

Figure 5.10 Stokes Raman spectra for liquid toluene for near resonance wavelength excitations. 81

Figure 5.11 Full Stokes Raman spectra for pure toluene with 266.83 nm and 430 nm excitation wavelengths. 82

Figure 5.12 Stokes Raman spectra for various concentrations of benzene in heptane solution for 258.88 nm resonant excitation. 85

Figure 6.1 Schematic of the liquid-vapor-window interface region. 88

Figure 6.2 Time evolution of the energy deposited into the effective volume of pure toluene for average laser power of 1 mW and pulse width of 8 ns for several excitation wavelengths. 95

Figure 6.3 Time evolution of the energy deposited into the effective volume of pure toluene for average laser power of 1 mW and pulse width of 8 ns for several excitation wavelengths. 95

Figure 6.4 Time evolution of the energy deposited into the effective volume of pure toluene for average laser power of 1 mW and pulse width of 8 ns for several excitation wavelengths. 96

Figure 6.5 Time evolution of the energy deposited into the effective volume of benzene for the experimental values in Table 6.4. 96

Figure 7.1 Solid points connected by dashed line: integrated Stokes Raman intensities for diamond, centered on 1332 cm^{-1} as the excitation is tuned from 215 nm to 235 nm in 1 nm steps and to 300 nm in larger steps. Solid line: absorption coefficient (scaled 10×), from [Edwards and Philipp, 1985]. The A indicates the band gap edge at $\sim 5.5\,eV$. 103

Figure 7.2 Stokes Raman spectra for pure liquid benzene, centered on $\sim 992\,cm^{-1}$. Tuning from $258.5\,nm$ to $259.5\,nm$, excitation wavelength indicated left of the spectra. 104

Figure 7.3 Two methods of quantifying resonance gain. Top: integrated Stokes Raman intensities for benzene in heptane at various concentrations for different excitation wavelengths adjusted only for instrument variation. This is referred to the 'raw' or real measured signal. Bottom: integrated Stokes intensities where both the instrument variation and species self-absorption are corrected. 106

Figure 7.4 The ratio of all integrated intensities to the non-resonant integrated intensity across concentration provides a normalized indication of signal gain. Left: indicates the real measured signal gain by adjusting only for the instrument variation. Right: also adjusts for the species self-absorption for cross-section comparison. The arrow indicates a point outside of the vertical scale. 107

Chapter 1

Introduction

1.1 Overview

Resonance Raman spectroscopy has become an important research tool in the investigation of molecular species. When the excitation light incident on the molecule is within an absorption band for the molecule, the Raman scattering intensity for vibrational and rotational modes in the system may exhibit significant increases in amplitude. The enhancement of the Raman signal can increase several orders of magnitude over that for non-resonant excitation [Asher, 1993a; Kudelski, 2008; Clark and Dines, 1986]. There are some key motivating features of resonance Raman scattering.

- The larger per molecule scattering cross-section offered by resonance enhanced Raman scattering provides appreciable signal to noise ratios for smaller populations of active scattering centers. This gain in signal compared to non-resonant Raman scattering suggests the direct application of resonance Raman to low concentration and tiny sampling volume environments. The study of these environments typically suffers from the smaller scattering intensities resulting from non-resonant Raman scattering; these can be too small to be useful.

- For the excitation wavelengths between $\sim 210\,nm$ and $\sim 450\,nm$, Raman scattering results from the excitation of the system from lower vibrational levels in the electronic ground state. However when the excitation source is near an electronic absorption band, the scattering probability is enhanced by interaction with lower levels of the

first excited electronic state. Due to the spacing of vibrational levels in the potential well, the resonant Raman scattering provides additional information about specific levels in the excited state unavailable with non-resonant Raman scattering [Hirakawa and Tsuboi, 1975; Haar, 1946].

- This work utilizes an deep ultraviolet (DUV) excitation source. Ultraviolet resonance Raman scattering is advantageous for a few reasons. Visible excitation Raman studies suffer from sample and matrix fluorescence that can dominate the Raman scattering intensity. Ultraviolet excitation at shorter wavelength escapes the issue of species fluorescence since many materials do not exhibit significant fluorescent emission at wavelengths below $280\,nm$ [Asher and Johnson, 1984]. Also many materials have interesting electronic absorption features within the DUV region that can potentially yield resonance enhancement [Jones et al., 1985; Gerrity et al., 1985].

1.2 Goal of This Work

The goal of this dissertation is to present three major findings not explored in the previous investigations of resonance Raman scattering.

- The bulk of resonance Raman studies utilize discrete, widely spaced excitation wavelengths [Jones et al., 1985; Efremov et al., 2008]. Early studies used widely spaced wavelengths associated with available laser light sources. Dye laser sources offered expanded ranges of wavelengths [Asher et al., 1983]. Few previous studies utilize continuously tunable excitation sources and fewer still utilize continuously tunable ultraviolet excitation. These studies are limited to small wavelength intervals ($\sim 3\,nm$), which limited the exploration of absorption features [Ziegler, 1987]. To our knowledge, studies utilizing continuously tunable ultraviolet excitation from $\sim 210\,nm$ and $\sim 400\,nm$ are non-existent in the current literature. Our work serves to initiate resonance Raman studies utilizing widely continuously tunable ultraviolet excitation. The benefit of wide excitation tunability is not trivial. Within our tuning range we have been able to obtain vibrational Raman spectra for liquid benzene and liquid toluene while tuning through significant features in their respective absorption spectra. Prior investigations of benzene have been limited to large steps in excitation wavelength

for the near-ultraviolet to ultraviolet region ($> 210\,nm$) [Asher and Johnson, 1985] or has examined higher energy absorption systems in the molecules ($< 210\,nm$) [Ziegler and Hudson, 1981; Ziegler and Albrecht, 1979]. Our studies of the $260\,nm$ absorption system in liquid benzene and the $267\,nm$ absorption system in liquid toluene have obtained vibrational Raman scattering profiles across complete absorption bands.

- Previous resonance Raman studies relied on a dynamic sample space; where a liquid sample is flowing or circulating through the interaction region [Asher, 1993a,b]. The primary reason for a dynamic sample is to avoid localized sample photo-degradation due to high pulse energy laser excitation [Chen et al., 1997; Sedlacek et al., 2001]. Our configuration utilizes stationary sample species. We have observed that when the excitation wavelength is within $\pm 0.5\,nm$ of a sharp absorption band for vapor phase benzene, the resonance Raman scattering intensity for our liquid phase benzene sample is at its maximum. Comparison of the vapor phase and liquid phase absorption profiles show a separation of approximately $2\,nm$ to $3\,nm$. Thus, we are certainly observing the most intense resonance enhancement in liquid samples, occurring at the absorption maxima of its vapor phase. This behavior is also observed in liquid toluene. To explain this interesting and unexpected behavior, we have considered a simple model to describe the time evolution of the energy deposited into the sampling volume. The model suggests, that in the spectrally narrow and highly absorbing region at the absorption band peak, the energy deposited into the sample volume is sufficient to promote a liquid-to-gas phase change in the sample. The phase change is distinctive and associated with audible acoustic shocks detected when the excitation wavelength is tuned to the vapor absorption peak. Additionally a simple model is considered to describe the acoustic observations.

- Resonance Raman scattering occurs only in the sharp or high intensity absorption bands. A drawback of this requirement is the absorption may be sufficiently intense to limit the Raman signal due to the high local absorption of the system. We have observed a trade-off between the heavy absorption and the enhancement gain by examining different concentrations of liquid benzene in heptane and naphthalene solutions. Our trials with liquid benzene in heptane suggest that when the solution

concentration is high, the enhancement gain for resonance excitation is comparable to the signal levels observed for non-resonant excitation. However when the solution concentration is low, the resonance enhancement gain is approximately 3 to 4 orders of magnitude over that observed with non-resonant excitation. In naphthalene, where the absorption is approximately 30 times stranger than that of benzene, we were unable to detect any resonance signal for our lowest milli-molar concentrations, confirming our observations in benzene. These results provide a basis to determine when and in what environments resonance Raman scattering can be useful. This study addresses a void in the previous resonance Raman work; when and under what conditions is the resonance Raman process useful.

Additionally, the experimental apparatus, image processing, and analysis algorithms are described. One of the primary contributions of this work is utilizing a continuously tunable ultraviolet excitation source - an optical parametric oscillator (OPO). Fundamentals of our OPO system are thoroughly discussed in Chapter 3. Our image processing methodology required an additional parameter not initially obtained from the experimental apparatus. The spectrometer spectral efficiency is required to normalize the collected sample spectra. A simple model to estimate our spectrometer spectral efficiency is presented in Chapter 3. The image processing methodology is outlined in Chapter 4 with emphasis on significant processing algorithms. The pulse energy deposition model and resonance gain calculations are described using our simple absorption correction model discussed in Chapter 4. Finally, sources of experimental uncertainties are discussed in Chapter 4. Key experimental absorption and Raman spectra are presented in Chapter 5. Also preliminary vibrational Raman spectral assignments are tabulated and compared with established assignment values from the literature and presented.

Chapter 2

Background

2.1 Overview

This chapter presents some of the major theoretical concepts of optical scattering, the Raman and resonance Raman effects, and molecular spectroscopy. Important aspects of historical and current work in Raman and resonance Raman scattering will be outlined. The mathematical framework used to describe resonance Raman scattering is discussed, and limitations of this mathematical description are addressed in relation to this study.

2.2 Survey of Previous Work

The techniques and application of Raman and resonance Raman spectroscopy have been employed in a wide breadth of study since the early 20^{th} century. Early resonance Raman studies were almost exclusively theoretical primarily due to the lack of powerful and narrow bandwidth light sources. Laser light sources have increased the usefulness of Raman and resonance Raman spectroscopy techniques for various research fields spanning chemistry, biochemistry, physics, atmospheric and meteorological science, and remote sensing.

Efremov et al. [Efremov et al., 2008] summarizes many of the recent developments of resonance Raman spectroscopy. These developments comprise studies in biological materials specifically plant carotenoids, proteins, nucleic acids, drug interactions, and metalloproteins, carbon nanotubes, liquid chromatography, capillary electrophoresis, archaeological

artifacts, and minerals as well. Also methodological and instrumentation innovations are introduced with attention to utilizing fiber-optic probes for a highly portable and stable apparatus. All of these techniques can benefit from resonance Raman enhancements due to the small analyte concentrations, where non-resonant Raman scattering intensity is too small to be useful.

Resonance Raman scattering is by nature a result of relaxation from a level inside an excited electronic state. Browne and McGarvey [Browne and McGarvey, 2007] outline several regimes of resonance Raman for explaining different excited electronic state structure. *Transient resonance Raman* uses single laser pulses to both excite and probe the excited states and by controlling the pulse power, information can be extracted about the excited states since the level and state populations can be adjusted with different incident light pulse powers. With *time-resolved resonance Raman* an initial pumping pulse is introduced to put the system into an excited state followed by an additional weaker pulse (which may or may not be of the same wavelength) used to probe the time evolution of the levels and states. These techniques exploit the availability of electronic information inherent in resonance Raman. This type of information is not present in non-resonant Raman studies.

Resonance Raman has found extensive application in various biological and biochemical studies. The appeal of resonance Raman in these studies is due to the resonance signal enhancement in low concentration environments. Much of the work in biological samples is confined to the visible and infrared portions of the spectrum, where many analytes exhibit absorption resonances in these wavelengths; including materials such as metalloporphyrins, heme systems, and enzymes [Browne and McGarvey, 2007; Clark and Dines, 1986; Spiro and Strekas, 1974; Belyea et al., 2006]. These studies utilize pre-resonance enhancement of the Raman signal; however, with excitation wavelengths in the visible and infrared, they do not yield as detailed electronic state information as available in ultraviolet excitation. Conversely, DNA, RNA, and other nucleic acids have absorption resonances in the ultraviolet thereby allowing for ultraviolet resonance Raman studies [Benevides et al., 2005; Toyama et al., 1996, 2005; Dudik et al., 1985]. These absorption resonances have permitted the spectral fingerprinting of bacteria using ultraviolet resonance Raman [Grun et al., 2007; Jarvis and Goodacre, 2004]. One of the drawbacks to visible and infrared ex-

citation is due to sample and/or sample matrix fluorescence interference that may exceed the available Raman signal intensity [Asher, 1984]. The utilization of ultraviolet excitation can minimize or eliminate this interference.

Saariaho et al. [Saariaho et al., 2005] utilize ultraviolet resonance Raman to determine the amount of lignin (a biopolymer binding agent in wood) retained in wood pulp residues from the defibration and subsequent bleaching of the remaining fibers in the production of paper. Lignin has unique spectral features that exhibit resonance enhancement, which coupled with the complex chemical nature of wood pulp residues allows resonance Raman to be utilized as a production level tool in the evaluation of pulp quality. Recently Oladepo and Loppnow [Oladepo and Loppnow, 2008] have utilized ultraviolet resonance Raman for *in situ* studies of sunscreens appealing to the selective enhancement of the Raman signal above that of the sample matrix and fluorescence. Due to the minimal sample preparation requirements, which are unique to Raman spectroscopies, these studies suggest the ease and viability of a highly reliable means of production line quality control.

Resonance Raman has been utilized in the study of excited electronic state properties in solid state materials. Yaman et al. [Yaman et al., 2000] have observed resonant Raman scattering in SiO_2 at $288.2\,nm$ utilizing a broadband ($200\,nm$ to $700\,nm$) flash lamp source. Szczepanski et al. [Szczepanski et al., 2001] examine linear clusters of carbon atoms in solid argon by using resonance Raman as a means of identifying the number of carbon atoms as a function of wavelength based on the spectral features associated with the electronic transitions of the aggregate carbon clusters. Diamond has a considerable tenure in studies of its Raman features and is used as a reliable reference and calibration sample. Raman [Raman, 1956] observed its characteristic lone Raman line at $1332\,cm^{-1}$. Calleja et al. [Calleja et al., 1978] have observed significant resonance enhancement in the second-order Raman intensity, not the first-order Raman intensity for diamond, at various wavelengths approaching its fundamental band gap of approximately $220\,nm$.[1] We have extended this wavelength range into the ultraviolet, observing the quenching of the first-order Raman signal while tuning the excitation wavelength from approximately $300\,nm$ to $210\,nm$ in $1\,nm$ steps.

[1]Here first-order signifies photons scattered at $1332\,cm^{-1}$ and second-order signifies photons scattered at $2664\,cm^{-1}$.

Resonance Raman spectroscopy has become a valuable research tool for the petroleum and hydrocarbon industry [Grasselli et al., 1981]. Asher and Johnson [Asher and Johnson, 1984] have applied ultraviolet resonance Raman to examine and classify the constituent components of liquefied coal. This study was one of the first to document the reduced fluorescence interference from the sample and sample matrix, together with simultaneous resonance enhancement in a low concentration environment. Subsequent work from Jones et al. [Jones et al., 1985] has also verified these findings, demonstrating that these features permit significant benefits when using resonance Raman.

Additional work by Asher [Asher, 1984] has shown the benefits of fluorescence reduction and low concentration enhancement for the detection of polycyclic aromatic hydrocarbons using different excitation wavelengths, and we have extended this study to the utilization of a continuously tunable ultraviolet source in similar compounds. Hydrocarbon studies establish precedence in the resonance Raman studies for similar enhancements using the chemical bonding structures in explosive compounds such as trinitrotoluene (TNT), trinitrobenzene (TNB), and ammonium nitrate-fuel oil (ANFO) mixtures. These and related materials are of obvious interest to defense and security industries. Resonance Raman enhancement serves to expand remote sensing capabilities. Lacey et al. [Lacey et al., 1997] have used ultraviolet resonance Raman in detecting trace residues of TNT in a solid matrix, demonstrating the feasibility of detection of trace amounts of TNT in other situations. Blanco et al. [Blanco et al., 2006] have examined the Raman spectra of varying concentrations of the explosives dinitrotoluene (DNT), pentaerythritol tetranitrate (PETN), and triacetone triperoxide (TATP) in sand for applications in land mine detection. Examination of their published work shows possible resonance enhancements in PETN in the $1200\,cm^{-1}$ to $1700\,cm^{-1}$ range, and TATP in the $300\,cm^{-1}$ to $500\,cm^{-1}$ and $1500\,cm^{-1}$ to $1600\,cm^{-1}$ ranges, which they do not mention. Our investigations suggest that additional insights on these materials may be gained for remote sensing utilizing resonance Raman techniques.

Because of the small concentrations of scattering centers in the vapor phase compared to liquid and solid state regimes, resonance Raman is expected to provide opportunities for atmospheric and environmental measurement techniques and remote sensing applications. Use of the resonance enhancements in the improvement of light ranging and

detection (LIDAR) techniques has been under investigation for some time. Rosen et al. [Rosen et al., 1975] propose the use of resonance Raman enhancement in detecting atmospheric pollutants using the enhanced scattering cross-sections observed in sulfur and nitrogen dioxide, and suggest similar enhancements for several diatomic species although they present these without confirmation by a LIDAR system.

Chen and Sedlacek [Chen and III, 1996], Sedlacek et al. [Sedlacek et al., 1994], and Chen et al. [Chen et al., 1997] have utilized a standard Raman LIDAR system to observe resonance enhancement in low concentration atmospheric pollutants, such as sulfur dioxide, carbon tetrachloride, iodine, and nitrobenzene with two to four orders of magnitude enhancement using a tunable laser source from $270\,nm$ to $560\,nm$. While this work has utilized a tunable excitation light source, the spacing resolution of these wavelengths is larger than $\pm 1\,nm$ and the tuning range is limited to the longer wavelength ultraviolet into the visible. Recently Johansson et al. [Johansson et al., 2008] has proposed the use of ultraviolet resonance Raman for stand-off detection of roadside bombs and improvised explosive devices. One of the significant issues they acknowledge is the low signal to noise ratio in the application of resonance Raman due to the high absorption of the species under investigation. Later in this work, some observations on the trade off between the potential enhancement available and the absorption needed to have a significant enhancement are presented.

2.3 Historical Notes on the Raman Effect

The Raman effect is attributed to the Indian scientists C. V. Raman and K. S. Krishnan; however, there is some dispute involving a nearly simultaneous discovery by the Russian scientists G. Landsberg and L. Mandelstam as to which group was deserving of the title of first discoverer. In an elegantly simple paper published in *Nature* in 1928 Raman and Krishnan described the discovery of a *new type of secondary radiation* emerging from various illuminated samples [Raman and Krishnan, 1928]. Motivation to search this for new radiation was founded in A. H. Compton's work in X-ray scattering, specifically the observation that X-rays when scattered from matter emerge with less energy. Raman and Krishnan immediately identified some of the characteristics of both Raman scattered light

and the idiosyncrasies encountered in its detection. They observed that: *a*) the generation of the new radiation requires intense illumination, *b*) the scattered intensity is significantly smaller than that of the incident radiation, *c*) the frequency is shifted with respect to the incident radiation's frequency, *d*) the new radiation is distinguished from a fluorescence due to its weak intensity and similar polarization to the incident radiation, and *e*) the intensity from gases and vapors is much more weak than that scattered from liquids.

The light sources available at the time of Raman and Krishnan's discovery proved very limiting to the use of Raman scattering.[2] The introduction of the laser approximately 35 years later would rapidly expand the field of Raman spectroscopy, whereas infrared techniques had dominated the theater of spectroscopy in prior years [Anderson, 1971]. As indicated in Raman and Krishnan's initial paper, the effect is realized in many materials owing to specific molecular properties of the material giving unique optical fingerprints, which are complimentary to those available from other spectrographic characterizations. Excellent discussion on the historical aspects of the Raman effect are given in Anderson [Anderson, 1971] and Long [Long, 1977] without unnecessary mathematical rigor, and in the original work by Raman and Krishnan [Raman and Krishnan, 1928].[3]

2.4 Optical Scattering Phenomena

The Raman effect is an optical scattering phenomenon characterized as an inelastic interaction of light with matter. In Raman scattering, an incident photon interacts with a molecular bond, either gaining or losing a quantum of energy dependent on the characteristics of the interacting bond, and emerges as this energy-shifted photon. By comparison, an elastic interaction with the molecular bond do not result in any energy change of the incident photon; these regimes are typically associated with Mie and Rayleigh scattering. Specular reflection, the blue color of the sky, observation of particulates in the air (clouds and smoke) are examples of these scattering mechanisms. Fluorescence and phosphorescence, while emission processes, are also inelastic processes observed in conjunction with

[2] A quick estimate of the intensity they used in their experiment suggests, given their description, that they had an increase in power density of approximately 2100 times at the point of sample illumination estimated from $M = -f_2/f_1$, with f_i the lens focal lengths, and considering the ratio of the pupil areas on each end of their telescope.

[3] While Raman scattering has proved to be invaluable, it is a surprisingly small, albeit significant, portion of C. V. Raman's work in the sciences.

Raman and Rayleigh scattering.

The classical description of optical scattering is that of an induced electric and magnetic dipoles (or higher order multipoles) which can oscillate with the same frequency (elastic) or at a shifted frequency (inelastic) with respect to the incident fields. Depending on the relative sizes of the scattering system compared to the incident wavelength, the scattered radiation will have a certain character compared to the incident. When the scattering system's dimensions are larger than the excitation wavelength, the induced dipoles will be of assorted oscillation frequencies resulting in broad spectrum scattered light. Large particulates such as water, aerosols, and smoke particles result in white scatter as observed in clouds. This larger particle scattering regime is known as Mie scattering. Although technically, the Mie scattering formulation is developed using a spherical particle assumption. Due to the large particle size and excitation of multiple frequency dipoles, Mie scattering is usually not as heavily dependent on the frequency as other scattering processes [Born and Wolf, 1980; Hecht, 2002].

As the scattering system's dimensions approach scales smaller than the wavelength of the incident photon, the induced dipoles' frequencies are limited to discrete values excited by the incident photon frequency, possibly harmonics of the excitation frequency, and the effect of any permanent dipole present in the system. The dependence of the scattering dipole intensity on the excitation frequency becomes obvious and, as observed by Rayleigh [Rayleigh, 1871], varies proportionally to the forth power of incident frequency, ω^4 for particles much smaller than the wavelength. The scattering intensity from an electric dipole moment, $\mathbf{p}$, oscillating at ω, can be expressed as its time averaged Poynting vector, $\langle \mathbf{S} \rangle$,

$$\langle \mathbf{S} \rangle = \Big(\frac{p_0^2 \, \omega^4}{32\pi^2 \, \epsilon_0 \, c^3} \Big) \frac{\sin^2 \theta}{r^2} \, \hat{r}. \tag{2.4.1}$$

During the scattering process, the dipoles will either scatter light at the same frequency as the incident light (with a small shift due to the Doppler effect associated with the thermal distribution of the molecules),*Rayleigh scattering*, or may scatter light at a different frequency (associated with the energy exchange between the incident light and the molecule), *Raman scattering*. Raman scattered light is comprised of discrete wavelengths, considered instantaneous, and having a frequency shift from the incident frequency that is independent of the excitation. When the incident photon energy is sufficiently large enough to interact

with the electronic states of a molecule, the resulting photon is delayed and the process is either *fluorescence* or *phosphorescence*. Fluorescence and phosphorescence are emission phenomena and have broadband frequency content in the radiation they produce. The processes are characterized by exponentially decaying lifetimes and the frequency content of the radiation is dependent on the excitation frequency and electronic states of the molecule. Both of these properties distinguish fluorescence and phosphorescence from Raman scattering. Additionally, Rayleigh and Raman scattering demonstrate high degrees of polarization, whereas fluorescence and phosphorescence are randomly polarized.

Table 2.1 lists the cross-section magnitudes for the different optical scattering an emission regimes [Inaba, 1976].[4] Motivation for pursuing resonance enhancement in Raman scattering is clear in the comparison of the non-resonant Raman (NR) and resonant Raman (R) cross-section magnitudes with that of the cross-section of Rayleigh scattering in Table 2.1. The classical description of scattering is normally sufficient to describe Mie and

Table 2.1: Intensity cross-section magnitudes, $d\sigma/d\Omega$, for different optical interaction mechanisms.

Interaction	Process	Frequency Relation	Cross-Section (cm^2/sr)	Detectable Constituents
Scattering	Mie	$\omega_s = \omega_0$	$10^{-26} - 10^{-8}$	Particulate Matter
	Rayleigh	$\omega_s = \omega_0$	10^{-26} (NR) 10^{-23} (R)	Atoms & Molecules
	Raman	$\omega_s \neq \omega_0$	10^{-29} (NR) 10^{-26} (R)	Molecules (atoms)
Emission	Fluorescence	$\omega_s = \omega_0$ $\omega_s \neq \omega_0$	10^{-26} 10^{-24}	Atoms & Molecules
Absorption		$\omega_s = \omega_0$	10^{-20}	Atoms & Molecules

ω_s: Scattered Frequency, ω_0: Incident Frequency; NR: Non-Resonance, R: Resonance, from [Inaba, 1976]

Rayleigh scattering. When considering Raman scattering, the classical and semi-classical approaches are qualitatively sufficient. However to fully characterize Raman scattering within a system, quantum mechanics is required to relate the light interaction to molecular

[4]For optical cross-section, $\sigma(\theta, \phi) = d\sigma/d\Omega$, we consider the total scattered(emitted) power, $P_\Omega = (d\sigma/d\Omega)\, I_0$, where I_0 is the incident intensity, θ is the scattering(emission) angle, and ϕ is the polarization angle.

parameters.

Figure 2.1 depicts the scattering (or emission in the case of fluorescence) in the system originating from the energy exchange between a photon of energy $\hbar\omega_0$ and the system (e.g. molecular bond). The resultant scattered photon has an energy of $\hbar\omega_s$. The system depicted consists of a ground state S_{gnd} and an electronic state S_{ele} each having sublevels (such as vibrational or rotational modes), with all states and levels discrete. An incident photon $\hbar\omega_0$ interacts with the system, taking the total energy of the system to an intermediate level S_{int} or S_{ele} after which a new photon $\hbar\omega_s$ is created and released as the system relaxes back to a lower energy state, not necessarily S_{gnd}. For Rayleigh scattering,

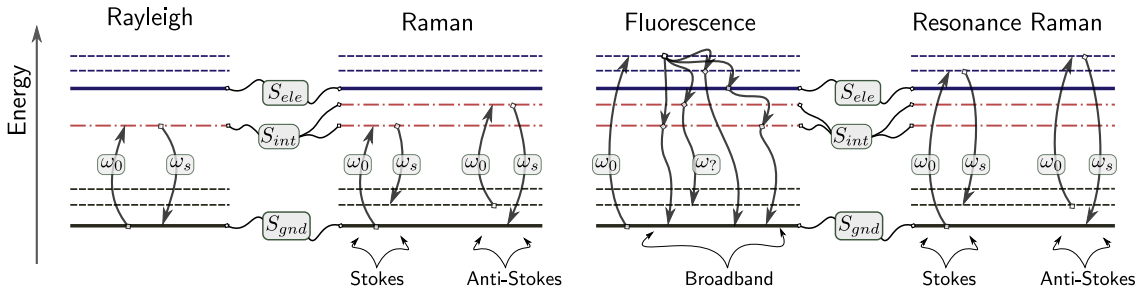

Figure 2.1: Jablonski energy transfer diagrams for Rayleigh, Raman, and fluorescence optical processes.

the incident photon $\hbar\omega_0$ interacts with the system, but does not gain or lose energy. The scattered photon energy is the same as the incident photon energy, so $\hbar\omega_0 = \hbar\omega_s$. For Raman scattering, the system interacts with the incident photon, $\hbar\omega_0$; however, due to the interaction with the system, the resultant photon either gains or loses energy, so $\hbar\omega_s = \hbar(\omega_0 \pm \Delta\omega)$. Also, the initial state of the system (the system may be thermally excited) will influence whether the scattered photon will gain or lose energy. When the system is initially excited to a level above the ground state, the scattered photon will gain energy and is termed the *anti-Stokes* shifted (higher energy) photon. When the system is initially at its lowest level (usually the ground state), the scattered photon will lose energy and is termed the *Stokes* shifted (lower energy) photon.[5] In the case of fluorescence, the energy transfered is large enough to excite the system into higher electronic state, such as S_{ele}. The result is the emission of photons of different energies as the system relaxes to different

[5]The Stokes namesake arises from the observations by George Stokes in the mid nineteenth century concerning fluorescence in fluorspar and uranium glass. He concluded that the absorption and emission spectra are shifted, due to loss in energy to the system.

intermediate states at different rates, giving broadband spectral content with exponentially decaying total lifetime of the fluorescence. When an incident photon has sufficient energy to excite the system into a higher electronic state S_{ele}, the photon may interact with the excited state. While interacting with the excited state, the scattered photon may gain or loss energy similar to the Raman scattering interaction. Interactions with specific features of the excited state results in resonance Raman scattering. As the excited states usually differ from the ground state (different potential energy surfaces), resonance Raman scattering can yield different and unique information about the system not observed with non-resonant Raman scattering.

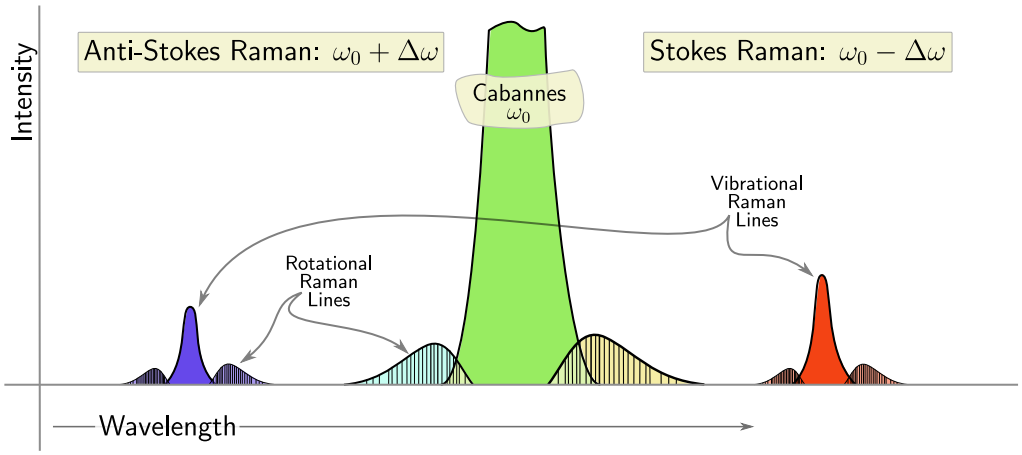

Figure 2.2: Relationship between the Rayleigh and Raman spectral peaks showing the rotational sidebands that straddle the more intense Rayleigh and vibrational Raman peaks.

The different quantum mechanical energy levels inside a system are ranked from highest to lowest as electronic, vibrational, and rotational, requiring more energy to excite higher ranked levels. These different quantum levels are associated with different excitation wavelength ranges. X-rays and ultraviolet wavelengths activate electronic transitions, visible and infrared wavelengths activate vibrational transitions, and microwave and radio wavelengths activate rotational transitions. Our resonance Raman experiments utilize the near-ultraviolet and ultraviolet regions of the spectrum. For Raman scattering, a typical experimental spectra may look as depicted in Figure 2.2, showing the relationships between the different features of the spectra. For gases and vapors the rotational Raman sidebands

of the more intense Cabannes line and vibrational Raman lines are more defined due to the availability of rotational states as the molecules are free to rotate without confinement. As the sample density increases, intermolecular interaction between the molecules restricts the available number of rotational states such that for liquids, no or few rotational states are available, leaving only the vibrational levels with little rotational sideband contribution to the spectra. For crystalline species, there are increased restrictions on allowable vibrations, resulting in some spectra features becoming more pronounced with the possibility of splitting of the vibrational Raman lines [Long, 1977]. Solid state spectra depend on crystal symmetries, excitation polarization, and temperature [Long, 1977; Smith and Dent, 2005].

The intensities of the vibrational and rotational spectra are skewed to the Stokes shifted side of the spectra due to the initial population of the system's vibrational and rotational energy levels. Given a particular temperature, these molecular energy levels will become populated as determined by the energy partition function of the system. This leads to the familiar Boltzmann distribution of states, Equation (2.4.2), where N_i is the number of molecules in energy state E_i with degeneracy g_i (number of substrates within energy level E_i) and temperature T, with k_B Boltzmann's constant.

$$f_B = \frac{N_i}{N} = \frac{g_i\, e^{-E_i/k_B T}}{Q} \quad \text{and} \quad Q = \sum_n e^{-E_n/k_B T} \tag{2.4.2}$$

The partition function Q represents the total number of states available to the system and is a product of rotational, vibrational, and electronic quantum states [Linne, 2002; Menzel, 1960a,b]. If we consider equivalent degeneracy, and two different energy states E_i and E_j such that $E_j > E_i$, then the Boltzmann distribution (2.4.2) says that the higher energy state E_j will be less populated. This translates directly to the anti-Stokes shifted spectra being less intense than the Stokes as $\omega_j = (2\pi\, c/\lambda_j) > \omega_i = (2\pi\, c/\lambda_i)$. As the temperature of the system increases, the number of occupied higher energy levels increases resulting in increased scattering intensity for the anti-Stokes Raman line [Linne, 2002].

2.5 Raman and Resonance Raman Scattering

The classical description of Rayleigh and Raman scattering start by examining the multipole expansion of the electromagnetic fields of induced dipole. Following the thorough

development given by Long, we can represent the electric field of the dipole moment as,

$$\mathbf{p} = \mathbf{p}_1 + \mathbf{p}_2 + \mathbf{p}_3 + \cdots = \widetilde{\boldsymbol{\alpha}} \cdot \mathbf{E} + \frac{1}{2}\widetilde{\boldsymbol{\beta}} \colon \mathbf{E}\,\mathbf{E} + \frac{1}{6}\widetilde{\boldsymbol{\gamma}} \colon \mathbf{E}\,\mathbf{E}\,\mathbf{E} + \cdots , \tag{2.5.1}$$

where $\widetilde{\boldsymbol{\alpha}}$, $\widetilde{\boldsymbol{\beta}}$, and $\widetilde{\boldsymbol{\gamma}}$ represent the *polarizability*, *hyper-polarizability*, and *second hyper-polarizability* tensors respectively [Long, 2002].[6] We restrict the multipole expansion to terms linear in the dipole moment thereby reducing the problem to determining the contributions to the fields from the polarizability $\widetilde{\boldsymbol{\alpha}}$. For Rayleigh and Raman scattering we then have,

$$\mathbf{p}_0(\omega) = \widetilde{\boldsymbol{\alpha}}_{Ray} \cdot \mathbf{E}_0(\omega) \text{ and } \mathbf{p}_0(\omega \pm \omega_n) = \widetilde{\boldsymbol{\alpha}}_{Ram} \cdot \mathbf{E}_0(\omega), \tag{2.5.2}$$

where $\mathbf{p}_0$ and $\mathbf{E}_0$ are the time independent amplitudes of the dipole moment and electric field respectively, $\widetilde{\boldsymbol{\alpha}}_{Ray}$ is the equilibrium polarizability, and $\widetilde{\boldsymbol{\alpha}}_{Ram}$ the polarizability associated ω_n. The departure from the classical treatment arises from the inadequate quantitative description of $\widetilde{\boldsymbol{\alpha}}_{Ray}$ and $\widetilde{\boldsymbol{\alpha}}_{Ram}$ in characterizing the molecular properties. While the classical treatment is quite sufficient for Rayleigh scattering, the classical treatment can only give qualitative information about Raman scattering of the system. The proper treatment of molecular vibrations and rotations is only possible using the quantum mechanical treatment [Long, 2002]. The approach is to treat the molecule quantum mechanically and the electromagnetic field classically by considering the field as a perturbation of the quantum mechanical energy. We assume the unperturbed system is solved, thereby allowing us to use the unperturbed wavefunctions and solve for the eigenvalues of the perturbation using standard perturbation theory.

We replace the classical dipole moment with the *transition dipole moment operator*, $\hat{\mathbf{p}}$, that describes the transition of the system from an initial state, i, to a final state, f, due to interaction with an electric field.[7] This framework follows from the quantum mechanical treatment of dispersion theory developed by Kramers and Heisenberg [Anderson, 1971], [Van Vleck, 1929]. Again we limit the terms to first-order in the dipole as in (2.5.2). The first-order induced transition dipole moment is given as,

$$\widetilde{\mathbf{p}}^{(\mathbf{1})} = \langle \psi_f | \hat{\mathbf{p}} | \psi_i \rangle \tag{2.5.3}$$

[6] For monochromatic dynamic fields, the Maxwell curl equations link the electric and magnetic fields and as such, the multipole expansion is usual presented for the electric field. In certain materials, the magnetic permeability may have significant departure from μ_0, however for optical frequencies in most materials $\mu \approx \mu_0$ and the variations in permittivity dominates [Griffiths, 1989].

[7] In general, all quantities are considered complex.

where $|\psi_i\rangle$ and $|\psi_f\rangle$ are the first-order time-dependent initial and final state wavefunctions respectively. The wavefunctions are found for the system using the time-dependent Schrödinger's equation,

$$\Big(\mathcal{H}_0 - \hat{\mathbf{p}}\cdot\mathbf{E} - \imath\hbar\frac{\partial}{\partial t}\Big)|\psi\rangle = 0 \tag{2.5.4}$$

where $\mathcal{H}_0$ is the unperturbed system Hamiltonian and $\mathcal{H}_p = \hat{\mathbf{p}}\cdot\mathbf{E}$ is the dipole interaction perturbation Hamiltonian. The wavefunctions $|\psi\rangle$ are expanded as,

$$|\psi\rangle = |\psi^0\rangle + |\psi^1\rangle + \cdots \tag{2.5.5}$$

with $|\psi^0\rangle$ and $|\psi^1\rangle$ representing the unperturbed and first-order perturbed time-dependent wavefunctions respectively. The problem becomes the determination of the contributing terms in the polarizability tensor, so we can replace the $\widetilde{\boldsymbol{\alpha}}$ with its expectation value (observable) giving now in the most general terms,

$$\big[\widetilde{\mathbf{p}}^{(\mathbf{1})}\big]_{fi} = \langle\psi_f|\widetilde{\boldsymbol{\alpha}}|\psi_i\rangle\cdot\mathbf{E}_0. \tag{2.5.6}$$

We can write the time-dependent wavefunctions as,

$$\psi_n = \phi_n\,\exp\{-\imath(\omega_n - \imath\Gamma_n)t\}, \tag{2.5.7}$$

with ϕ_n the time-independent wavefunction for state n and Γ_n related to the lifetime of the state (via the uncertainty principle) as $\tau_n = 1/2\Gamma_n(\omega_n)$. If we also suggest that the initial and final states have appreciably long lifetimes ($\Gamma_i = \Gamma_f \to 0$) then these wavefunctions simplify further. As such we can formulate the ρ component of the real induced transition dipole moment $\big[\widetilde{\mathbf{p}}^{(\mathbf{1})}\big]_{fi}$, given in Long as,

$$\begin{aligned}
&\big[\widetilde{p}_\rho^{(1)}\big]_{fi} = \\
&\frac{1}{2\hbar}\sum_{r\neq i}\left\{\frac{\langle\phi_f|\hat{p}_\rho|\phi_r\rangle\langle\phi_r|\hat{p}_\sigma|\phi_i\rangle}{\omega_{ri} - \omega_0 - \imath\Gamma_r}\widetilde{E}_{\sigma 0}\,e^{-\imath(\omega_0-\omega_{fi})t} + \frac{\langle\phi_f|\hat{p}_\rho|\phi_r\rangle\langle\phi_r|\hat{p}_\sigma|\phi_i\rangle}{\omega_{ri} + \omega_0 + \imath\Gamma_r}\widetilde{E}^*_{\sigma 0}\,e^{-\imath(\omega_0+\omega_{fi})t}\right\} \\
&+ \frac{1}{2\hbar}\sum_{r\neq f}\Big\{\cdots\Big\} + \text{complex conjugate.}
\end{aligned} \tag{2.5.8}$$

Under some assumptions as argued by Placzek, more simplifications to (2.5.8) can be made [Long, 2002]. If we consider terms involving $\widetilde{E}_{\sigma 0}\,e^{-\imath(\omega_0-\omega_{fi})t}$ to describe Rayleigh scattering ($\omega_{fi} = 0$), anti-Stokes Raman scattering ($\omega_{fi} < 0$), and Stokes Raman scattering ($\omega_{fi} > 0$),

with $\omega_{fi} = \omega_f - \omega_i$, we finally arrive at a general expression for the transition polarizability tensor. In component form,

$$[\alpha_{\rho\sigma}]_{fi} = \frac{1}{2\hbar} \sum_{r \neq i,f} \left\{ \frac{\langle \phi_f | \hat{p}_\rho | \phi_r \rangle \langle \phi_r | \hat{p}_\sigma | \phi_i \rangle}{\omega_{ri} - \omega_0 - \imath\Gamma_r} + \frac{\langle \phi_f | \hat{p}_\sigma | \phi_r \rangle \langle \phi_r | \hat{p}_\rho | \phi_i \rangle}{\omega_{ri} + \omega_0 + \imath\Gamma_r} \right\}. \tag{2.5.9}$$

The scattering intensity (measured quantity) is then determined as with (2.4.1). Additionally (2.5.9) will determine the Raman selection rules for the system which is to say that the requirement is that $[\alpha_{\rho\sigma}]_{fi}$ have some non-zero elements. This general form of the transition dipole tensor (2.5.9) will be difficult determine, and will therefore require the introduction of more simplifications to allow us to determine the contributing terms responsible for the scattering intensity.

We can however make some qualitative observations as to the behavior of (2.5.9). The nature of the denominators in (2.5.9) is of obvious consequence to resonance Raman scattering. Consider the relationship between the absorption frequency ω_{ri} and the excitation frequency ω_0 for some special cases. If $\omega_0 \ll \omega_{ri}$, so the excitation frequency is much smaller than the absorption frequency, then the denominator is dominated by the absorption frequency since the broadening is small compared to the absorption frequency. In the case where $\omega_0 \approx \omega_{ri}$, the denominator becomes very small, exploding the magnitude of the polarizability provided there are non-zero numerators. Preresonance behavior is observed as the excitation frequency approaches the absorption. Concerning the numerators, the requirement that (2.5.9) have non-zero terms (selection rules) will determine the level and state transitions that will contribute to the scattering. The products of the expectation values of the transition dipole moments such as $\langle \phi_f | \hat{p}_\rho | \phi_r \rangle \langle \phi_r | \hat{p}_\sigma | \phi_i \rangle$ describe the linkage between the dipole transitions, for example a first transition being associated with an absorption $|\phi_i\rangle \rightarrow |\phi_r\rangle$ and the second associated with an emission $|\phi_r\rangle \rightarrow |\phi_f\rangle$. Summation over the intermediate states $\sum_{r \neq i,f}$ will give the weighted contributions of these linked transitions. In the case where $\omega_0 \ll \omega_{ri}$, there can exist many linked transitions that satisfy this condition, thereby resulting in many intermediate states contributing to the scattering. This condition is observed in non-resonant Raman, making it difficult to identify information about particular intermediate states. When $\omega_0 \approx \omega_{ri}$ the contribution is limited to a few participating intermediate states. This property is what allows resonance enhanced Raman scattering to be used to obtain information about these intermediate states. Fi-

nally, there are symmetry considerations for $[\alpha_{\rho\sigma}]_{fi}$. Degeneracy arguments for the initial and final states can be discussed for both Rayleigh and Raman scattering; however in most circumstances, Rayleigh scattering is degenerate in the initial and final states therefore the resulting tensor is symmetric, and since the states are different in the case of Raman scattering, the tensor is considered to be asymmetric. These arguments are given by Long and the reader is directed to [Long, 2002] for more discussion.

2.6 Forms of the Polarizabiltiy Tensor

As previously mentioned, the non-zero terms of $[\alpha_{\rho\sigma}]_{fi}$ may be difficult to determine due to the complex nature of the linked states involved, the form of the system's wavefunctions, and the geometry of the scattering system. In the case of non-resonant Raman scattering, the non-zero terms of the polarizability are potentially due to a large number of terms relating to the transition from the initial state, i, through several possible intermediate states, r, and relaxation from these intermediate states to the final state, f. These terms can all have appreciable contribution to the overall intensity, thereby making separation of the contributing intermediate states difficult if not impossible in non-resonant Raman scattering. However in the case of resonance Raman scattering, since the intermediate states are usually at the bottom of the potential well of the higher electronic state (typically the first electronic state above the ground state), the determining which states are contributing to the overall scattering is simplified. To aid in determining what terms in the polarizability are contributing to the scattering the following assumptions proposed by G. Placzek may be adopted.[8] The main assumptions are that: *1*) the excitation frequency ω_0 is much less than the absorption frequency ω_{ri}, *2*) the system's initial and final electronic states are the non-degenerate ground electronic state, and *3*) the nuclear and electronic displacements are small, allowing for the separation of the system wavefunctions, the *Born-Oppenheimer* approximation [Anderson, 1971; Clark and Dines, 1986; Albrecht, 1961]. These assumptions result in a relatively good description of non-resonant Raman scattering however when considering resonant Raman, these are invalidated due to the proximity of the absorption and excitation frequencies. In work done by P. P. Shorygin, J. Behringer

[8] Placzek's paper is a well cited work, however difficult to obtain in English. Most discussions on the Raman effect significantly cover his approach, therefore credit is extended although not specifically referenced.

and J. Z. Brandmüller, Rea [Rea, 1960], Albrecht [Albrecht, 1961], Clark and Dines [Clark and Dines, 1986] and Lee [Lee, 1983] these assumptions are addressed in various ways and provide an adequate framework for determining the contributing terms in resonance Raman scattering.[9]

2.6.1 General Form of the Polarizability Tensor

Essential to the Placzek approach is the use of the Born-Oppenheimer approximation to separate the wavefunctions of the system into products of the wavefunctions for each of the quantum mechanical energy regimes. This approach to the system's wavefunctions is also shared in those cases that are not held to the strict conditions assumed by Placzek. The interaction of the light with the system is assumed to be slow enough such that the movements of the nuclei with respect to each other are small and the electron displacements are effectively described with a Hamiltonian representing fixed nuclei [Sakurai, 1994]. This allows the separation of the overall system wavefunction into a product of wavefunctions. For a general system wavefunction $|j\rangle$,

$$\begin{aligned} |j\rangle &= |e^j v^j R^j\rangle \rightarrow |e^j\rangle|v^j\rangle|R^j\rangle, \quad \text{also} \\ \omega_j &= \omega_{e^j v^j R^j} \rightarrow \omega_{e^j} + \omega_{v^j} + \omega_{R^j} \end{aligned} \tag{2.6.1}$$

where $|e^j\rangle$, $|v^j\rangle$, and $|R^j\rangle$ are the electronic, vibrational and rotational wavefunctions respectively for overall state j with equivalent separation for the quantum mechanical frequencies ω_j. This separation allows us to pull out the terms that contribute little to the summation over states by evoking the closure theorem for the wavefunctions. For situations where the excitation frequency is much smaller than any electronic absorption frequency, yet much larger than any vibrational or rotational frequency, we can evoke the closure theorem on the rotational wavefunctions as the contributions of the rotational wavenumbers on the broadening terms in the denominator are small. In terms of experimental observation, this condition suggest that the spectra is dominated by the contributions of the vibrational energies with little or no observed rotational structure in the spectra. resolution statement–washout The

[9] The work of Shorygin and Behringer and Brandmüller follow the same availability as in 8.

polarizability then follows as,

$$[\alpha_{\rho\sigma}]_{fi} = \frac{1}{\hbar} \sum_{\substack{e^r v^r \neq e^g v^i, \\ e^f v^f}} \left\{ \frac{\langle v^f | \langle e^f | \hat{p}_\rho | e^r \rangle | v^r \rangle \langle v^r | \langle e^r | \hat{p}_\sigma | e^g \rangle | v^i \rangle}{\omega_{e^r e^g} + \omega_{v^r v^i} - \omega_0 - \imath \Gamma_{e^r v^r}} \right. \\ \left. + \frac{\langle v^f | \langle e^f | \hat{p}_\sigma | e^r \rangle | v^r \rangle \langle v^r | \langle e^r | \hat{p}_\rho | e^g \rangle | v^i \rangle}{\omega_{e^r e^f} + \omega_{v^r v^f} + \omega_0 + \imath \Gamma_{e^r v^r}} \right\}. \tag{2.6.2}$$

This version of the polarizability tensor holds well for the description of the Raman and resonance Raman scattering, provided there is not a significant displacement of the nuclei of the system violating the Born-Oppenheimer approximation. Under the more stringent assumptions by Placzek the tensor may be separated into two parts, one part for the summation over states where the intermediate electronic state is the electronic ground state and the other part for the summation over states where the intermediate and ground electronic states are different. Also, if the broadening terms are considered small, we obtain,

$$\begin{aligned} &[\alpha_{\rho\sigma}]_{fi} = [\alpha_{\rho\sigma}]_{fi}^{e^r = e^g} + [\alpha_{\rho\sigma}]_{fi}^{e^r \neq e^g} \quad \text{and} \\ &\Gamma_{e^r v^r} = \Gamma_{e^g v^r} = 0. \end{aligned} \tag{2.6.3}$$

For the same electronic state ($|e^r\rangle = |e^g\rangle$), the separation has the vibrational transition frequencies, $\omega_{v^r v^i}$ and $\omega_{v^r v^f}$, in the denominators and since the excitation frequency is much larger than the vibration, this portion becomes small compared to the $|e^r\rangle \neq |e^g\rangle$ portion. The remaining portion then can be simplified by evoking the closure theorem over the vibrational states ($\sum_{v^r} |v^r\rangle\langle v^r| = 1$) within each of the electronic states, giving the pure vibrational transition polarizability,

$$[\alpha_{\rho\sigma}]_{v^f v^i} = \frac{1}{\hbar} \sum_{e^r \neq e^g} \left\{ \frac{\langle v^f | \langle e^g | \hat{p}_\rho | e^r \rangle \langle e^r | \hat{p}_\sigma | e^g \rangle | v^i \rangle}{\omega_{e^r e^g} - \omega_0} + \frac{\langle v^f | \langle e^g | \hat{p}_\sigma | e^r \rangle \langle e^r | \hat{p}_\rho | e^g \rangle | v^i \rangle}{\omega_{e^r e^g} + \omega_0} \right\}. \tag{2.6.4}$$

This expression of the polarizability tensor effectively describes those systems that do not exhibit significant absorption in the visible, but will exhibit Raman scattering in the visible. The failing of this expression in the describing resonance Raman scattering is due to the closure over the vibrational wavefunctions for the intermediate state. In the case of resonance Raman scattering, the denominators in (2.6.2) are sensitive to the vibrational energy contributions through the damping term, the separation between the vibrational frequencies, and the excitation frequencies.

2.6.2 Improving the Polarizability Tensor

To better describe Raman scattering, various developments found in Albrecht [Albrecht, 1961], Rea [Rea, 1960], Clark and Dines [Clark and Dines, 1986], and Galluzzi [Galluzzi, 1985] address different approaches for incorporating the separation between the vibrational and excitation frequencies, and influence of the broadening terms that the Placzek approach lacked. One of the problems in incorporating these properties us due to the Born-Oppenheimer approximation. While the approximation considers the electronic and nuclear displacements as separable, these movements are in fact coupled. This coupling is realized when the electronic transition moments $\hat{p}_{\rho,\sigma}$ have a small dependence on the nuclear displacements, Q_k. This is known as the *Herzberg-Teller vibronic coupling*. If the nuclear displacements are considered small about their equilibrium positions, such as in one-quantum vibrational transitions, then the electronic Hamiltonian can be expanded in a Taylor's series in the nuclear displacement Q_k. Using as the new Hamiltonian the first-order terms in the Taylor's series, the electronic transition dipole moments effectively undergo a small perturbation. Using perturbation theory and considering the additional intermediate states $|s\rangle$ and $|t\rangle$ in addition to $|r\rangle$ we obtain for the ρ component of the dipole transition,

$$[p_\rho]_{e^{f'}e^{r'}} = [p_\rho]^0_{e^f e^r} + \frac{1}{\hbar}\sum_{e^s \neq e^r}\sum_k [p_\rho]^0_{e^f e^s}\frac{h^k_{e^s e^r}}{\omega_{e^r} - \omega_{e^s}}Q_k + \frac{1}{\hbar}\sum_{e^t \neq e^f}\sum_k \frac{h^k_{e^f e^t}}{\omega_{e^f} - \omega_{e^t}}Q_k\,[p_\rho]^0_{e^t e^r}, \tag{2.6.5}$$

where the $[p_\rho]^0$ denotes the unperturbed electronic states' moments (e. .g. $\langle e^f|\hat{p}_\rho|e^r\rangle$) and the vibronic coupling terms are now introduced as,

$$h^k_{e^s e^r} = \langle\psi_{e^s}(Q_0)|\Big(\frac{\partial \hat{H}_e}{\partial Q_k}\Big|_0\Big)|\psi_{e^r}(Q_0)\rangle, \tag{2.6.6}$$

where the $|\psi_e(Q_0)\rangle$ states describe the electronic wavefunctions of the undisturbed equilibrium nuclear positions Q_0. Similar results follow for the σ component of the dipole transition. Following the development given in Section 2.5 with these new dipole transition moments expanded for the vibronic coupling contributions, we arrive at a useful description of the Raman and resonance Raman scattering polarizability tensor incorporating the frequency proximity and broadening term sensitivity absent in the Placzek development. The polarizability is separated in to different terms, each describing a particular set of contributing mechanisms to the scattering tensor. This form is the Abcd notation presented in the next section.

2.7 Polarizability for Resonance Raman

The ABCD notation for the polarizability is $[\alpha_{\rho\sigma}]_{e^g v^f : e^g v^i} = A + B + C + D$, with the terms defined in (2.7.1) as,

$$A = \frac{1}{\hbar}[p_\rho]^0_{e^g e^r}[p_\sigma]^0_{e^r e^g}\sum_{v^r_k}\frac{\langle v^{f(g)}_k|v^{r(r)}_k\rangle\langle v^{r(r)}_k|v^{i(g)}_k\rangle}{\omega_{e^r v^r_k : e^g v^i_k} - \omega_0 - \imath\Gamma_{e^r v^r_k}}$$

$$B = \frac{1}{\hbar^2}[p_\rho]^0_{e^g e^s}\frac{h^k_{e^s e^r}}{\omega_{e^r} - \omega_{e^s}}[p_\sigma]^0_{e^r e^g}\sum_{v^r_k}\frac{\langle v^{f(g)}_k|v^{r(r)}_k\rangle\langle v^{r(r)}_k|v^{i(g)}_k\rangle}{\omega_{e^r v^r_k : e^g v^i_k} - \omega_0 - \imath\Gamma_{e^r v^r_k}} +$$
$$\frac{1}{\hbar^2}[p_\rho]^0_{e^g e^r}\frac{h^k_{e^r e^s}}{\omega_{e^r} - \omega_{e^s}}[p_\sigma]^0_{e^s e^g}\sum_{v^r_k}\frac{\langle v^{f(g)}_k|v^{r(r)}_k\rangle\langle v^{r(r)}_k|Q_k|v^{i(g)}_k\rangle}{\omega_{e^r v^r_k : e^g v^i_k} - \omega_0 - \imath\Gamma_{e^r v^r_k}}$$

$$C = \frac{1}{\hbar^2}\frac{h^k_{e^g e^t}}{\omega_{e^g} - \omega_{e^t}}[p_\rho]^0_{e^t e^r}[p_\sigma]^0_{e^r e^g}\sum_{v^r_k}\frac{\langle v^{f(g)}_k|Q_k|v^{r(r)}_k\rangle\langle v^{r(r)}_k|v^{i(g)}_k\rangle}{\omega_{e^r v^r_k : e^g v^i_k} - \omega_0 - \imath\Gamma_{e^r v^r_k}} +$$
$$\frac{1}{\hbar^2}[p_\rho]^0_{e^g e^r}[p_\sigma]^0_{e^r e^t}\frac{h^k_{e^t e^g}}{\omega_{e^g} - \omega_{e^t}}\sum_{v^r_k}\frac{\langle v^{f(g)}_k|Q_k|v^{r(r)}_k\rangle\langle v^{r(r)}_k|v^{i(g)}_k\rangle}{\omega_{e^r v^r_k : e^g v^i_k} - \omega_0 - \imath\Gamma_{e^r v^r_k}}$$

$$D = \frac{1}{\hbar^3}[p_\rho]^0_{e^g e^s}\frac{h^k_{e^s e^r}h^k_{e^r e^{s'}}}{(\omega_{e^r} - \omega_{e^s})(\omega_{e^r} - \omega_{e^{s'}})}[p_\sigma]^0_{e^{s'} e^g}\sum_{v^r_k, v^r_{k'}}\frac{\langle v^{f(g)}_k|Q_k|v^{r(r)}_k\rangle\langle v^{r(r)}_{k'}|Q_{k'}|v^{i(g)}_{k'}\rangle}{\omega_{e^r v^r_k : e^g v^i_k} - \omega_0 - \imath\Gamma_{e^r v^r_k}}. \tag{2.7.1}$$

Each term of $[\alpha_{\rho\sigma}]_{e^g v^f : e^g v^i}$ describes a specific transition regime that contributes to polarizability. The expressions of (2.7.1) describe these transition regimes for vibrational resonance Raman where the system is initially in the ground electronic state, and returns to a final state within the ground electronic state is expressed in the notation, $[e^g v^f : e^g v^i]$. The vibrational transitions are our primary interest in this work. We allow for the intermediate states to be within (resonance) or near (preresonance) the first excited electronic state with the system returning to a vibrational level within the ground electronic state. These transitions are expected for the frequency range of our available excitation light source based on the available absorption spectra for the systems under investigation.

2.7.1 A-Term Contribution

There are two requirements to allow A-term contribution to the scattering intensity. First, the electric dipole transitions $[p_\rho]^0_{e^g e^r}$ and $[p_\sigma]^0_{e^r e^g}$ must be non-zero, meaning that the transitions must be electric-dipole allowed. This condition is satisfied for transitions within an intense absorption band. The magnitudes of these transitions moments

can be large; whereas weak intensity bands, while dipole-allowed, may not have significant contribution to the scattering intensity. Second, the vibrational overlap integrals or Franck-Condon factors, $\langle v_k^{f(g)}|v_k^{r(r)}\rangle$ and $\langle v_k^{r(r)}|v_k^{i(g)}\rangle$, must also be non-zero, establishing the selection rules for the allowed transitions. This requirement for non-zero Franck-Condon factors is satisfied in several ways. For orthogonal vibrational wavefunctions, recall that $\langle v_l|v_m\rangle = \delta_{lm}$ which would require that $v_k^{f(g)} = v_k^{r(r)} = v_k^{i(g)}$. Under this condition, no transition takes place; therefore there is no contribution to the scattering intensity. Contribution from the A-term arises from non-orthogonal wavefunctions and these are the most significant source of overtones observed in the experimental spectra. Non-orthogonality is related to differences between the potential energy surfaces of the initial, intermediate, and final states. One case occurs when the initial and final states are different, such that $\omega_{e^r v_k^r} \neq \omega_{e^g v_k^i}$. A second case is found when the potential energy surface minimum of the excited state is offset from the equilibrium position of the initial state potential energy surface. In terms of normal coordinates of the system, Q_k, then $\Delta Q_k \neq 0$ which is essentially a result of changes in molecular geometry. If these changes in geometry are associated with distortions in the molecule that are symmetric, such as changes in bond angles and bond lengths, then the offset is deemed totally symmetric and only effects those vibrational modes that are about those normal coordinates. An example of such a change is the ring breathing vibrational mode of the benzene molecule, where the bond lengths between the carbon atoms all lengthen and shrink along the bond. While the overall symmetry of the molecule is preserved, the molecule has obviously distorted. Should the symmetries in the excited state and ground states differ, then not only does the ground state symmetry matter but those shared symmetry aspects of the excited state as well. This condition serves to remove degeneracies and configure the molecule into more stable geometries even if symmetry is removed. Figure 2.3 illustrates how the potential energy surface differences influence the amplitude of the Franck-Condon factors. In Figure 2.3 the symmetries of the states are the same, however with only small offsets in the potential energy surface minimums, the Franck-Condon factors can become quite large [Ellis et al., 2005].

When the potential energy minima are not offset, so $\Delta Q_k = 0$, then both totally symmetric modes and non-totally symmetric modes can give non-zero vibrational overlap integrals provided the vibrational energies $\omega_{e^r} \neq \omega_{e^g}$. Hence there will be no A-term scattering for same energy vibrational levels in symmetrically similar electronic states. If the

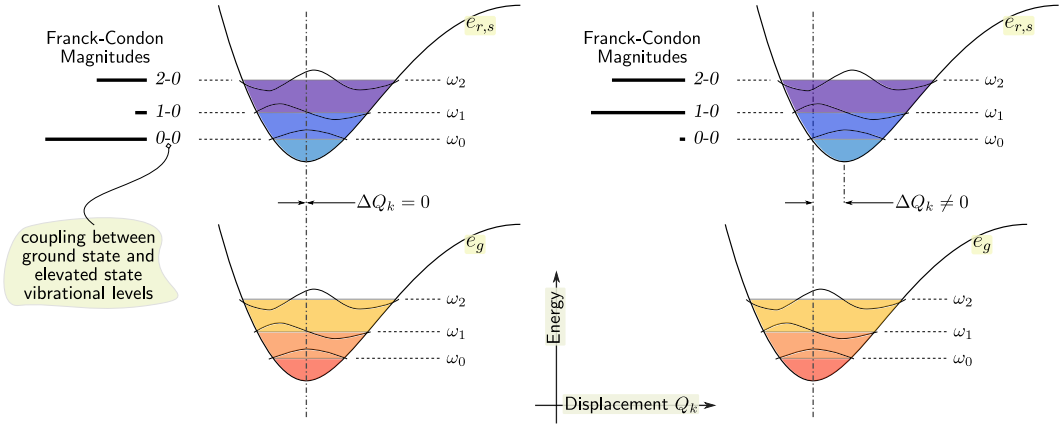

Figure 2.3: Illustration of the Franck-Condon effect in a two state scattering system.

vibrational energies are different, then both symmetrically similar and non-totally symmetric electronic states will contribute to the scattering intensity. In the case where $\Delta Q_k \neq 0$, it is only the total symmetric modes that contribute to the scattering intensity.

2.7.2 B-Term Contribution

Non-zero B-term contributions require several conditions to be satisfied. As with the A-term, the electric-dipole transition must be allowed, particularly both transition dipole moments from the ground (initial) to the intermediate (s), $[p_\sigma]^0_{e^s e^g}$ and $[p_\sigma]^0_{e^r e^g}$, and the intermediate (s) to the ground (final), $[p_\rho]^0_{e^g e^s}$ and $[p_\rho]^0_{e^g e^r}$. Additionally, one of the vibronic coupling terms, $h^k_{e^s e^r}$ and $h^k_{e^r e^s}$, must also be non-zero. These terms describe the mixing or linkage between the intermediate states $|e^r\rangle$ and $|e^s\rangle$ through the normal coordinate Q_k as described by (2.6.6). Symmetry arguments dictate that the vibronic coupling terms will only be non-zero for either totally symmetric or non-totally symmetric fundamental modes. For totally symmetric modes, the intermediate electronic states, r and s, must have the same symmetry, and since same symmetry electronic states are usually not close together, the vibronic term is small as there is a large energy difference between the intermediate states, so $\Delta\omega_{e^r e^s} = \omega_{e^r} - \omega_{e^s}$ is large.

Finally we need to consider the vibrational transition integrals, $\langle v^{f(g)}_k | Q_k | v^{r(r)}_k \rangle$ and $\langle v^{r(r)}_k | Q_k | v^{i(g)}_k \rangle$, and the overlap integrals, $\langle v^{r(r)}_k | v^{i(g)}_k \rangle$ and $\langle v^{f(g)}_k | v^{r(r)}_k \rangle$. The selection rules for the products of these integrals limits the B-term contribution to only fundamental vibra-

tional modes. Considering the harmonic oscillator approximation as an example and using the harmonic oscillator ladder operators, the vibrational transition integrals and overlap integral products will be of the form $\langle v_k^{f(g)}|Q_k|v_k^{r(r)}\rangle\langle v_k^{r(r)}|v_k^{i(g)}\rangle = \langle 1_k^{f(g)}|Q_k|0_k^{r(r)}\rangle\langle 0_k^{r(r)}|0_k^{i(g)}\rangle$ and provide non-zero contribution. Unlike the A-term contributions, the B-term is not responsible for any overtone enhancements due to this fundamental mode restriction. When the excitation frequency is sufficiently different from the absorption frequency, the main contributions to the scattering intensity originate in the B-term.

2.7.3 C- and D-Term Contributions

In many systems the contributions from C and D terms are mostly negligible. The vibronic coupling mechanism in the C-term arises from interactions of the ground state with a higher set of intermediate states (t), unlike in the B-term, where the vibronic coupling is between the intermediate states only. The energy difference between the ground state and the intermediate states can be fairly large, making the contribution of these vibronic couplings quite small. Otherwise the same conditions of allowed electric dipole transitions and non-zero vibrational transitions and overlap integrals presented for the B-term apply to the C-term. The D-term describes the interactions of excited states with other excited states. Overtone and binary combination vibrational modes are associated with the D-term and are expected to be considerably weak.

2.8 Considerations Relative to this Study

To close the discussion on the theoretical development of resonance Raman, I will address some limitations on the application of these theoretical results to our experimental work. In an ideal situation, the experimental data would enable us to extract various information about the states and transitions contributing to the scattering intensity. One of the benefits of resonance enhancement of the Raman scattering intensity is the participation of only a limited set of transitions to the first excited electronic state. This can lead to simplifications in the computation of the scattering tensor elements, unlike non-resonant Raman scattering, where a large number of intermediate states may be participating in the intensity. However, determining the participating transitions in the resonance Raman regime requires an understanding, a priori, of the potential energy surface of the first excited state and how

the vibrational levels are distributed. This task becomes significantly complicated as the system under investigation increases in complexity. One technique used to distinguish what may or may not be contributing to the scattering intensity is to select out participating transitions based on their polarization using an polarization analyzer. Typically spectra acquisition involves measuring the polarization state of the spectra and establishing a set of depolarization ratios for the spectral features. Using a polarization analyzer, we can essentially limit the number of matrix elements in $[\alpha_{\rho\sigma}]_{e^g v^f : e^g v^i}$ that need to be determined because only certain states will be responsible for the scattering intensity of a particular polarization [Esposito et al., 1997]. Figure 2.4 illustrates the scattering arrangement in this work, excluding the analyzer.

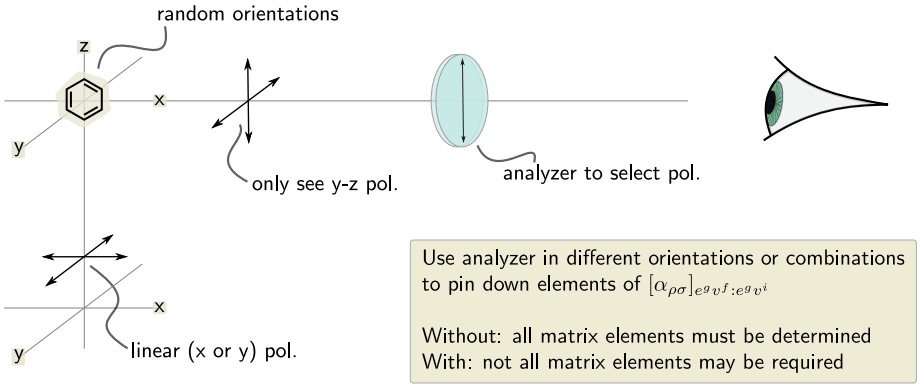

Figure 2.4: 90 degree Raman scattering configuration showing how the observed signal originates from a spatial average of a random ensemble of scattering agents.

With the exception of diamond, our sample systems are liquid and due to the random orientation of the individual molecules in bulk volume the scattering intensity is attributable to spatial average of the excited molecules. The spatial average of the intensity is related to the invariants of the polarizability tensor under rotations and transitions, which are tabulated [Long, 2002]. By changing the scattering angle and utilizing a polarization analyzer, determination of the contributing terms of the polarizability tensor can be simplified due to the properties of the invariants. In our work presented here, no polarization analyzer was utilized and the scattering angle was fixed at 90 degrees for all experimental trials. This limits the amount of information we can extract from the experimental spectra. Additionally, the spectra obtained from the diamond suffers from similar limitations on the

amount of information we can extract. In our experiments, the orientation of the diamond sample was not fixed and the surface features of the diamond are not well classified as the diamond is a rough stone instead of a precision cut crystal or deposited film. The scattering intensity of solid and crystalline sample species is strongly dependent on the geometric structure and orientation of the crystal and changing its orientation may complicate spectral interpretation [Smith and Dent, 2005].

Finally, for a portion of our investigations we utilized binary liquid sample species. This introduces the spectral features of the solvent, solvent fluorescence, and may introduce some solvent related shifting of the vibrational energies of both the solute and solvent. In the resonance Raman regime, the spectral features are easily distinguished due to the selective enhancement while on resonance. Typically the solute and solvent do not share similar absorption profiles [Jones et al., 1985; Browne and McGarvey, 2007]. The fluorescence of the solvent is not an issue for our ultraviolet excitation; as observed by Asher et al. [Asher and Johnson, 1984; Asher, 1993a] the fluorescence is not significant for excitation wavelengths below approximately $270\,nm$. Finally, the solvent induced effects on the Raman spectra may mask certain spectra features of the solute. The solvent may introduce some low-frequency vibrational motions to the solute that appear in the spectra, and there may be uncertain local environmental fluctuations that couple into the vibrational energies as well [Siebrand and Zgierski, 1982]. These effects will tend to shift the spectral peaks and may broaden the solute's spectral lineshapes. While the accounting for the spectral shifts is fairly straight-forward, the broadening may not be clear and this can complicate estimations on the lifetimes of the participating intermediate states. Recall that the lifetimes are related to the broadening terms in the denominators of the polarizability tensor elements. While near resonance, the broadening term is very influential due to the small energy difference between the absorption and excitation frequencies; also this can only reveal significant information about the intermediate state if the solvent influence is well understood.

Chapter 3

Instrumentation

3.1 Overview

This chapter will describe the significant components and arrangement of the experimental apparatus utilized in conducting the research. The apparatus is divided into three portions: sample positioning, wavelength tunable excitation light source, and the spectrometer system. Particular attention is given to discussion of the tunable excitation source. Also, a model to estimate the spectral efficiency of the spectrometer system is presented.

3.2 General Apparatus

3.2.1 Sample Positioning

Sample positioning in our apparatus is fairly straightforward. Positioning is handled in two fashions: one by direct movement of the sample with respect to the spectrometer's coupling optics, and the other by sweeping the incident light across a stationary sample. We employ a 90 degree scattering geometry and control the sample's three spatial coordinates utilizing two simple linear stages and a two-axis rotational mount. The positioning arrangement is primarily sensitive in the horizontal and vertical axes (Y and Z respectively in Figure 3.1). The Y-axis corresponds to the excitation laser beam's horizontal position relative to the vertical spectrometer slit. The Z-axis corresponds to the distance from the sample to the collection optics' focal plane. Experimental trials have the sample placed

in the focal plane of the collection optics with the excitation laser beam centered on the sample. The optimal sample position is the position where the interaction volume of the sample is within the focus of the spectrometer coupling optics. Figure 3.1 illustrates the standard experimental configuration.

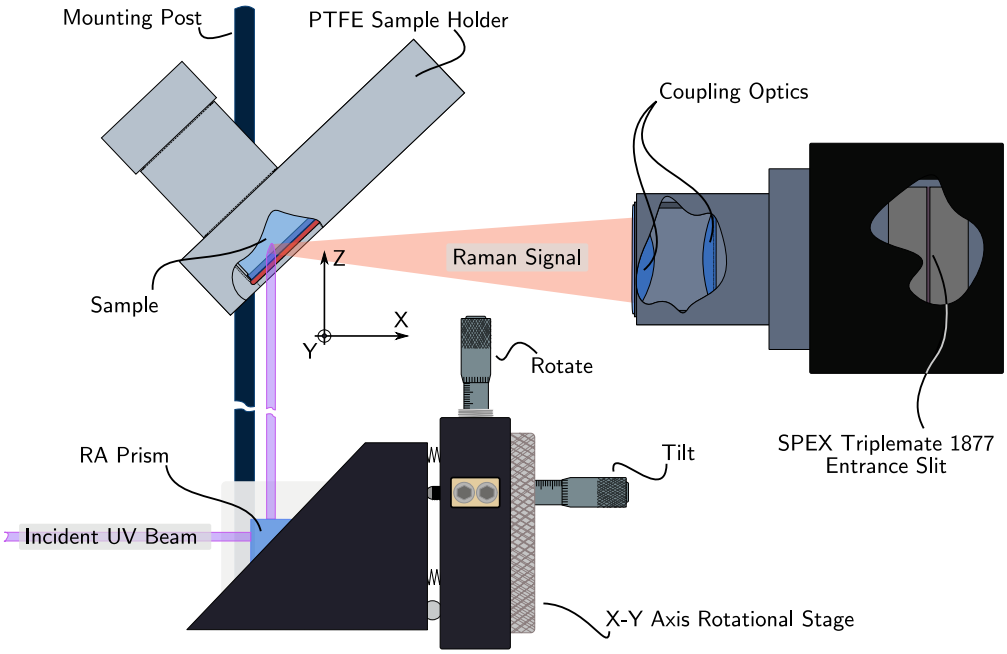

Figure 3.1: Illustration of the typical experimental configuration.

3.2.2 Spectrometer Coupling

Initial trials were performed using a smaller spectrometer (Instruments SA HR-320). The HR-320 spectrometer has a small dispersion yielding approximately 20 nm across the exit slit and has a focal length of 0.1 m, using a 1200 gr/mm grating. The main experimental trials were performed using a larger spectrometer (Spex Triplemate 1877) and its specifications are outlined in Section 3.5. The coupling optics we utilized readily available off-the-shelf ultraviolet grade fused silica lenses and sapphire windows. The lens arrangement is a *split-lens* configuration, using two lenses to image the focal spot from the sample onto the spectrometer entrance slit. The lens selection allowed some flexibility in positioning of the focal spot with respect to the spectrometer while attempting to match the available

numerical aperture of the spectrometer. Equations (3.2.1) are used to calculate the lens parameters and the best matches available are selected from vendors such as Thor Labs and Edmund Optics.

$$f/\# = \frac{f}{D} = \frac{1}{2NA} \text{ and } \quad NA = n\sin\theta, \tag{3.2.1}$$

where $n = 1$, for the index of refraction of air. Figure 3.2 shows the arrangement of the optics used to calculate the parameter values and Table 3.1 lists these parameters for both the SPEX and Instrument SA spectrometer systems. There is a shortcoming of this method

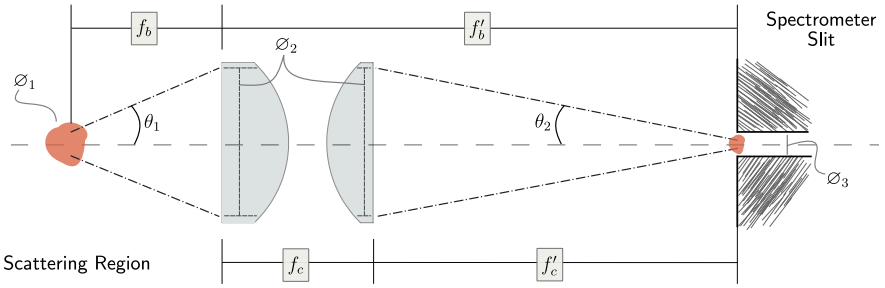

Figure 3.2: Schematic used for calculating the coupling optics' parameters.

Table 3.1: Summary of calculated coupling optics parameters.

Spectrometer	Slit Width $\varnothing_3$, (mm)	$f/\#$	NA	Front Lens f_b	Back Lens f_c'	(θ_1, θ_2)
HR-320	0.05	6.4	0.078	$38\,mm$	$175\,mm$	$8.75°, 3.06°$
SPEX	1.5	3.9	0.128	$38\,mm$	$75\,mm$	$8.75°, 6.55°$
SPEX étendue	4.6e-9	$r_1 = 0.5\,mm$	$r_2 = 125\,\mu m$	$d = 2640\,mm$		

Clear apertures, $\varnothing_2$, are taken as $0.75\varnothing_{lens} = 18.75\,mm$. For the étendue calculation $\omega_f = 2r_1$ and $2r_2$ is the main slit width of the SPEX spectrometer.

of coupling into the spectrometer. The coupling of the light from the scattering region into the spectrometer slit is not very efficient. This can be quantified by the total étendue of the system.[1] Étendue can be calculated using different methods; to calculate the total étendue, Λ, for our system, consider the following method utilizing the shape factor, $F_{A_1-A_2}$, going

[1]The étendue of an optical system is either conserved or increasing [Chaves, 2008]. The interpretation then is that some optical element in the system (such as a slit) will limit the maximum throughput of the system.

from surface A_1 to A_2:

$$F_{A_1-A_2} = \frac{1}{2}\big(Z - \sqrt{Z^2 - 4X^2Y^2}\big), \quad \text{and} \tag{3.2.2}$$

$$\Lambda = \pi A_1 F_{A_1-A_2}, \tag{3.2.3}$$

where $X = r_2/d$, $Y = d/r_1$, $Z = 1+(1+X^2)Y^2$, and $r_{1,2}$ are the radii of the circular surfaces $A_{1,2}$ separated by distance d [Chaves, 2008]. The circular surface areas, $A_{1,2}$, are determined from the coupling lens focal waist and the spectrometer slit width. The focal waist of the coupling lens can be approximated by: $\omega_f = 2.44\lambda f/D$, where D is the clear aperture of the lens, and for $\lambda = 250\,nm$ the expected waist size is $\sim 1\,\mu m$ [Moore et al., 1989]. The total étendue for our system is listed in Table 3.1. Clearly, focusing the incident light to a focal spot would be more efficient, taking advantage of filling the numerical aperture of the first coupling lens; however, having a continuously variable wavelength light source complicates any light focusing arrangements due to chromatic abberation. Normally, utilizing an achromat lens is sufficient to correct for chromatic abberation, however, the availability of achromat lenses that cover the ultraviolet to deep ultraviolet portion of the spectrum are sparse (and expensive). Typical optically transparent adhesives (such as the Norland optical adhesives) tend to exhibit transparency in the visible, while showing strong absorption in the ultraviolet.[2] Though small changes in the tuning wavelength is manageable, changes larger than several tens of nanometers causes the coupling to become disjointed.

A more significant issue is associated with the focusing of high-power laser pulses. The energy density of the focused laser pulse is sufficient to cause the breakdown of the sample material at reasonable laser operating power. A consequence is the generation of residues from the breakdown of the sample on the container window. The residue interferes with both the Raman spectra and may attenuate the incident and signal light. Several arrangements were attempted to improve the coupling. One scheme involved using lenses of appreciably long focal lengths optimized for different wavelengths. The lenses were placed downstream of the sample to focus the light some before the sample was illuminated. The second scheme utilized a spherical mirror to reflect the light into the sample with the sample placed inside the mirror's focal length. Both of these attempts yielded little in terms of signal enhancements, due primarily to the attenuation of the incident laser power by the

[2]Norland adhesives are UV cured and show strong fluorescence after curing.

anti-reflective coatings and substrate materials of the lenses and the protective coating of the spherical mirror.

3.2.3 Other Sample Control

The original experimental proposal for this work was to investigate tunable excitation resonance Raman enhancements in vapor phase species. Sample control for the vapor species is identical to that of the liquid sample species excluding the sample container. This sample vessel comprised a rectangular block of stainless steel fitted with sapphire windows on two parallel faces and one sapphire window on a face perpendicular to the other two windows. The windows were secured to the stainless steel block with ultraviolet curing epoxy (Norland Optical Adhesives 81) such that the vessel could be evacuated and filled with a sample vapor. Fixturing for evacuation and cleaning were also machined into the block. A Peltier junction could be attached to a plain face of the vessel for temperature control. Additional gas and vacuum control components were assembled for filling and evacuation of the vessel. Initial trials investigating Raman scatting intensities for ambient atmospheric nitrogen and oxygen Raman scatter demonstrated major limitations in obtaining vapor sample Raman spectra with our laser source, coupling efficiency, and imaging method. These limitations arise from the low scattering cross-sections typical of gas and vapor phase sample species. Observation of the vibrational Raman of nitrogen required significant incident laser power for illumination at $357\,nm$ and long image acquisition time ($> 2\,min$). While the acquisition time is manageable, the laser power limitation is the primary limiting factor in obtaining vapor phase Raman spectra for tunable excitation. The nitrogen spectra were obtained using the pump source for the optical parametric oscillator (OPO), not the tunable signal of the OPO. The pump source power is significantly larger than the OPO signal power and to observe any Raman spectra for nitrogen required both hard driving of the OPO system (which could damage the OPO system) and long image acquisition times ($> 10\,min$). These factors made gas and vapor sample investigation even with resonance enhancement impractical for our experimental arrangement (in hind-sight).

Illumination of the liquid samples held in the sample container depicted in Figure 3.1 posed an additional problem. The initial spectra collected utilizing the sample holder (and another similar sample container) showed the Raman spectral features of the sample

container itself. The sample container is made of polytetrafluoroethylene (PTFE) which has distinct spectral features occurring nearby significant spectral features of several of our sample species. The sample itself acts as a waveguide for the excitation light while in the sample container and couples the excitation light onto the PTFE sample cell surface. The corresponding Raman scattered signal from the sample container adds spectral features which are easily detected and identified; however they are still undesirable. A solution for this problem is to mask the excitation light from the internal surface of the sample container by using an aluminum shroud inside the sample holder; since the metal surface does not contribute a Raman scattering signal.

3.3 Data Acquisition

Both the SPEX and Instruments SA spectrometers utilize computer control for wavelength tuning. The Instruments SA system utilizes routines from a custom, in-house data acquisition package written in the graphical programming language *LabView* from National Instruments Corporation. These routines are part of a larger set of data acquisition and control programs authored by Dr. Hans Hallen entitled *Data Taker*. The SPEX system, loaned by Dr. Robert Nemanich, is controlled by a dedicated computer interface and software supplied by the manufacturer. The spectrometer detector images for both systems used a charge-coupled device (CCD) camera. The initial experimental trials used a Santa Barbra Instrument Group (SBIG) CCD-UV Model ST-6 camera with software control provided by the lab's *Data Taker* suite. After these initial trails, another imaging system become available courtesy of Michigan Aerospace Corporation. This instrument is an ANDOR iXon^{EM} DU-897 (with back illumination) with a PCI card interface and software from the manufacturer. The images were stored as standard FITS format files and processed using MATLAB and the open source statistical analysis package `R`. The processing and analysis algorithms are discussed in Chapter 4.

The ANDOR camera was designed with a precision temperature control to regulate the CCD element's operating temperature over a large range from ambient temperature. The camera is equipped with an inboard fluid heat exchange which operated with circulating water to provide consistent operation of the CCD at $-80\,^{\circ}C$ using room temperature coolant water. The SBIG camera was designed with a modest CCD temperature control limited primarily by ambient temperature. The camera was fitted with a fluid heat exchange by

a prior graduate student (Eric Ayers) to allow additional cooling. With additional cooling, the SBIG camera could maintain a stable CCD operating temperature of approximately $-40\,^{\circ}C$ provided the liquid coolant was near $0\,^{\circ}C$. The heat exchange was improved by an undergraduate student (Ryan Neely, III) to better couple the camera's Peltier junction to the heat exchange to permit lower CCD operating temperature. However stable operating temperature of the SBIG camera was cumbersome due to the requirement that the coolant also have a stable temperature and limited the consistent operating temperature to approximately $-45\,^{\circ}C$ over long (several hours) data collection trials. The need for the lowest possible CCD operating temperature is due to the temperature dependence of the dark counts of the CCD; the dark current, D, can (to first approximation) be expressed as: $D = D_0 \exp(-\Delta E/kT)$, where ΔE is the activation energy of the CCD substrate, k is Boltzmanns constant, and T the absolute temperature (D_0 empirically determined) [Widenhorn et al., 2001]. By reducing the temperature of the CCD, we can increase data acquisition time without introducing too much noise into the image. Table 3.2 list some of the relevant camera parameters. The overall gain in using the ANDOR camera is expediency.

Table 3.2: Comparison of SBIG and ANDOR camera parameters.

Parameter	SBIG [SBIG, 1996]	ANDOR [Andor, 2008]	Units
Image Size	8.6×6.5	8.2×8.2	mm
Pixel Size	23×27	16×16	μm
Pixel Area	375×242	512×512	$pixel$
Readout Noise	30	25	$e^- \; rms$
Full Well Capacity	400	800	$ke^- \; max$
Saturation	$2^{16} - 1$	Variable by Gain	counts
Read Bit Resolution	16	16	bit
Average Operation Temperature	-45	-80	$^{\circ}C$, thermoelectric

3.4 Optical Parametric Oscillator

The tunable light source, we utilized an optical parametric oscillator (OPO) from U-Oplaz (OPO BBO-3B + BBO-SHG Type I, Model S) [U-O, 1999]. The tuning range is from $210\,nm$ to $2\,\mu m$ with an average power of approximately $0.25\,mW$ to $15\,mW$ across this range respectively. The OPO system is pumped using the third harmonic ($354.7\,nm$) of a pulsed, Q-switched Quanta Ray INDI-50-10 Nd:YAG laser from Spectra-Physics. The

laser has a $8\,ns$ pulse width with a repetition rate of $10\,Hz$ and maximum power of approximately $6\,W$ [Spe, 1998]. Our experimental trials restricted the maximum laser power to approximately $4\,W$ to minimize the possibility of damaging optical components in the OPO system. Figure 3.3 details the arrangement of our system. The remainder will outline the basic theory and operation of the OPO system. Excellent coverage of theory of nonlinear optics is given in Yariv, [Yariv, 1975], and an engineering approach on laser systems (including nonlinear optical systems) is given in Kuhn [Kuhn, 1998]. Coverage of nonlinear optics theory and materials is provided in Sutherland [Sutherland, 2003], Boyd [Boyd, 1992], and Dmitriev et al. [Dmitriev et al., 1999].

Figure 3.3: Schematic of the NCSU OPO system.

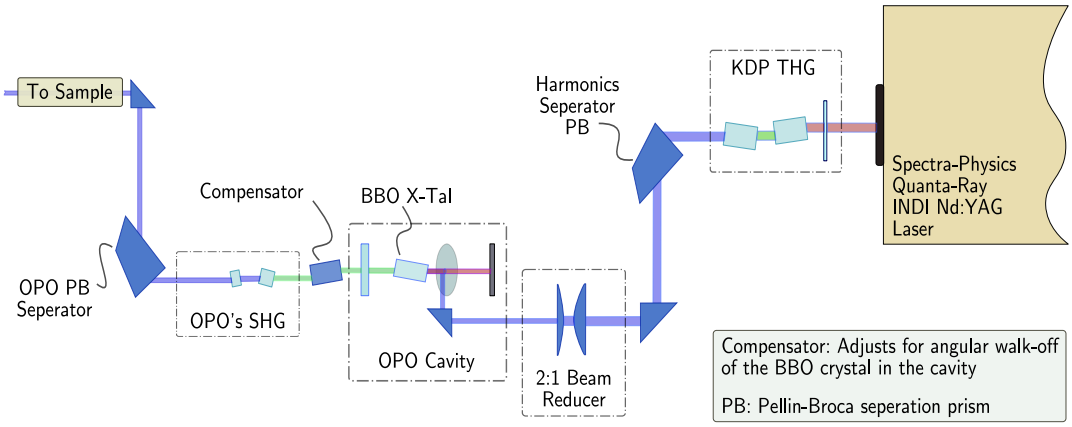

3.4.1 Phase-Matching Conditions

Optical parametric oscillators share similarities with laser cavities. Light from an OPO cavity is highly monochromatic, coherent, displays laser speckle and the beam profiles are typically Gaussian and propagate in $\mathrm{TEM}_{0,0}$ mode [Kuhn, 1998]. Optical parametric oscillation arises from the nonlinear optical susceptibility tensor, χ_{ijk}, and is specifically a second order process, $\chi^{(2)}_{ijk}$, as with frequency doubling and sum/difference frequency generation. The electric polarization for a nonlinear material, $\mathbf{P}(\vec{r},t)$, can be expressed as,

$$\mathbf{P}(\vec{r},t) = \chi^{(1)}\mathbf{E}(\vec{r},t) + \chi^{(2)}\mathbf{E}^2(\vec{r},t) + \chi^{(3)}\mathbf{E}^3(\vec{r},t) + \cdots , \tag{3.4.1}$$

where $\mathbf{E}$ represents the electric field interacting with the nonlinear medium. Substitution of $\mathbf{P}(\vec{r},t)$ into Maxwell's equations and solving the wave equations for the appropriate

boundary conditions yields the phase-matching conditions:

$$\mathbf{k}_3 = \mathbf{k}_1 + \mathbf{k}_2 \quad \text{with,} \tag{3.4.2}$$

$$|\mathbf{k}_j| = \frac{n(\omega_j)\omega_j}{c}, \quad \text{and more generally,} \tag{3.4.3}$$

$$\omega_3 = \omega_1 + \omega_2. \tag{3.4.4}$$

Depending on the nonlinear material, this phase-matching can become rather complicated. Equation (3.4.2) gives the most general form for the phase-matching condition, vector phase-matching, where the field propagation directions may not necessarily be collinear. Scalar phase-matching is the least complicated with respect to the apparatus [Sutherland, 2003]. Our system utilizes scalar phase-matching (Equation (3.4.4)) where the field propagation vectors are collinear. The remaining discussion will assume scalar phase-matching. The phase-matching condition is equivalent to the conservation of energy for the associated photons, $E = \hbar\omega = h\nu$. The OPO process is parametric since by adjustment one of the ω_i, energy conservation requires the others to change. Parametric oscillation uses an oscillation at one frequency to drive the oscillation of two other distinct frequencies. Placing a nonlinear crystal into an optical resonator with resonating modes for the ω_1 (signal) or ω_2 (idler) waves or both lead to parametric oscillations in these modes [Yariv, 1975]. At a certain threshold level, the resonator cavity loss balances the cavity's gain and any additional energy input is delivered to the signal and idler oscillations. This results in a frequency variable cavity whose output is modulated by the phase-matching conditions, (3.4.4), of the crystal.

3.4.2 Nonlinear Crystal Properties

Birefringent crystals are attractive for use in nonlinear light generation. Birefringent crystals exhibit double refraction, due to the existence of two indices of refraction, depending on the direction transversed in the crystal [Fowles, 1968]. The indices of refraction are termed ordinary index of refraction and extraordinary index of refraction. Phase-matching with a birefringent crystal is accomplished when the field propagating along the direction of the ordinary index of refraction is equivalent to that propagating along the direction of the extraordinary index of refraction, or $\Delta n = n_e - n_o = 0$, where e and o specify extraordinary and ordinary respectively.[3] Several methods can be utilized to change the

[3]This could also be accomplished using mixed polarization for the incident field as the ordinary and extraordinary ray propagations are polarization dependent.

refractive indices of birefringent crystals including temperature variation, acoustic modulation, piezoelectric modulation, and angular rotation of the crystal. The most economical scheme is to utilize angular tuning, as with our system; however this economy comes at a price. Angular tuning is susceptible to the walk-off of the output beam due to the light propagation path through the material, a problem more significant for long crystal dimensions. Depending on the crystal material, the conversion efficiency and tuning range available can vary appreciably.

Nonlinear crystals are classified based on their spatial symmetry. The spatial symmetry effectively determines which elements of the susceptibility tensor are non-zero [Boyd, 1992]. These crystal classes influence the usefulness of a material for particular schemes of nonlinear light generation and the phase-matching conditions. Crystals utilized for most nonlinear light generation belong to either the biaxial or uniaxial classes. Our system utilizes two different uniaxial crystals and the axes conventions are illustrated in Figure 3.4. A nonlinear crystal is specified by a cut (its phase-matching angles), defined by the angular values θ and ϕ. These angles relate to the elements of the susceptibility tensor, $\chi^{(2)}_{ijk}$ are given in a contracted notation, $d_{ijk} = \frac{1}{2}\chi^{(2)}_{ijk}$. In our system we use beta

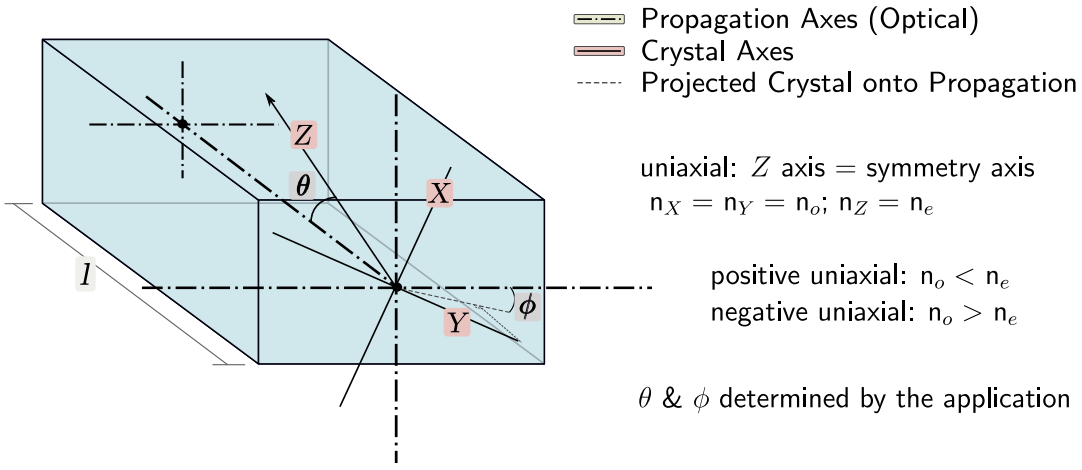

Figure 3.4: Illustration of uniaxial nonlinear crystal conventions.

barium borate (BBO), β-BaB_2O_4, and potassium dihydrogen phosphate (KDP), KH_2PO_4.

Initially the system was exclusively BBO, however mechanical damage to the second (2ω) and third (3ω) harmonic generator crystals for the Nd:YAG laser resulted in using a set of KDP crystals for the second and third Nd:YAG harmonics. Both crystals are negative uniaxial ($n_o > n_e$), with BBO belonging to the $3m$ symmetry class and KPD belonging to the $\bar{4}2m$ symmetry class [Dmitriev et al., 1999]. Figure 3.5 shows the calculated ordinary and extraordinary refractive indices of BBO and KDP given by their Sellmeier's equations (3.4.5), with the shaded regions indicating the possible phase-matching values [Dmitriev et al., 1999; Nikogosyan, 1991].

$$BBO: \begin{cases} n_o^2 = 2.7359 + \dfrac{0.01878}{\lambda^2 - 0.01822} - 0.01354\lambda^2 \\ n_e^2 = 2.3753 + \dfrac{0.01224}{\lambda^2 - 0.01667} - 0.01516\lambda^2 \end{cases}$$

$$KDP: \begin{cases} n_o^2 = 2.259276 + \dfrac{13.00522\lambda^2}{\lambda^2 - 400} - \dfrac{0.01008956}{\lambda^2 - 77.26408^{-1}} \\ n_e^2 = 2.132668 + \dfrac{3.2279924\lambda^2}{\lambda^2 - 400} - \dfrac{0.008637494}{\lambda^2 - 81.42631^{-1}} \end{cases} \tag{3.4.5}$$

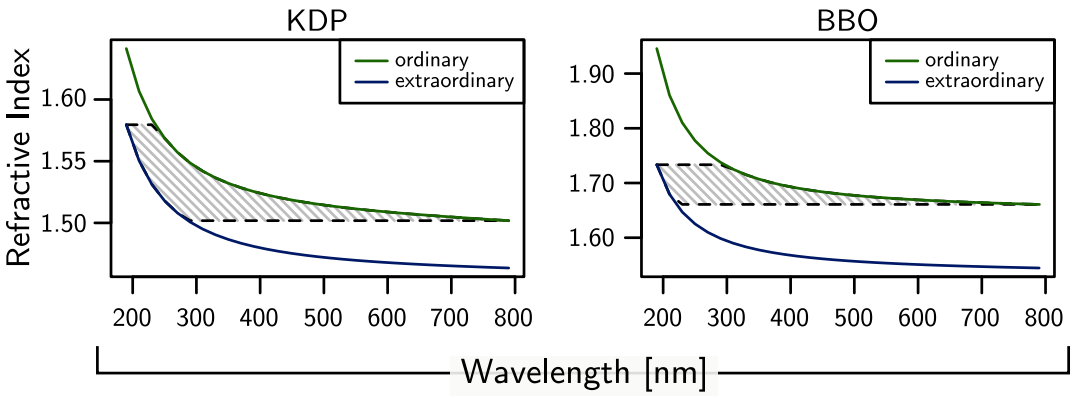

Figure 3.5: Sellmeier's dispersion for KDP (left) and BBO (right) between $190\,nm$ and $800\,nm$. Shaded regions indicate values conducive to phase-matching.

3.4.3 Angular Tuning Curves

Due to birefringence, phase-matching will only occur for certain values of the refractive indices given by the Sellmeier's equations (3.4.5). The birefringence introduces an angular dependence to the Sellmeier's equations for an incident wave. This yields angular tuning curves for the crystals. For uniaxial crystals, the tuning angle, θ, is given by solving

$$\frac{1}{n_e^2(\theta)} = \frac{\cos^2\theta}{n_o^2} + \frac{\sin^2\theta}{n_e^2}. \tag{3.4.6}$$

The polarization relationship between the pump, idler, and signal beams in the OPO system are also important to consider. The polarization state of the beams determines the crystal cut and tuning angle range available for specific crystal materials. The convention for describing this relationship references the polarization in terms of crystal's refractive index directions. The ordinary and extraordinary index directions are orthogonal inside uniaxial crystals and as such the convention describes the polarization state of each of the beams in terms of what direction it propagates in the crystal. The notation for our system is given as:

$$\underset{lab\ axes}{(x,y,z)} \rightarrow \mathcal{L}\,\underset{crystal\ axes}{(X,Y,Z)} \rightarrow (\text{ooe}) \rightarrow (\text{idler, signal, pump}),$$

where $\mathcal{L}$ projects the crystal axes onto the lab axes.

Our system utilizes the (ooe) configuration, which is a Type I phase-matching configuration. Solving Equations (3.4.4) and (3.4.6) provides the phase-matching angle, θ_{pm}.

$$\frac{n_e(\theta,\lambda_p)}{\lambda_p} = \frac{n_o(\lambda_s)}{\lambda_s} + n_o(\lambda_i)\Big(\frac{1}{\lambda_p} - \frac{1}{\lambda_s}\Big) \quad (\text{ooe}) \tag{3.4.7}$$

Calculated angular tuning curves based on Equations (3.4.5), (3.4.6), and (3.4.7) are shown in Figure 3.6. In the angular tuning, the phase-matching angle will reach a maximum value, called the degeneracy point, which bounds the upper limit on the signal wavelength. The crystal type and cut can be selected to accommodate a range of phase-matching schemes. As previously mentioned, we utilize two types of crystals. The crystal parameters for BBO are listed in Table 3.3.[4]

[4]The crystal parameters for the KDP crystals is unknown. Only the polarization states of the exiting fundamental, second and third harmonics for the Nd:YAG laser light are known. The KDP crystals are Type I phase-matching.

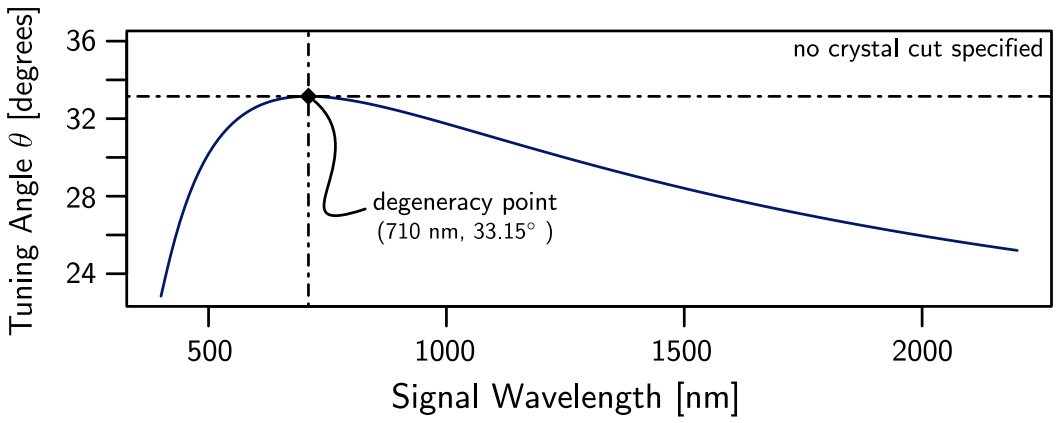

Figure 3.6: Theoretical angular tuning curve for BBO in the Type I (ooe) phase-matching scheme.

Table 3.3: BBO crystal parameters for the NCSU OPO system.

Use	Cut Angles θ	ϕ	L,W,H in mm
YAG SHG	22.8°	0°	7,9,9
YAG THG	31.3°	0°	6,9,8
OPO	30°	0°	17,7,5
OPO SHG_1	56°	0°	5,10,7
OPO SHG_2	36°	0°	5,10,7

3.4.4 Output Characteristics

When the field propagation and polarization directions are fixed (as with our system), the nonlinear polarization $\mathbf{P}(\vec{r},t)$ can be expressed as a scalar quantity,

$$P(\omega_3) = 4d_{eff}E(\omega_1)E(\omega_2), \tag{3.4.8}$$

where d_{eff} is the effective value of the second order susceptibility tensor (in reduced notation). The calculation of the propagation fields, power, intensity, and conversion efficiencies are greatly simplified using d_{eff}. Additionally should the lowest resonant frequency of the system be much greater than the optical frequencies encountered in the nonlinear interactions, the nonlinear susceptibility becomes approximately independent of frequency. This is termed Kleinman symmetry and for many nonlinear materials this approximation is valid

within the ultraviolet through infrared region ($150\,nm$ to $2.5\,nm$). Table 3.4 lists the relevant d_{eff} expressions for BBO and KDP, with θ equal to the phase-matching angle. The

Table 3.4: Values of d_{eff} for BBO and KDP for common phase-matching schemes under Kleinman symmetry approximation.

Polarizations	BBO ($3m$)	KDP ($\bar{4}2m$)
ooe, oeo, eoo	$d_{15}\sin\theta - d_{22}\cos\theta\sin 3\phi$	$-d_{14}\sin\theta\sin 2\phi$
eeo, eoe, oee	$d_{22}\cos^2\theta\cos 3\phi$	$d_{14}\sin 2\theta\cos 2\phi$

expressions listed in Table 3.4 can be used to estimate the conversion efficiencies of the nonlinear processes in the system, including the harmonic stages of the Nd:YAG laser, the OPO and the second harmonic stages of the OPO. Sutherland [Sutherland, 2003] and Dmitriev et al. [Dmitriev et al., 1999] outline several approaches to obtaining these efficiencies. The efficiencies at the different stages of the light generation chain are not linearly related to one another and the relationships can be determined theoretically. Measurements have been taken at the different stages in our system to estimate the composite conversion efficiency from Nd:YAG laser output to ultraviolet OPO output. These measurements were taken after the installation of a new OPO BBO cavity crystal with KDP SHG/THG Nd:YAG stages using an Ophir Nova power meter averaging for 30 seconds.

$$\underset{pump:\,355\,nm}{(270\,mW)} \rightarrow \underset{signal:\,440\,nm}{(14.7\,mW)} \rightarrow \underset{UV:\,220\,nm}{(0.45\,mW)}$$
$$\text{usual UV operation power} \approx 3\,mW \tag{3.4.9}$$

BBO has a more favorable nonlinear conversion efficiency compared to KDP. Using KDP in the second and third harmonic stages of the Nd:YAG has compromised the overall conversion efficiency. We have observed the increased conversion efficiency using BBO in the second and third harmonic stages. A simple performance estimate of conversion efficiency for second harmonic conversion in BBO and KDP is possible and is illustrated in Figure 3.7. The second harmonic power conversion efficiency can be estimated using (3.4.10) for crystal length L and incident power density PD:

$$\eta_{shg} = \tanh^2\Big(\frac{L}{L_{nl}}\Big), \quad L_{nl} = \frac{1}{\sigma a_0}, \quad \sigma = \frac{8\pi^2 d_{eff}}{n_\omega \lambda_\omega}, \text{ and } \quad a_0 = \sqrt{\frac{752(PD)}{\pi n_\omega}}, \tag{3.4.10}$$

where L_{nl} is the effective nonlinear length of the crystal [Dmitriev et al., 1999]. In Figure 3.7 the conversion efficiencies are compared for variations in power density and crystal

length. Clearly BBO provides better second harmonic generation performance than KDP for equivalent incident power densities and crystal lengths. A trade-off exists between power density and crystal length. Obviously for appreciably long crystals, the conversion performance of both types of materials approach unity. Effectively all incident photons are converted. However long crystals can experience significant walk-off and are prone to inhomogeneous heating as incident power is applied to the crystal [Dmitriev et al., 1999]. To improve beam quality and retain high conversion efficiency, short crystal lengths are desirable with modest incident power densities applied. In this case BBO is a superior choice to KDP. The trade-off between power density and crystal length comes at the expense of power damage threshold however. KDP is known to have a high power damage threshold ($> 5GW\,cm^{-2}$ at $1064\,nm$ for $10\,ns$), whereas BBO has a modest damage threshold of ($\sim 1GW\,cm^{-2}$ at $1064\,nm$ for $10\,ns$) [Dmitriev et al., 1999]. The damage threshold can affect the total power conversion efficiency of a system by limiting the incident power density. The performance estimates from (3.4.10) provide a guide to choosing crystal material and establishes limits for power densities at different stages in the system. For our system, BBO is an optimal choice in all stages of the light generation. Overall a high conversion efficiency in the early stages of the light generation chain yield improved beam quality in the later stages and result in reduced wear and tear on the nonlinear crystals throughout the system. Figure 3.8 details the elements of our OPO cavity, with Figure 3.9 showing the OPO cavity during operation.

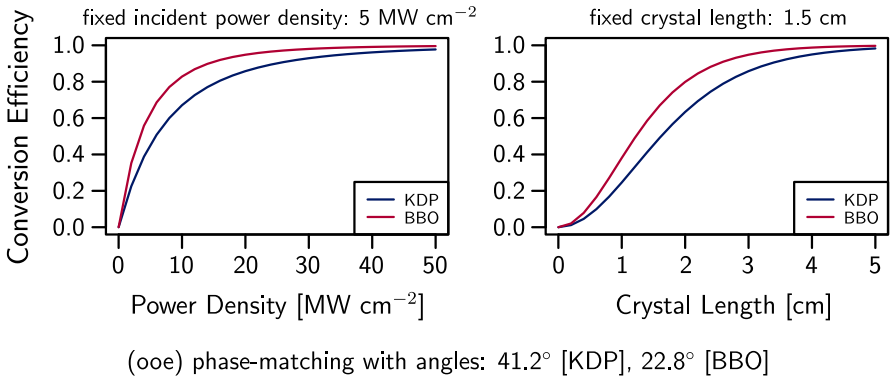

Figure 3.7: Theoretical power conversion efficiency of KDP and BBO for different incident power densities and crystal lengths.

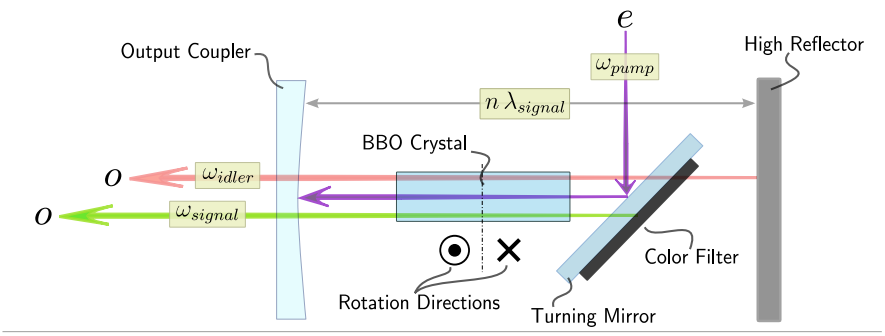

Figure 3.8: Configuration of the Type I phase-matching OPO cavity of the NCSU OPO system.

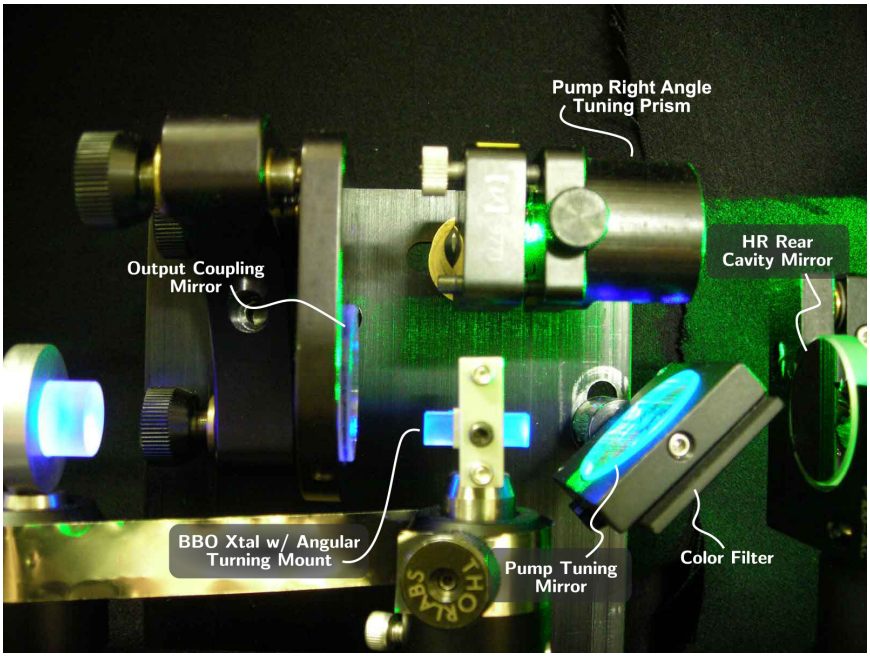

Figure 3.9: The NCSU OPO system in operation. The Nd:YAG laser and SHG/THG system are on right concealed by protective fabric.

3.5 Spectrometer Model

3.5.1 Overview

For proper processing of the camera image data, several corrections need to be considered. One of those corrections requires an understanding of the contribution of the spectrometer spectral efficiency in the image data. To gain an insight into this contribution, a simple model of the spectrometer spectral efficiency has been developed based on the cumulative spectral efficiencies of the spectrometer optics and CCD camera. The motivation for this model is due to the lack of reported spectral efficiency data for the spectrometer either from the literature or by experimental observation. Future experimental work should establish a robust calibration of the spectrometer system utilizing broadband calibrated light sources. We believe the following model is sufficient to describe the behavior of the spectral efficiency, although the actual numerical values may be different. As a point of reference for the overall spectral efficiency, the initial work done by Asher on ultraviolet resonance Raman utilized the same spectrometer we have used for our data collection, excluding the CCD camera [Asher, 1993a]. Rigorous development of a spectral efficiency model would include the complex modeling of the diffraction gratings [Loewen and Popov, 1997]. Such a model would involve the solution of Maxwell's equations on the grating surface and the subsequent calculation of the propagating fields in the far-field limit. While there are several techniques for calculating these grating equations, the process is time intensive. Additionally, empirical spectral efficiency curves are available for the spectrometer grating; thus a rigorous calculation of these efficiency curves is not necessary. The routines used to calculate the parameters were written using the data analysis package `R`.

3.5.2 Spectrometer Characterization and Specifications

Table 3.5 summarizes the manufacturer's specifications of our Spex Triplemate spectrometer. This is a triple stage instrument, comprised of a double stage input monochromator and a final $0.6\,m$ focal length principle spectrometer stage in an asymmetric Czerny-Turner configuration. The triple stage design offers excellent stray light rejection courtesy of the double monochromator stage coupled with the long focal length of the main stage providing good spatial separation. This makes the instrument ideal for Raman spectroscopy studies where the signal light usually has a much lower intensity compared to the excitation

Table 3.5: Spex Triplemate 1877 spectrometer specifications utilized in the spectral efficiency estimate, from [Spex, 1985].

Spectrometer Nominal Coverage Bandpass			**Filter Nominal Bandpass,** $[1200\,gr/mm]$ **@** $514\,nm$	
Grating $[gr/mm]$	Spectral Coverage $[nm/25mm]$	Bandpass $[nm/25\,\mu m]$	slit$[mm]$	Bandpass$[nm]$
1200	35 (@ $514\,nm$)	0.035	0.5	1.4
2400	17 (@ $357\,nm$)	0.017	1.0	2.7
3600	11.5 (@ $250\,nm$)	0.11	2.0	5.5
			5.0	14

Other Parameters	
wavelength accuracy:	$\pm 0.5\,nm$
wavelength resettability:	$\pm 0.2\,nm$
linearity:	$\pm 0.5\,nm$ ($250\,nm \sim 550\,nm$)
stray light rejection:	10^{-14} @ 10 BP units from Rayleigh
focal plane:	$25\,mm \times 10\,mm$
Filter Stage:	Dual Subtractive C-T
Spectrometer Stage:	Asymmetric C-T

light. A schematic of the instrument is given in Figure 3.10.

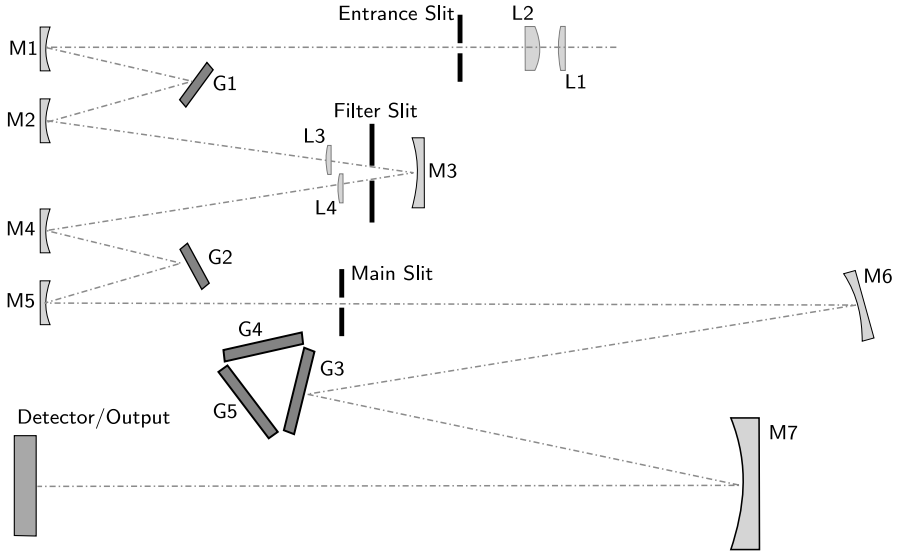

Figure 3.10: Schematic of the Spex Triplemate 1877 spectrometer. M, L, and G represent the mirrors, lenses, and gratings respectively.

Characterization of the spectrometer begins by considering the dispersion properties of its main stage. To begin, the angle conventions for the dispersion calculations are defined by

Equations (3.5.1) and illustrated in Figure 3.11 [Radziemski, 1981].

$$\begin{aligned} \theta &\equiv \text{grating rotation from zero order (turret angle)} \\ \phi = \arctan(\tfrac{L}{2f}) &\equiv \text{instrument angle, fixed for instrument} \\ i = \theta + \phi &\equiv \text{angle of incidence} \\ r = \theta - \phi &\equiv \text{angle of diffraction} \end{aligned} \tag{3.5.1}$$

Using these angle conventions, (3.5.1), the classical grating equation and the related dis-

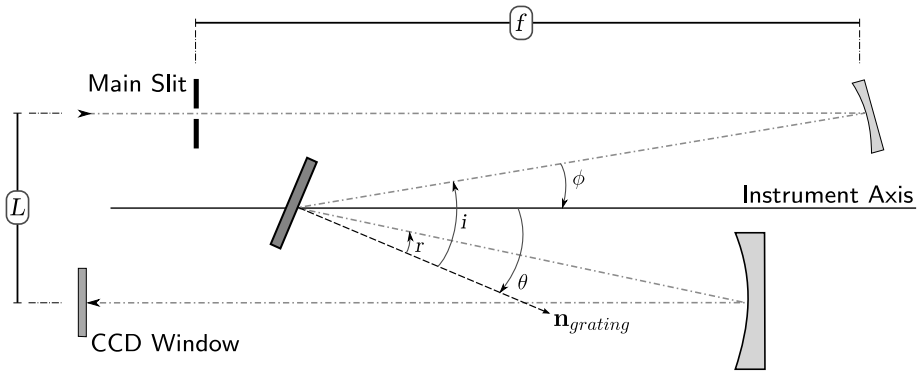

Figure 3.11: Angle conventions for the Czerny-Turner configuration. The angles of incidence (i) and diffraction (r) are both positive angles referenced from the grating normal, $n_{grating}$.

persions are expressed as (3.5.2) [Hecht, 2002; Gross, 2005; Radziemski, 1981]. The usual definitions of angular dispersion, (3.5.2b), and linear dispersion, (3.5.2c), apply to describe the rate at which the wavelength sweeps across the exit pupil (CCD window in our system) as the grating is rotated. The angular, linear, and reciprocal linear dispersions are properly calculated for fixed angles of incidence i [Radziemski, 1981]. This condition requires all of the parameters then to have a dependence on the physical rotation angle or turret angle θ of the spectrometer. For the specifications of our system, Figure 3.12 shows the linear dispersion for two wavelengths within the range extremes of our image data series.

$$m\lambda = d(\sin i + \sin r) \tag{3.5.2a}$$

$$\frac{dr}{d\lambda} = \frac{1}{\lambda}\frac{\sin i \pm \sin r}{\cos r} \tag{3.5.2b}$$

$$\frac{dx}{d\lambda} = f\frac{dr}{d\lambda} \tag{3.5.2c}$$

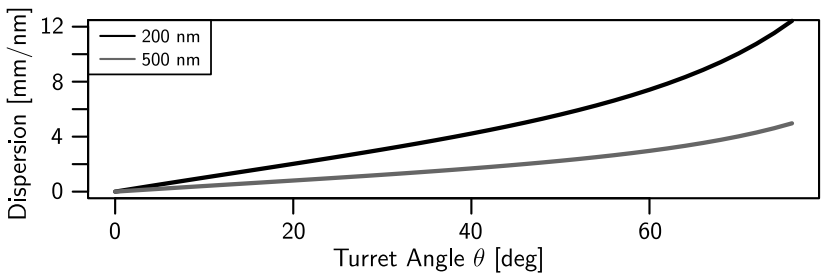

Figure 3.12: Dependence of the linear dispersion on turret angle for a $2400\,gr/mm$ grating, an instrument angle $\phi \approx 13°$, and diffraction order $m = 1$.

As we are utilizing a different CCD camera system than the original detector designed for the spectrometer, some considerations are in order to determine what is observed in our image data and how this relates to the spectrometer parameters. The original specifications provided by the manufacturer have the CCD detector area as $25\,mm \times 10\,mm$ compared to the area of the ANDOR CCD element which is $8.2\,mm \times 8.2\,mm$. The differences in the these CCD element sizes will change the bandpass and field of view original specifications. Using Equations (3.5.2) new specifications for the spectrometer adapted with the ANDOR camera can be easily calculated and are provided in Table 3.6. The field of view is an important parameter for comparison between the original system and the ANDOR adapted system. Due to the significantly smaller horizontal dimension of the ANDOR CCD element, the dispersion yields approximately 1/3 the wavelengths on the ANDOR CCD element as it did for the original CCD element. There is a small wavelength dependence on this window size, as anticipated by the grating equation, and Figure 3.13 shows the field of view variation for the ANDOR CCD. This variation is relevant when expressing the image data in terms of wavenumber instead of wavelength. A linear wavelength variation does not translate to a linear wavenumber variation. The observed spectra will have a larger wavenumber range in the shorter wavelengths than in the longer wavelengths. However this variation is dominated by the wavelength range, that is, the small variation in field of view is dominated by the wavelength range where the spectrometer is tuned. The window has a very small contribution, but nonetheless documented for completeness.

Table 3.6: Alternate configuration specifications for the Spex Triplemate 1877 with ANDOR camera adaptation.

$\lambda\,[nm]$	Linear Dispersion $[\frac{mm}{nm}]$	Bandpass $[\frac{nm}{8mm}]$	Window $[nm]$
200	5.52	0.0221	5.79
500	5.02	0.0201	6.38

These calculations were done with our operational grating ($2400\,gr/mm$) and our input slit of $250\,\mu m$. Instrument angle $\phi = 13.3°$ and diffraction order $m = 1$.

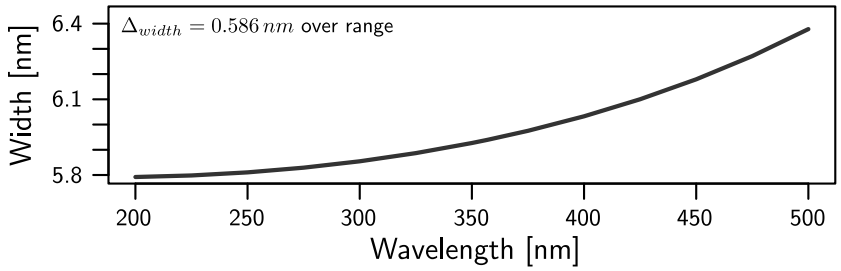

Figure 3.13: Variation of field of view with wavelength for a $2400\,gr/mm$ grating, an instrument angle $\phi \approx 13°$, and diffraction order $m = 1$.

3.5.3 Lens and Mirror Considerations

The spectrometer throughput will be effected by several types of optical elements as detailed in Figure 3.10. The parameters to consider in the estimation of the spectral efficiency are: *a*) the slit diffraction limitations, *b*) the lens transmission, *c*) the mirror reflectance, *d*) the attenuation from the anti-reflection and protective coatings, and *e*) the grating spectral efficiency. The total throughput is the compounded throughput of each element in the spectrometer and is represented by (3.5.3),

$$I_{output} = \left(\prod_{m=1}^{m\,mirrors} (R_m) \prod_{l=1}^{l\,lenses} (T_l) \prod_{g=1}^{g\,gratings} (\eta_g) \right) I_{input} \tag{3.5.3}$$

where, R_m is the mirror reflectance, T_l is the lens transmittance, and η_g is the grating efficiency. The mirrors although spherical (with large radius of curvature) are treated as plane mirrors for estimating reflectance. Also all the optics are assumed to have standard broadband anti-reflection coatings. The anti-reflection coating layer thickness is unknown and with the availability of complex index of refraction data for various coating materials a simple model of the anti-reflection coating layer and mirror substrate is used to give the total

mirror reflectance [Hass and Waylonis, 1961; Smith et al., 1985; Cotter et al., 1991]. The calculation of the Fresnel coefficients for the spectrometer mirrors and lenses including thin layer anti-reflection films are done utilizing the transfer matrix method given in Equation (3.5.4) [Fowles, 1968].

$$M = \begin{bmatrix} \cos\beta & \frac{\imath}{p}\sin\beta \\ \imath p \sin\beta & \cos\beta \end{bmatrix}, \qquad M \begin{bmatrix} 1 \\ \mathcal{N}_t \end{bmatrix} t = \begin{bmatrix} 1 \\ \mathcal{N}_0 \end{bmatrix} + \begin{bmatrix} 1 \\ -\mathcal{N}_0 \end{bmatrix} r$$
$$k = \frac{2\pi}{\lambda}, \quad \beta = kl\cos\theta, \quad p_s = \mathcal{N}_i \cos\theta, \quad p_p = \frac{\mathcal{N}_i}{\cos\theta} \tag{3.5.4}$$

where, $\mathcal{N}$ is the complex index of refraction, M is the transfer matrix, t is the transmission coefficient, r is the reflectance coefficient, l is the layer thickness, θ is the incidence angle, $\mathcal{N}_{0,i,t}$ are the ambient, layer, substrate complex indices of refraction, respectively. The resultant reflectance behavior of the mirror reflectance are in agreement with the manufacturer's reflectance profiles. The spectrometer lenses are made with anti-reflection coated fused silica (specifically Dynasil$^{\text{TM}}$) however no transmission profile was available from the manufacturer. Small variation in the lens transmission is not expected to have a significant impact on the composite throughput. The estimated transmission for the spectrometer lenses is in agreement with similar transmission profiles for anti-reflection coated fuse silica. The resultant mirror reflectance and lens transmittance profiles are shown in Figures 3.14 and 3.15 respectively. Table 3.7 lists a summary of the parameters.

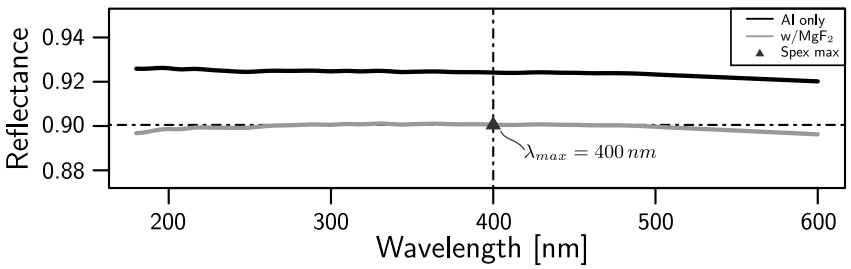

Figure 3.14: Estimated reflectance profile for an anti-reflection coated aluminum mirror.

3.5.4 Diffraction Grating Considerations

Most of the throughput attenuation in the spectrometer is attributable to the reflection losses of the diffraction gratings in the filter and main stages. Diffraction gratings

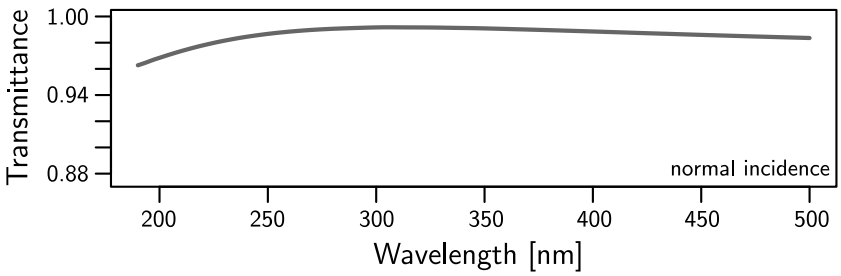

Figure 3.15: Estimated transmittance profile for an anti-reflection coated fused silica lens.

Table 3.7: Calculated mirror and lens parameters.

	AR Layer Thickness [nm]	Correction	Our Estimate	SPEX Specification	Average Reflectance
Mirror	3.65	0.977	0.901 @ 428 nm	0.9 @ 400 nm	0.899
Lens	55.9	0.722	0.992 @ 306 nm	N/A	0.010

Mirror reflectance is specified $> 82\%$ over the region of interest and optimized to $> 85\%$ at 250 nm.

have complex reflectance profiles depending on the wavelength range and polarization state of the incident light [Johnson, 1981; Li, 1996, 1993; Li et al., 1999; Margelevičius et al., 2003; Moharam et al., 1995; Nakata and Koshiba, 1990]. Solution of Maxwell's equations at the grating surface for even a simple blazed grating is not a straightforward exercise. A survey of the different methods for solving Maxwell's equations for the grating's boundary conditions reveals significant shortcomings in each methodology particularly in respect to the polarization state of the incident fields. Fortunately, a robust solution is not necessary as the manufacturer has supplied us with the grating spectral efficiency curves, tracked by the component serial numbers [Spex, 1999, 2000]. The nature of the scattered light from the experimental sample is considered to be unpolarized, therefore we consider the average of the s- and p- polarization spectral efficiency curves. Not included in the spectral response of the gratings is the influence of the grating age and possible contaminations from fingerprints, dust, and oxidation. These are difficult to estimate due to our uncertainty in the instruments handling, however given the history of the instrument we feel these effects are minimal. Figure 3.16 shows the unpolarized efficiency curves for the spectrometer system using 1200 gr/mm for the two filter stage gratings and 2400 gr/mm for the main stage grating. The gratings share the same blaze wavelength (250 nm) and operate in first

order ($m = 1$).

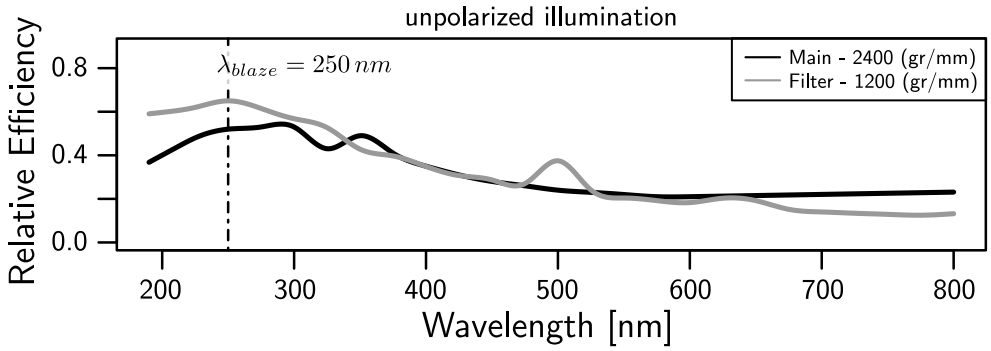

Figure 3.16: Spectral efficiency profiles for the filter and main stage diffraction gratings.

3.5.5 Camera Considerations

The final component to consider in the spectrometer spectral response is the CCD element of the camera. The quantum efficiency of the CCD element for the ANDOR camera system was supplied by the manufacturer. Figure (3.17) shows the quantum efficiency for the camera CCD array.

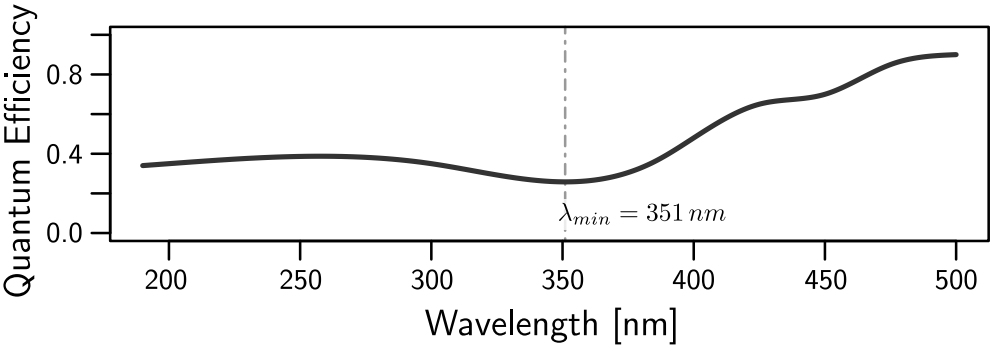

Figure 3.17: ANDOR camera CCD array quantum efficiency.

3.5.6 Final Spectral Efficiency Results

The total spectral efficiency of the spectrometer system follows from Equation (3.5.3). Figure 3.18 shows the spectral efficiency with and without including the camera responsivity. These data series are easily incorporated into the data correction routines. As a summary of the behavior of the spectrometer spectral efficiency, Table 3.8 lists the average and extreme values over our wavelength region of interest.

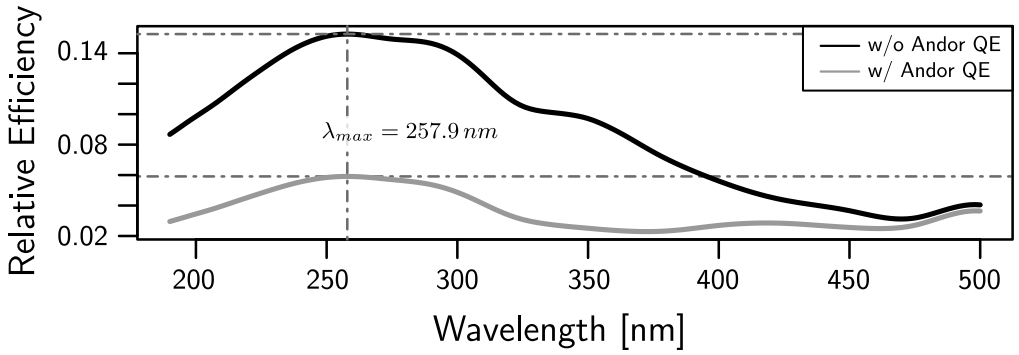

Figure 3.18: Estimated total spectral efficiency of the SPEX spectrometer system.

Table 3.8: Summary of the estimated spectrometer spectral efficiency (η) statistics.

	η_{avg}	$\eta_{avg\,in\,uv}$	η_{min}	η_{max}
w/ ANDOR	0.0906	0.116	0.0311	0.153
w/o ANDOR	0.0362	0.0403	0.0229	0.0591

Mean values in the ultraviolet are from $200\,nm$ to $400\,nm$.

Chapter 4

Methods

4.1 Overview

This chapter presents the image data processing and data analysis algorithms. These routines are developed using MATLAB and the open-source and freely available mathematical programming environment, `R`. The routines outlined are available through the courtesy of the NSOM lab. The absorption correction model is introduced. Sources of experimental uncertainty and error propagation equations are also discussed.

4.2 Image Processing

Figure 4.1 provides an example of the typical image file from the ANDOR camera. Image data from the SBIG camera is not included in this discussion due to significant differences in the processing routines and the broad availability of ANDOR camera image data for all investigated sample materials. The benefits to utilizing the ANDOR camera were speed in the image acquisition, reduced thermal noise, and the convenient file format of the image data. These image files are stored as `---.fits` files of approximately one megabyte in size. The `.fits` format stands for Flexible Image Transport System and is a standard digital file format used primarily in astronomical images [Wells et al., 1981].[1] The images themselves are 512×512 arrays (one data point/CCD pixel) with the horizontal indicies, i, spanning wavelength and the vertical indicies, j, spanning effectively the exit slit height

[1] In addition [Wells et al., 1981], the curious reader is encouraged to start on the Wikipedia page for more information on the FITS format located at (as of April 24, 2009: `http://en.wikipedia.org/wiki/FITS`

and each point (i, j) having an intensity value, $\mathcal{I}(i, j)$.[2] These images are processed using a combination of software routines to yield the final data series for further analysis. The following outline describes the different operations performed to process the data series:

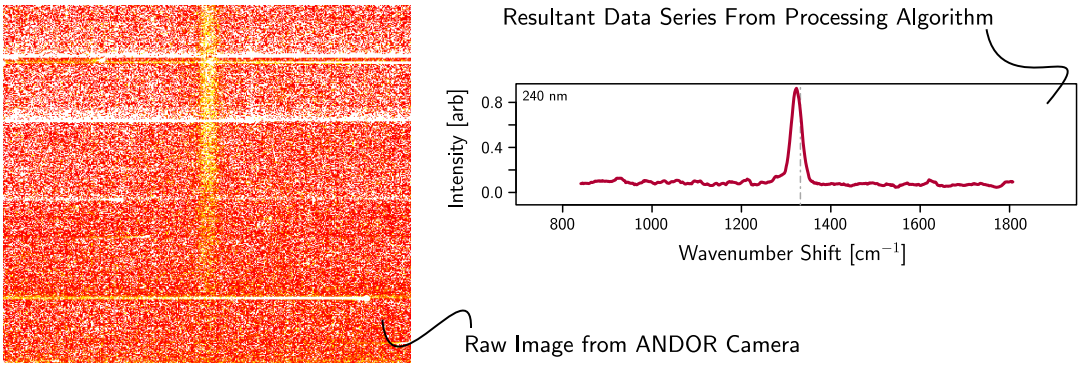

Figure 4.1: Unprocessed ANDOR camera image of the $\sim 1332\,cm^{-1}$ Stokes Raman line of diamond for $240\,nm$ excitation. Intensity scales from red (min) to white (max).

1. Spurious event exclusion: subtract bad rows from image array,
2. Column average: average remaining data down image array columns–reduces $\mathcal{I}(i, j)$ to $\mathcal{I}(i, 1)$,
3. Window smoothing: 10-point windowing average,
4. Power normalization: divide out series by average power,
5. Removal of excitation energy skew, ω_{exc}^4,
6. Background level and noise removal,
7. Fluorescence removal,
8. Removal of spectrometer wavelength efficiency skew, and
9. Self-absorption scaling (if applicable).

Steps 1-5 are accomplished using a set of MATLAB scripts written by a visiting graduate student Adam Willitsford (Pennsylvania State University, 2006-2007) [Willitsford, 2008]. Spurious event exclusion (#1) acts to remove groups of data points in the images that appear to originate in abnormal noise on the CCD. This noise is believed to originate from damage to the CCD's semiconductor electron multiplier stages. While utilizing high

[2]The exit pupil in our system is the CCD array, there is no slit.

gain amplification, the electron multiplier stages have become damaged due to a high signal intensity on the CCD element overloading the initial multiplier stages. The resulting output image, when utilizing any modest gain during acquisition, has randomly occurring streaks due to the erratic behavior of these electron multiplier stages. Also noticeable on the images are several circular rings located in the center of the image caused by damage induced by high power laser pulses into the CCD element as indicated by the group at Michigan Aerospace who loaned the camera for our investigations. We suspect this damage and the erratic behavior observed in the images are linked. The random streaks are seen in Figure 4.1 as the splotches or long horizontal lines locally saturating the image. The rows containing these are selected out using by intensity level since the desired data seldom saturate the camera and are not localized. Once the streaks are removed, the image can be averaged down (#2) the array columns yielding a (1:512) vector which is then smoothed (#3) using a low-pass filter in the form of 10-point windowing average. This window average does not introduce a lag as it replaces the data value with the average of n surrounding values. Next average power is then divided out (#4) to normalize each data series to the same power factor. The inherent excitation energy skew is divided out also (#5), since the scattering intensity has a quartic dependence on the excitation frequency.

Steps 6 and 7 are accomplished using a nonlinear curve fitting program, `fityk`. Despite the program being open-source and freely available, it is praised by the spectroscopic community. The utility of the program comes from its graphical user interface allowing visual selection of the spectrum features. For our previously processed data series, we wish to preserve as much of the original spectral content as possible so `fityk` is used only to strip away the background level (#6) and broader fluorescence (#7) from the sample and/or matrix. The background and fluorescence are slowly varying compared to the other spectral content, however algorithmically determining them is time consuming and inconsistent in our attempts. Using polynomial splines of varying degrees, we can match their observed behavior visually and intuitively inside `fityk` minimizing the potential introduction of artifacts. Occasionally peak height and center values are also obtained with `fityk`. While the center values are not expected to change significantly, we lack additional information on the spectrometer's instrument function and laser lineshape that would allow the data to be deconvolved to show just the signal spectrum [George and Willis, 1990; Smith and Dent,

2005]. Therefore fitting the spectra to any set of distributions is not expected to be yield much insight in this current investigation.

Steps 8 and 9 and the additional analysis are accomplished with custom scripts in the R language. R is a robust mathematical programming language and software environment widely used for its well developed statistical modeling capacities [Maindonald and Braun, 2003; R Development Core Team, 2008]. The spectrometer efficiency, as described in Section 3.5, is a divided out as with the power and excitation frequency normalizations. To adjust for self-absorption of the sample, several additional calculations are needed to properly account for the variances in concentration and species. These calculations are described in the next section. Most of the above processing steps are linear operations on the data series, excluding the background and fluorescence. The linearity allows easy reintroduction of removed parameters should the analysis require.

4.3 Absorption Correction Model

One of the requirements to obtain resonance enhancement on the Raman signal is that the excitation frequency fall in a high absorption region of the sample material. The gain in signal from resonance enhancement can only be determined by accounting for the absorption of the excitation and signal frequencies as they pass through the sample. Figure 4.2 illustrates the configuration and conventions used in our apparatus. Our model joins both the attenuation of the excitation and Raman signal light passing through the liquid sample into a single parameter, the effective path length (EPL), which describes the effective absorption. The calculations are shown for benzene, near the $992\,cm^{-1}$ Stokes Raman region for resonant and non-resonant excitation wavelengths at two sample concentrations, and for toluene, near the $1004\,cm^{-1}$ Stokes Raman region for resonant and non-resonant excitation wavelengths. These calculations are performed using the best high resolution absorption data available from Etzkorn et al. [Etzkorn et al., 1999] for both benzene and toluene. These absorption data are for vapor phase benzene and toluene although our experiments utilized liquid phase sample materials, as will be addressed in Chapter 6. These materials have exhibited resonance enhancement for the excitation wavelengths corresponding to a local maximum in the vapor-phase absorptions. We believe that our absorption correction model provides a very reasonable approximation to the magnitude of absorption

related attenuation for both the on resonance and off resonance regimes despite the apparent differences in the phase state of the sample media. The Beer-Lambert-Bouguer Law

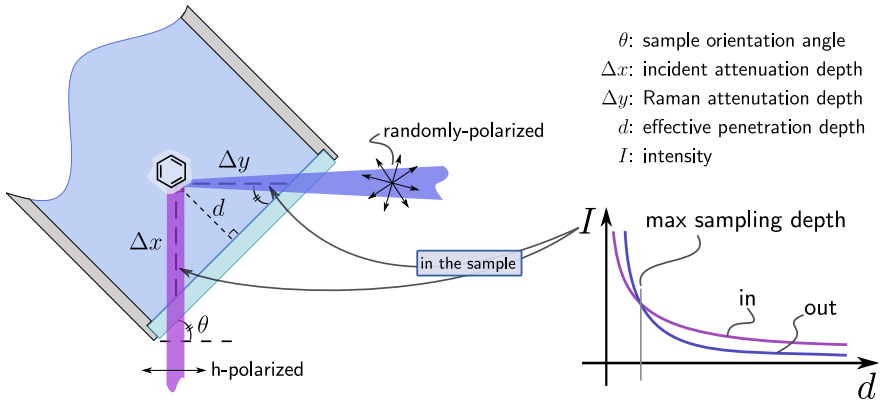

Figure 4.2: Configuration and conventions for calculating the Beer-Lambert-Bouguer Law attenuation of the excitation and scattered light.

(BLB) suggests an exponential attenuation of incident light as a function of the distance transversed in a homogeneous medium. This applies to both small concentration solutions and pure liquid species. In these cases, scattering arising from differences between solvent and solute molecule sizes is negligible. Derivation of BLB considers the ratio of the obstructed cross-section to the total cross-section as a light beam transverses the sample. The obstructed cross-section is dependent on the concentration, or number density. The intensity, I_z, at a distance z in a fluid follows as,

$$\begin{aligned} I_z &= I_0\, e^{(-\sigma N z)} \quad \text{where, } \sigma \text{ is the absorption cross-section and } N \text{ the number of absorbers or,} \\ I_z &= I_0\, 10^{(-\epsilon c z)} \quad \text{where, } \epsilon \text{ is the molar absorptivity and } c \text{ is the concentration.} \end{aligned} \tag{4.3.1}$$

The exponential form in (4.3.1) is typically used in the description of gases and pure samples, and the base-10 form in (4.3.1) is used for liquid solutions [Meyer-Arendt, 1989]. As indicated in Figure 4.2, the incident excitation radiation will experience some attenuation as it enters the sample. The Raman scattered light also experiences some attenuation (different from the incident light) as the signal exits the sample. As the incident light continues into the sample, its intensity available to generate any Raman scatter will diminish to a point where the Raman scattered light cannot exit. The combined attenuation effects establishes an effective volume from which most of the scattering interaction takes place. As

the incident beam is not focused, we take the beam cross-section to be constant; therefore the sampling volume is described by a sampling depth d. We generalize that the Raman signal is isotropic and therefore randomly polarized, although the incident polarization state will influence what is actually received by the detector as illustrated in Figure 4.3 [Grasselli et al., 1981]. For example, in benzene the $992\,cm^{-1}$ Raman line corresponding to the ring breathing vibrational mode is known to be highly polarized, whereas the $606\,cm^{-1}$ Raman line corresponding to the ring deformation vibrational mode is not polarized [Herzberg, 1966]. However the polarization state of either the incident or signal light is not consequential to our estimation of the sampling depth. To determine the effective path length EPL

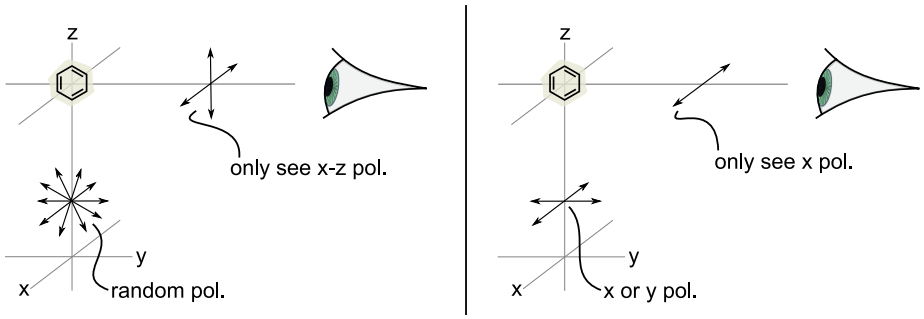

Figure 4.3: Detector polarization state for randomly polarized (left) and horizontally polarized (right) incident light.

consider the beam path lengths Δx and Δy defined by the distance d from the window and the orientation angle θ of the sample holder as depicted in Figure 4.2. Along these beam paths the excitation and signal light will experience an exponential attenuation defined by A_{in} and A_{out} respectively. The effective path length EPL then is determined by integrating the joint attenuation along the path perpendicular to the window from 0 to some distance d representing the total depth penetrated. This development is identical to the determination of the path length realized by a laser beam experiencing atmospheric attenuation due to different absorption and scattering agents [Measures, 1984]. Under these assumptions we have then,

$$\begin{aligned}
&\Delta x = \frac{p}{\sin\theta},\ \Delta y = \frac{p}{\cos\theta},\ \text{and } A_{in} = exp(\Delta x \alpha_{in}),\ A_{out} = exp(\Delta y \alpha_{out}),\ \text{giving} \\
&\int_0^d dp\, A_{in}\, A_{out} = \int_0^d dp\, exp\Big(\frac{-p\,\alpha_{in}}{\cos\theta} + \frac{-p\,\alpha_{out}}{\sin\theta}\Big),\ \text{yielding,} \\
&EPL = \frac{-\cos\theta\sin\theta}{\alpha_{in}\sin\theta + \alpha_{out}\cos\theta}\, exp\Big(-p\frac{\alpha_{in}\sin\theta + \alpha_{out}\cos\theta}{\cos\theta\sin\theta}\Big)\Big|_0^d.
\end{aligned} \tag{4.3.2}$$

The attenuation parameters $\alpha_{()}$ are determined from the available absorption cross-section data $\sigma(\omega)$ and concentration (or number density) N such that $\alpha_{()} = \sigma(\omega)\, N$ and are expressed in units of cm^{-1}. The upper bound on the effective penetration depth is the most useful parameter explaining the sampling volume and the upper boundary, EPL_d, is found by taking the limit of EPL in Equation (4.3.2) as d becomes large. As anticipated, at this limit the attenuation results no signal escaping the bulk sample. This length characterizes the sampling volume and Table 4.1 lists some calculated EPL_d values for various concentrations at different excitations wavelengths. The bulk of the attenuation is experienced by the excitation beam while on resonance. During the tuning of the excitation frequency however, the signal may experience the bulk of the attenuation. These variations are highly dependent on the absorption profile, however outside of the sample, these variations cannot be distinguished, no matter their origin.

Table 4.1: Calculated effective path length, EPL_d, for liquid benzene and liquid toluene for resonant (R) and non-resonant (NR) excitation.

	Sample Material	Excitation λ $[nm]$	Raman λ $[nm]$ †	EPL_d $[\mu m]$
Benzene	pure:	258.88 (R)	265.72	0.77
	0.25 M:	258.88 (R)	265.72	34.4
	pure:	430 (NR)	449.22	184.3
	0.25 M:	430 (NR)	449.22	8190
Toluene	pure:	266.65 (R)	274	1.24
	pure:	430 (NR)	449.40	220.3

†: These calculations are for the Stokes Raman shifts of $992\, cm^{-1}$ for benzene and $1004\, cm^{-1}$ for toluene.

4.4 Discussion of Experimental Uncertainties

The primary sources of error in our work derive from measurement uncertainty involved in power measurement, spectrometer positioning, and fluid measurement. Propagation of these errors to the relevant quantities follow the development given in Bevington [Bevington and Robinson, 1992]. Statistical errors, such as electric noise fluctuations in the CCD array, are not considered as their influence on the measurement are small. Table 4.2 lists the sources of experimental uncertainties. To calibrate the spectrometer a mercury emission line source was utilized. The emission spectra of mercury is well characterized and

Table 4.2: Summary of experimental uncertainties.

Sources of errors	Error
spectrometer resettability (from manuf.) $[nm]$:	± 5.0
spectrometer accuracy (from manuf.) $[nm]$:	± 2.0
wavelength, measurement $[nm]$:	± 0.04
wavenumber, measurement $[cm^{-1}]$:	± 6.4
image resolution $[nm/pixel]$:	0.011
power meter accuracy (from manuf.) [%]:	± 3.0
laser energy stability (from manuf.) [%]:	± 2.0
pipette volume accuracy $[mL]$:	± 0.025

is commonly used for precision calibration. National Institute Standards and Technology (NIST) has documented the uncertainty of the emission line wavelengths for mercury to less than ± 0.001Å[Sansonetti and Reader, 2001]. Our image resolution is determined from the dispersion of the spectrometer onto the CCD element: the linear dispersion is approximately $5.8\,nm$ wide for the SPEX system and the CCD array is 512 pixels wide giving a $5.8/512 = 0.011\,nm$/pixel resolution. The NIST accuracy for the mercury emission lines is well within our image resolution of approximately $0.011\,nm = 0.11$Å. Machine positioning is the most significant source of error. When the spectrometer is positioned onto a wavelength, there is the accuracy of its position and when the position is changed and then returned to this previous wavelength there is the accuracy of the resettability of the spectrometer's position. These arise from rigidity of the mechanical coupling between the grating turret and positioning motor. The manufacturer lists the position and resettability accuracies to be within $\pm 2\,nm$ and $\pm 5\,nm$ respectively. In our trails and frequent calibration iterations, we have observed both of these accuracies to be within $\pm 0.04\,nm$ for the spectral region between $210\,nm$ to $500\,nm$. Mercury emission line images were acquired across the range of $250\,nm$ to $300\,nm$ to determine the accuracy. The mercury lines imaged were the $253.6517\,nm$ and $302.1498\,nm$ both $\pm 0.0001\,nm$ as given in [Sansonetti and Martin, 2005]. For the $253.65\,nm$ mercury line, our data show the peak to be located at $253.52\,nm$ consistently across 12 measurements and the $302.15\,nm$ mercury line peak appears at $302.16\,nm$ consistently on 2 measurements. The appearance of the $253.65\,nm$ line at $253.52\,nm$ may be due to variation in the lamp pressure (differences in degree of pressure broadening). Given the light source's age, the amount and quality of mercury may also contribute to this

discrepancy. However, the data for different calibration trials shows that the line position is consistent for this lamp source. The final spectral data series (after all image processing as detailed previously) will have an wavelength uncertainty of $\pm 0.04\,nm$. This will appear on the images differently however due to the relationship between the wavelength and energy. Our spectra are expressed in terms of the vibrational energy shift from the excitation laser line. The position uncertainty then is expressed in wavenumber shift (cm^{-1}): it is larger at shorter wavelengths. This uncertainty ranges from $\sim 6.4\,cm^{-1}$ at $225\,nm$ to $\sim 2.1\,cm^{-1}$ at $450\,nm$, although expressed in wavelength it is constant across this range.

The excitation laser power was measured using an Ophir Nova power meter fitted with the 3A low power thermal head detector. The power measurement was taken as the average power over 30 seconds with an expected accuracy of $\pm 3\%$ for the 3A detector head.[3] A measurement was repeated after the data image was acquired to detect any power drift and a new measurement was taken after the excitation wavelength was changed. Additionally the Nd:YAG laser (Spectra-Physics Quanta Ray INDI-50-10) has a listed energy stability of $\pm 2\%$. Fortunately the power measurement captures the variance of the laser energy, so the uncertainty in the power measurement is that of the power meter, $\pm 3\%$. This uncertainty will be observed on the data image as a change in the pixel intensity and applies uniformly to all pixels within an image. As with the position, the final spectral data series (after all image processing as detailed previously) with have an intensity uncertainty of $\pm 3\%$.

The last source of uncertainty in the measurements arises from the accuracy of the pipette used in the diluted species trials. The pipette has listed an uncertainty of $\pm 0.025\,mL$. This uncertainty is observed in the molar concentration value of the prepared benzene-heptane solutions. The concentration variation results in the variations in the effective path length due to its dependence on the number density. To determine the uncertainty in the concentration, absorption coefficient, and effective path length, standard error propagation expressions were derived for these uncertainties and are listed in Equations (4.4.1), (4.4.2), and (4.4.3) respectively. These were derived using the total derivative of the functional forms of C, α, and EPL_d. All are expressed in terms of the uncertainty of the pipette

[3]The Ophir Nova instrument offers the feature to take average measurements on different time intervals displaying the result after the period of the time interval. For example, in our trials, we obtained new power measurements every 30 seconds for the average power over the previous 30 seconds.

measurement, $\Delta V = 0.025\,mL$ and evaluated serially starting with Equation (4.4.1). The pipette was used to measure all fluid volumes, so for different concentrations the number of times the pipette was used introduces the same number of uncertainty contributions. This is to say, for example, if the pipette was used 5 times then the total uncertainty in the volume is $5\Delta V$. The absorption coefficient α in Equation (4.4.2) describes both the attenuation of the excitation and signal, recalling that the cross-section $\sigma = \sigma(\omega)$. We have then,

$$C \pm \Delta C = \frac{\rho}{MW}\frac{V_s}{V_s + V_{ss}} \pm \frac{\rho}{MW}\frac{\Delta V}{V_s + V_{ss}} \tag{4.4.1}$$

$$\alpha \pm \Delta\alpha = \frac{\sigma\, N_A\, C}{1000} \pm \frac{\sigma\, N_A\, \Delta C}{1000} \tag{4.4.2}$$

$$EPL_d \pm \Delta EPL_d = \frac{\cos\theta \sin\theta}{\alpha_{in}\sin\theta + \alpha_{out}\cos\theta} \pm \frac{\Delta\alpha_{in}\sin^2\theta\cos\theta + \Delta\alpha_{out}\cos^2\theta\sin\theta}{(\alpha_{in}\sin\theta + \alpha_{out}\cos\theta)^2} \tag{4.4.3}$$

where C is the concentration in $mol\,L^{-1}$, ρ is the solute density in $g\,mL^{-1}$, MW is the solute molecular weight in $g\,mol^{-1}$, V_s is the solute volume in mL, V_{ss} is the solvent volume in mL, α is the absorption coefficient in cm^{-1}, σ is the absorption cross-section in $cm^2/molecule$, N_A is Avogadro's number, and EPL_d is the effective path length in cm. While the variation in the absorption cross-section will lead to different values for $\Delta\alpha_{()}$ and ΔEPL_d, these uncertainties can be expressed as relative uncertainties which are immune to the variations. As may be expected, the relative uncertainty for all the parameters is identical for a given concentration. Table 4.3 lists the calculated absolute and relative uncertainty values for the parameters dependent on the volume uncertainty.

4.5 Peak Classification

Classification of the experimental Raman spectra is two-fold. The data series resulting from the image processing discussed in Section 4.2 yields a standard spectra, showing features across a wavelength or energy shift range. Figure 4.1 shows this result in the single line plot of the Stokes Raman intensity of the $1332\,cm^{-1}$ feature in diamond. This representation shows spectra features for comparison across magnitude, bandwidth, and position (energy shift). The intensity values will have an uncertainty of $\pm 3\%$ across the data series due to the power measurement uncertainy. The positions, in terms of wavenumber shift, will have an uncertainty that varies from $\pm 2.1\,cm^{-1}$ to $\pm 6.4\,cm^{-1}$ depending on the wavelength

Table 4.3: Concentrations, absorption coefficients, and effective path lengths with calculated uncertainties for different liquid benzene in heptane solutions.

Parameter		Case A	Case B	Case C	Units
Concentration	Abs.	0.25 ± 0.003	1.13 ± 0.014	4.98 ± 0.062	$mol\,L^{-1}$
	Rel.	1.11	1.25	1.24	%
$\alpha_{in}(\lambda_{exc} = 258.88\,nm)$	Abs.	182.9 ± 2.03	812.8 ± 10.2	3617 ± 45	cm^{-1}
	Rel.	1.11	1.25	1.24	%
$\alpha_{out}(\lambda_{exc} = 266.72\,nm)$†	Abs.	4.97 ± 0.055	22.1 ± 0.28	98.27 ± 1.21	cm^{-1}
	Rel.	1.11	1.25	1.24	%
$\alpha_{in}(\lambda_{exc} = 430\,nm)$	Abs.	0.43 ± 0.005	1.90 ± 0.024	8.44 ± 0.104	cm^{-1}
	Rel.	1.11	1.25	1.24	%
$\alpha_{out}(\lambda_{exc} = 449.22\,nm)$†	Abs.	0.43 ± 0.005	1.90 ± 0.024	8.44 ± 0.104	cm^{-1}
	Rel.	1.11	1.25	1.24	%
EPL_d for $\lambda_{exc} = 258.88\,nm$	Abs.	34.4 ± 0.38	7.73 ± 0.097	1.74 ± 0.021	μm
	Rel.	1.11	1.25	1.24	%
EPL_d for $\lambda_{exc} = 430\,nm$	Abs.	8190 ± 91	1843 ± 23	414.1 ± 5.12	μm
	Rel.	1.11	1.25	1.24	%

†Calculated for $992\,cm^{-1}$ Stokes shifted wavelength.

range of the image.

The second classification method considers the area underneath a specific spectral feature: the integrated intensity. In this method, we can capture information about the intensity and bandwidth without relying on assumptions about the distribution responsible for the lineshape. The motivation for this approach is due to the lack of prior information that would allow us to properly deconvolve the laser bandwidth and instrument slit function from the spectra. Even including this information, deconvolution has the potential to introduce spectral features when the assumptions on laser lineshape and slit function are inaccurate [Smith and Dent, 2005]. The most straightforward approach to classify features when missing these information is to utilize the integrated intensity [George and Willis, 1990]. For this we utilize the area defined by full-width at half-maximum of the specific spectral feature. For the spectra data series $I(1, i)$ over wavenumber shift i the integrated

intensity A_{peak} then follows as,

$$A_{peak} = \sum_{k_- \text{ to } k_+}^{\Delta w} I_k \text{ where,}$$
$$I_m = \max(I(1,i)) = I_i(k_m),\ \Delta w = |k_+ - k_-|, \tag{4.5.1}$$
$$k_+ \equiv k_i \text{ where } I_i = \tfrac{1}{2} I_m(k_i > k_m), \text{ and } k_- \equiv k_i \text{ where } I_i = \tfrac{1}{2} I_m(k_i < k_m).$$

Figure 4.4 illustrates the integration calculation for two different regimes on a set of artificial data, with the shaded region representing the calculated area. These artificial data were generated using a simple pseudo-Voigt profiles superimposed with white noise as defined in [Wojdyr, 2007]. For spectral features observed in the resonance regime the features exhibit a significantly larger width than those in the non-resonant regime. This is due to the increased transition lifetime inherent in resonance Raman. However, there is a contribution to this width introduced by the variations in the excitation light bandwidth contributed by the OPO process. This contribution is fairly linear within our excitation wavelength range starting with $\sim 5\,cm^{-1}$ at $200\,nm$ up to $\sim 35\,cm^{-1}$ at $300\,nm$ as shown in Figure 4.5 [U-O, 1999]. To bolster using the integrated intensity instead of peak height to classify

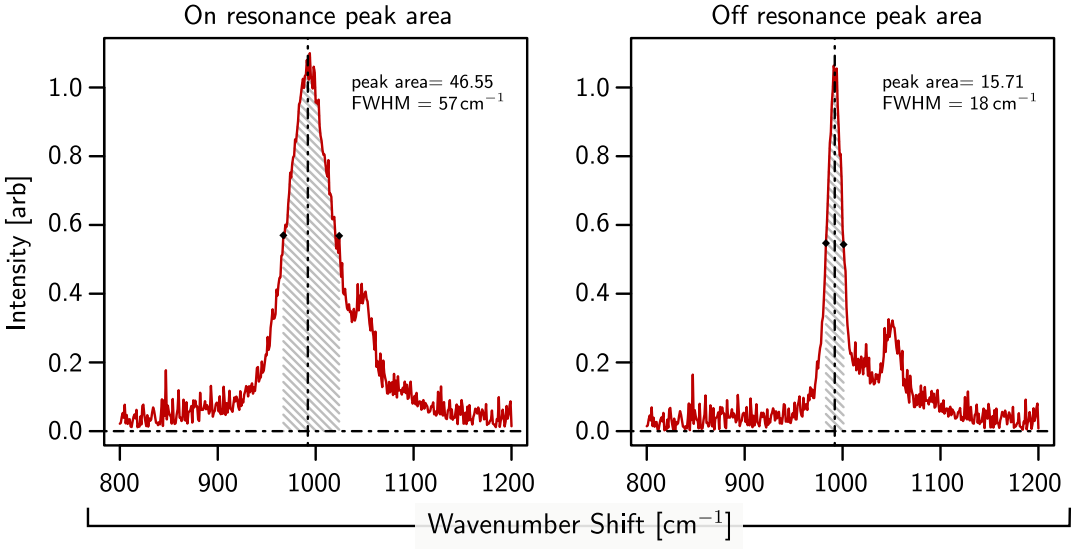

Figure 4.4: Illustration of spectral peak area (shaded region) calculation for resonant and non-resonant artificial data series.

the spectral features consider Figure 4.6. On the left, both the area and peak height of the

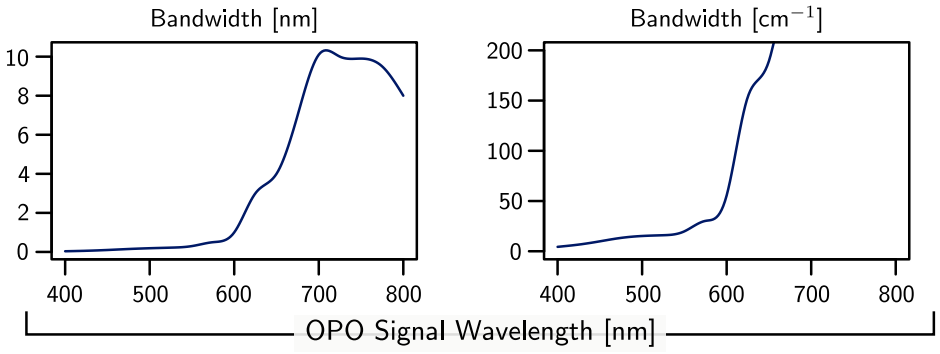

Figure 4.5: Bandwidth of the NCSU OPO system in wavelength (left) and wavenumber (right) as indicated by the manufacturer.

total intensity are established. Whereas on the right, increasing both the OPO bandwidth and instrument contributions, the total intensity value is shifted more significantly than the area. This suggests that the area, being less susceptible to fluctuations in intensity, will more accurately describe a spectral feature than the peak intensity in the absence of corrective deconvolution. The uncertainty in the integrated intensity values arises from the variations

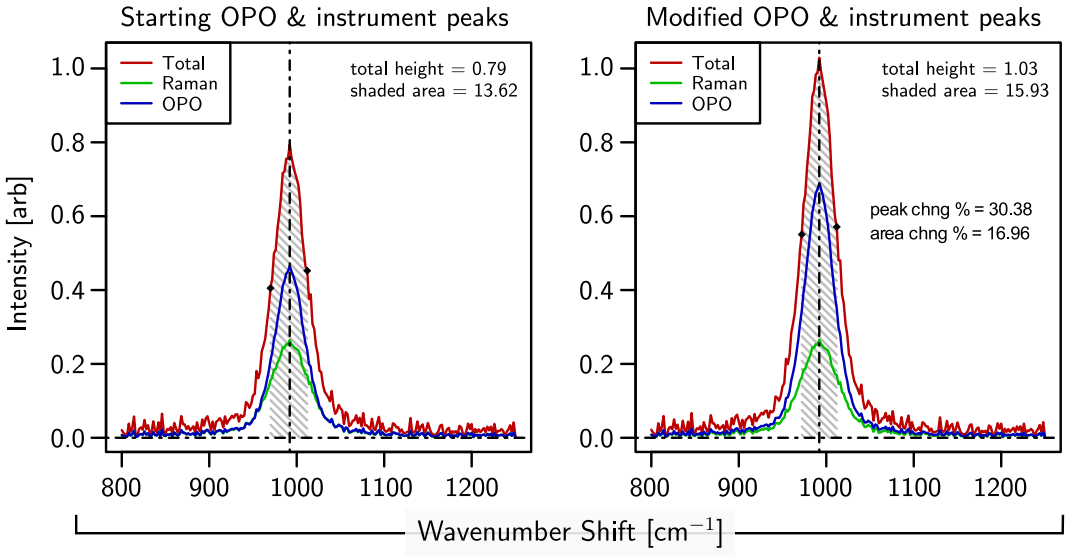

Figure 4.6: Illustration of different classification schemes for spectral features without instrument slit function and excitation laser lineshape information.

in power measurement as with the intensity value. Due to the way the area is calculated

(Equation (4.5.1)), the uncertainty in the integrated intensity is expressed as the uncertainty in the intensity for a specific center position with a position uncertainty dependent on the wavelength range of the feature. For example, should the integrated intensity of the ring breathing vibrational mode of benzene have a value $A_{peak} = 10$ positioned at $992\,cm^{-1}$ then the uncertainty in are would be expressed as $\pm 3\%$ at $992 \pm 5.4\,cm^{-1}$ for an excitation wavelength of $259\,nm$.

Chapter 5

Overview of Key Experimental Spectra

5.1 Overview

Utilizing a continuously tunable light source allows the experimentalist to select specific absorption features previously inaccessible with fixed line laser sources. The scanning of the excitation frequency may yield new spectrographic information as the system transitions into and out of the excited state. Experimental studies of these types of transitions are absent in previous work on resonance Raman spectroscopy. We have observed that sharp absorption features may yield similarly sharp resonance Raman profiles in both liquid benzene and liquid toluene. This suggests that in order to probe narrow absorption features using a tunable excitation light source, one needs high resolution absorption spectra. High resolution absorption spectra allows precision tuning of the excitation frequency so specific absorption features may be probed and the maximal enhancement can be realized. In our initial trials investigating the $260\,nm$ absorption system of liquid benzene we observed that sharp absorption features may be entirely missed when tuning the excitation frequency if the resolution of the tuning steps is too large. The absorption feature for benzene in this case has a width less than $1\,nm$. Also, because of the presence of the high absorption required to realize resonance enhancement, the Raman signal may be unobservable (very weak) nearby an absorption feature. This signal absorption may swamp the preresonance enhancement that indicates the proximity of the absorption peak.

The ultraviolet absorption spectra and Stokes Raman spectra of the primary sample species we have investigated are provided below. Our studies cover three main sample species: rough stone diamond in Figures 5.1 and 5.2, liquid benzene in Figures 5.4 to 5.7, liquid toluene in Figures 5.8 to 5.11, and liquid benzene-heptane solution in Figure 5.12. Additionally, the resonance Raman vibrational mode assignments for liquid benzene and liquid toluene, both in the first excited electronic state, are proposed. Each sample species is briefly discussed and the experimental configuration and parameters are indicated. The Raman spectra presented are the product of the image data processing outlined in Chapter 4 and were obtained using our experimental apparatus as illustrated in Figure 3.1 of Chapter 3 whereas the absorption spectra were obtained from the literature. Measurement uncertainty in the spectra are discussed in Chapter 4. For all Raman spectra shown, the intensity uncertainty is within $\pm 3\%$ and the wavenmuber shift uncertainty is expected to be within $\pm 6.4\, cm^{-1}$. Uncertainty for the integrated intensity data are indicated individually.

5.2 Diamond Raman Spectra

Diamond provides a very suitable and reliable sample for Raman scattering due to its strongly intense Stokes Raman line at $\sim 1332\, cm^{-1}$ and has been a subject of Raman studies since the early work done by Raman [Raman, 1956]. Resonance Raman scattering studies on diamond have been confined to excitation wavelengths accessible using argon laser light sources [Calleja et al., 1978; Grimsditch et al., 1981]. Additionally, Calleja et al. have observed resonance enhancement in the second-order (but not the first-order) Raman scattering for diamond as the excitation wavelength approaches the fundamental band gap for diamond [Calleja et al., 1978]. In our work, we extend this excitation range from $215\, nm$ to $300\, nm$ with $1\, nm$ tuning step size from $215\, nm$ to $235\, nm$ in the approach to the band gap at approximately $210\, nm$. Diamond species are typically classified into four types; Ia, Ib, IIa, and IIb. Depending on the type, the position of its primary ultraviolet absorption band can vary significantly with the tail starting at $\sim 300\, nm$ for Type I and $\sim 220\, nm$ for Type II [Edwards and Philipp, 1985]. For our experimental sample we have utilized a rough diamond stone of Type Ia provided by Dr. Diane S. Knight [Knight and White, 1989]. Natural diamond samples usually contain impurities such as nitrogen and non-diamond carbon (e. g. graphite) which can modify the position of the absorption band

and may also exhibit additional Raman features arising from these non-diamond molecular bonds [Kaiser and Bond, 1959; Leeds et al., 1998]. Figure 5.1 shows our diamond Stokes Raman spectra for three excitation wavelengths showing the primary Stokes shifted Raman line at $1332\,cm^{-1}$ from the excitation frequency. Image acquisition time was 60 seconds with the spectrometer slit widths of $1.0\,mm$, $2.0\,mm$, and $100\,\mu m$ for the input, filter, and main slits respectively. We also attempted to obtain second-order Stokes Raman spectra ($2664\,cm^{-1}$) for our sample, however the images revealed no discernible intensity over the noise background.

Figure 5.2 shows the integrated intensity of the $1332\,cm^{-1}$ Stokes Raman line over our excitation range from $215\,nm$ to 235 in $1\,nm$ steps and larger steps up to $300\,nm$. These integrated intensity values have an uncertainty of $\pm 3\%$ and wavelength uncertainty of $\pm 0.05\,nm$. For reference, the scaled ($10\times$) absorption coefficient is also shown. This is calculated from the room temperature extinction coefficient data for Type Ia provided by Edwars and Philipp [Edwards and Philipp, 1985].[1] Our interpretation of the irregular behavior of the integrated intensitis in Figure 5.2 is that the variance is due to surface/bulk contaminates inherent in natural diamond and possible indirect band transitions. Surface contaminates may attenuate the excitation/signal light. Also bulk contaminates may exhibit some Raman intensity. Graphite has Raman features in the Stokes shifted range from $\sim 1300\,cm^{-1}$ to $\sim 1450\,cm^{-1}$ [Leeds et al., 1998]. Due to the slight variations of our beam positioning after tuning the OPO wavelength, excitation light may favor scattering for regions of graphite and other non-diamond carbon bonds differently from the previous excitation wavelength thereby resulting in more or less image intensity. Figure 5.3 shows a $50\times$ magnification of our diamond sample where bulk contaminates are clearly visible. Finally, while the direct transition band gap is $\sim 5.5\,eV$ (labled A in Figure 5.2), there may be some nearby indirect transitions that lead to excitation photon absorption which may contribute to or attenuate the Raman intensity. While clean diamond is not known to have nearby indirect transitions based on the calculated crystal potentials, the presence of contaminate materials may allow some indirect transitions [Salehpour and Satpathy, 1990]. However the extent of these allowances may be difficult if not impossible to determine

[1] The absorption coefficient is calculated from the complex index of refraction data (κ) by $\alpha = \frac{2\omega}{c}\kappa = \frac{4\pi}{\lambda}\kappa$, where the complex index of refraction is $\tilde{n} = n + \imath\kappa$ and λ is the wavelength in nm. The units for the absorption coefficient are cm^{-1}.

without knowledge of the composition of the contaminates.

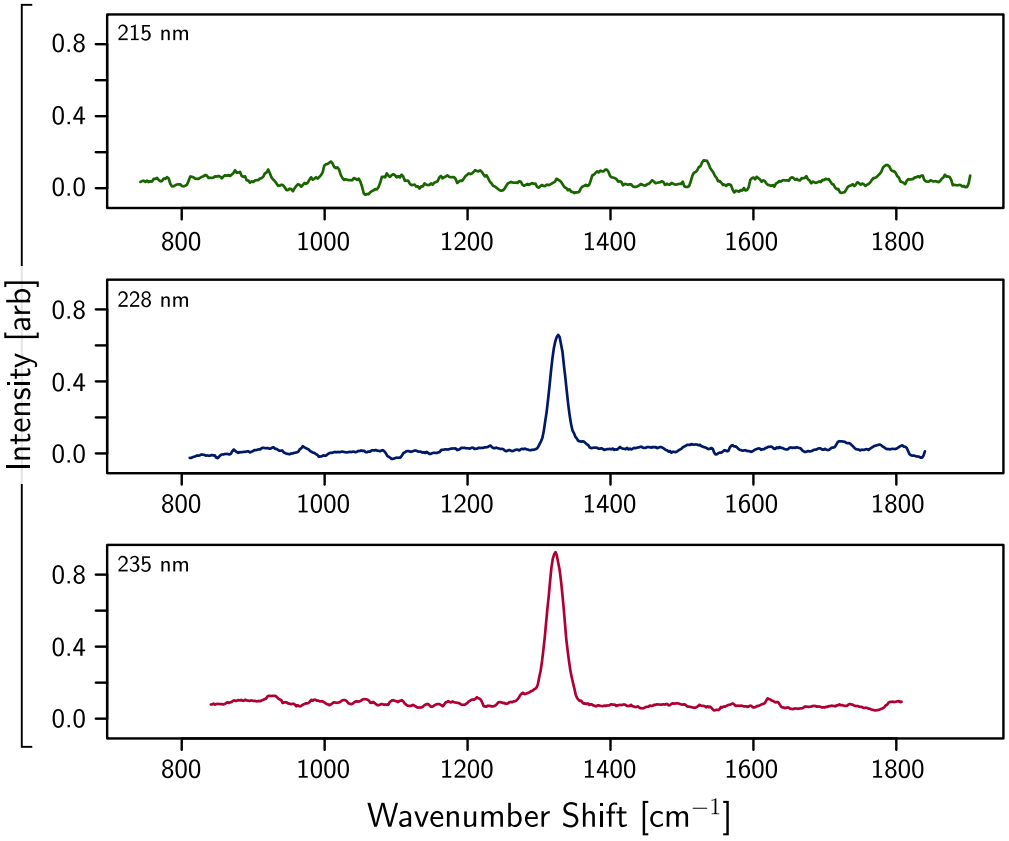

Figure 5.1: Diamond Stokes Raman spectra for three excitation wavelengths.

5.3 Benzene Absorption and Raman Spectra

The most interesting results arrive from our investigation of liquid benzene. The volume of literature on benzene is large and the molecule is perhaps on of the most studied systems after the water molecule. Also Raman and Krishnan utilized benzene as a sample species in their famous work in the mid-1920s [Raman and Krishnan, 1928]. The molecule is an planar hexagonal ring of six carbon atoms with a hydrogen atom attached to each carbon atom extending radially from the center of the molecule. It is aromatic, having delocalized electrons, and has no net dipole. Much debate has taken place as to the correct picture of the structure of benzene, with the presently accepted model attributable to Kekulé. Our

samples were obtained from a lot of 99% pure benzene (CAS# 71-43-2) purchased from Alfa Aesar (item# L14012). For the sample preparation the vessel was throughly washed with ethanol then rinsed with spectroscopic grade methanol followed by a rinse with benzene before filling to full sample volume. Sample volume was usually between $10\,mL$ and $15\,mL$ with the vessel tighly capped. The local experimental area was ventilated to remove accumulated benzene vapors. The signal acquisition time was 120 seconds with slit widths of $4.0\,mm$, $2.0\,mm$, and $250\,\mu m$ for the input, filter, and main slits respectively.

We choose liquid benzene for two primary reasons: availability of absorption features within our OPO tuning range and its well characterized Raman features. Benzene has several absorption systems within our tuning ability from approximately $235\,nm$ to $270\,nm$. Our main data and analysis involve the $260\,nm$ absorption system which represents the transition from the ${}^1A_{1g}$ ground state to the ${}^1B_{2u}$ first excited state [Callomon et al., 1966]. Figure 5.4 shows three absorption cross-section spectra for benzene from $230\,nm$ to $280\,nm$ (vertical lines identify the local maximum wavelength of the $260\,nm$ absorption system). The Inagaki series is for pure liquid benzene with a $2.94\,\mu m$ layer thickness at room temperature, wavelength uncertainty of $\pm 0.49\,nm$, and cross-section uncertainty of $\pm 5\%$ [Inagaki, 1972]. The API series is for $5.4\,mM$ solution of liquid benzene in iso-octane with a cell thick-

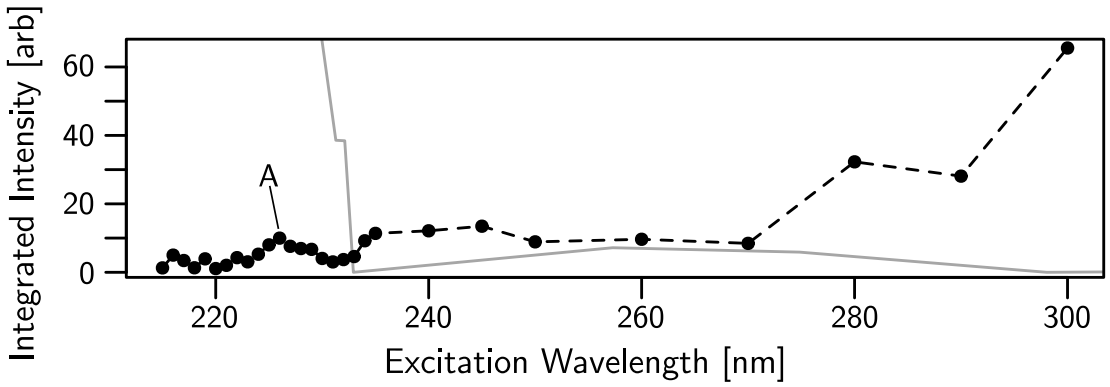

Figure 5.2: Integrated intensity of the Stokes Raman band at $1332\,cm^{-1}$ for diamond for various excitation wavelengths. Solid line: absorption coefficient (scaled $10\times$), from [Edwards and Philipp, 1985]. The A indicates the band gap edge at $\sim 5.5\,eV$.

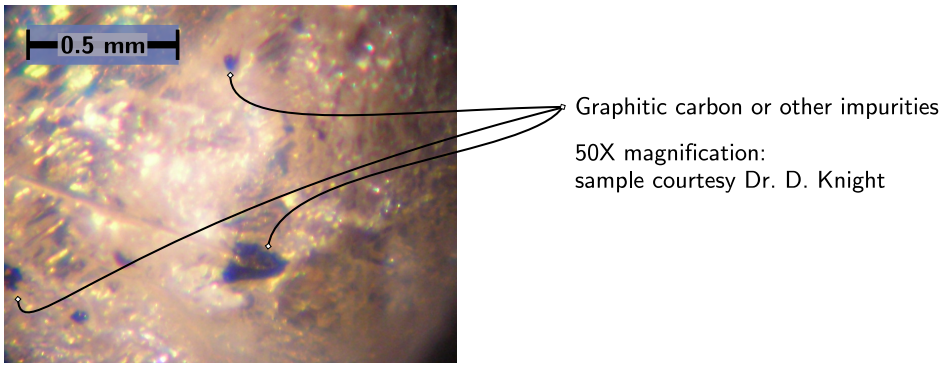

Figure 5.3: Photograph of diamond specimen, under magnification, showing internal contamination.

ness of $1.002\,cm$ at room temperature, wavelength uncertainty of $\pm 1.6\,nm$, and no reported cross-section uncertainty [API, 1970]. The presence of iso-octane introduces the shift seen in the API absorption spectra when compared to the Inagaki pure data. Finally the Etzkorn series is for vapor-phase benzene with a cell thickness of $6.22\,m$ at room temperature, wavelength uncertainty of $\pm 0.146\,nm$, and cross-section uncertainty of $\pm 0.21 \cdot 10^{-18}\,cm^2$ [Etzkorn et al., 1999]. Additional absorption spectra were consulted of varying degrees of utility in [Perkampus, 1992; Radle and Beck, 1940; Láng, 1970, 1961]. Figure 5.5 provides a closer detail of the $260\,nm$ absorption system where much of our data and analysis centers and indicates the wavelength positions of the absorption maxima. The choice of this spectral region is due to difficulty we encountered in obtaining signal over the background noise in the neighboring regions. The progression of spectral peaks are spaced such that the main Stokes Raman spectral feature at $\sim 992\,cm^{-1}$ overlaps onto the longer wavelength peak systems (e. g. $260\,nm$ absorption swamps the features active from $253\,nm$ excitation). For our trials, the Etzkorn series was utilized both for the absorption correction of the Raman spectra and the precision tuning of the excitation wavelength about absorption features due to its high resolution ($\Delta\lambda = 0.039\,nm$).

The main focus of our data analysis in benzene surrounds the $\sim \pm 2.3\,nm$ window about the ring-breathing vibrational mode on the Stokes side at $992\,cm^{-1}$. The ring-breathing (ν_2) mode is the second most intense mode in the benzene Raman spectra and is the planar stretching of the carbon-carbon bonds in the ring [Dollish et al., 1974; Herzberg, 1960]. Figure 5.6 shows some typical spectra for the region around the ring-breathing mode

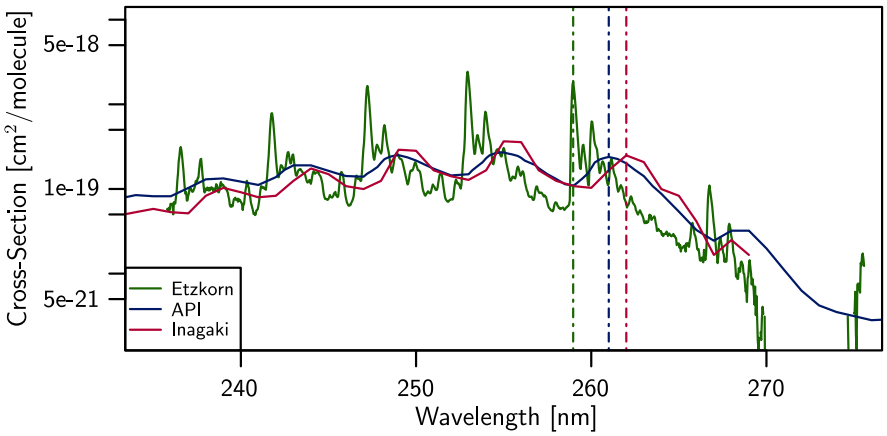

Figure 5.4: Eztkorn, Inagaki, and API ultraviolet absorption spectra for benzene.

(vertical dashed line) for various excitation wavelengths ranging from resonant excitation (top panel), to off-resonance ultraviolet excitation at 266.75 nm (middle panel), to non-resonant visible excitation at 430 nm (bottom panel). The image widths for all of these spectra are within $\pm 0.1\,nm$ of each other, however the energy range becomes smaller as wavelength increases resulting in different wavenumber shift scales. These spectra have been corrected for self-absorption. The off-resonance spectra at 266.75 nm excitation shows the masking effect of spectrometer filter stage slit visible as the sharp drop to zero on the

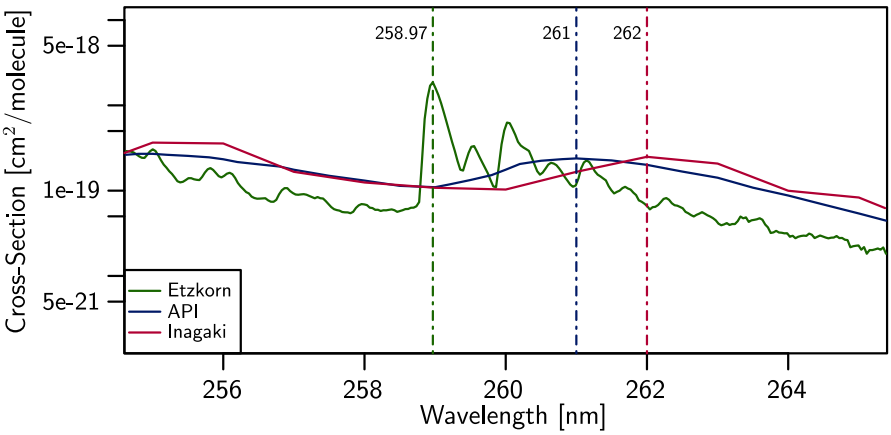

Figure 5.5: Absorption region of interest from Figure 5.4.

right and left extremes of the spectra. This clamping of the spectra is especially noticeable on the corrected spectra data due to the scaling introduced by the correction. Figure 5.7

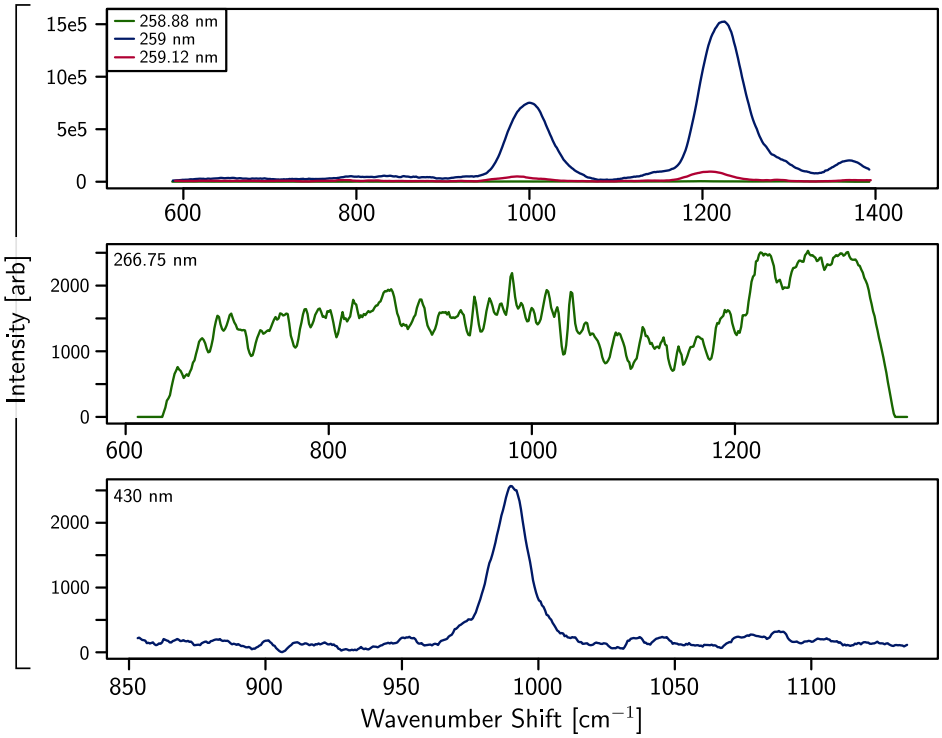

Figure 5.6: Stokes Raman spectra for liquid benzene for near resonance and off resonance wavelength excitations.

shows the our most comprehensive Stokes Raman spectra for two excitation wavelengths. The top panel shows the spectra for resonant excitation at 259 nm. The data series is constructed from 9 image files with the image center positions spanning 263.85 nm to 293.84 nm. The bottom panel shows the spectra for non-resonant excitation at 430 nm. The data series is constructed from 13 image files with the image center positions spanning 449.22 nm to 497.22 nm. Common features in each of the spectra are indicated by the boxed letters above the top panel (vertical dashed lines) and the additional letters annotate the features unique to the resonant excitation spectra. The vibrational mode assignment for these spectra are presented in Table 5.1 and are based on the aggregated work done by Herzberg [Herzberg, 1960] and a thorough documentation by Bertie and Keefe [Bertie and Keefe, 2004]. Additional ground state vibrational assignment and discussion for benzene can be found in

[Angus et al., 1936; Keefe and Bertie, 2006; Wilson, 1934a]. Due to the symmetry of the benzene molecule, the total number of fundamental vibrational modes for the molecule is $3N - 6 = 36 - 6 = 30$, where N is the number of atoms in the molecule [Wilson, 1934b]. Of these 30 fundamental modes, certain transitions will allow these fundamental modes to have Raman active vibration, infrared active vibration, both, or neither. There is also significant overtone and combination mode vibrational frequencies observed in the vibrational spectra [Herzberg, 1960].

While the assignments for non-resonant excitation Raman modes are well documented, the assignment for resonant excitation Raman modes is sparse. The first reported resonance Raman spectra for benzene is attributable to Ziegler and Hudson [Ziegler and Hudson, 1981] utilizing deep ultraviolet excitation at 212.8 nm. Ziegler and Hudson report significant overtone and combination modes for the 212.8 nm excitation compared to off resonance excitation at 354.7 nm. It should be noted that our resonance excitation wavelength probes the lower energy $^1A_{1g} \rightarrow {}^1B_{2u}$ transition, whereas the Ziegler and Hudson work considers the higher energy $^1A_{1g} \rightarrow {}^1B_{1u}$ transition. Also the absorption profile of benzene near the 210 nm absorption system ($^1B_{1u}$) is significantly different than the 260 nm system we have explored. A study by Gerrity et al. [Gerrity et al., 1985] extends the Ziegler and Hudson work deeper into the 210 nm system from 184 nm to 220 nm. This study represents a closer analogue to our work as they use several excitation wavelengths (218 nm, 213 nm, 204 nm, 200 nm, and 184 nm). Again this study is an investigation of the higher energy 210 absorption system. These works, while exhibiting similar spectral features to our 259 nm resonant excitation, should not be expected to show similar vibrational assignments due to the difference in the excited state active. The listing in Table 5.1 for the resonant 259 nm excitation are what we believe may be potential candidates for the vibrational assignment of this first excited state. The comprehensive spectra presented here will hopefully motivate a theoretical exploration of this excited state and should provide a useful experimental confirmation of these assignments.

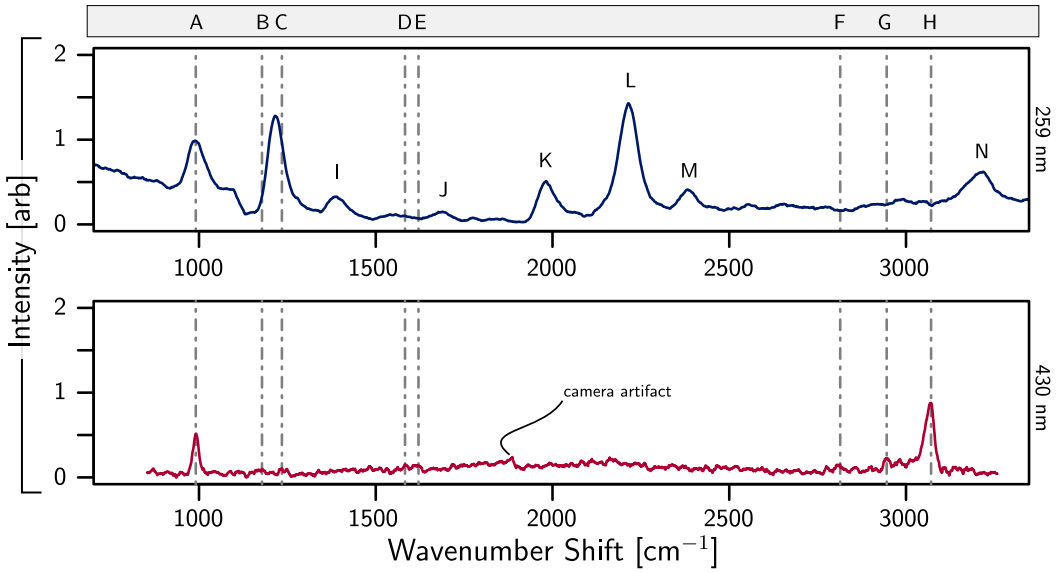

Figure 5.7: Full Stokes Raman spectra for pure benzene with 430 nm and 259 nm excitation wavelengths.

Table 5.1: Vibrational assignments for the experimental Raman spectra of liquid benzene, in Herzberg notation.

	This Work		From [Herzberg, 1960]			From [Bertie and Keefe, 2004]		
430 nm	Center	Intensity	Assignments	Center	%Diff	Assignments	Center	%Diff
A	990.87	1.02827	ν_2	991.6	0.074	ν_2	992.5	0.164
B	1178.2	0.200959	ν_{17}	1178	-0.017	ν_{17}	1176.8	-0.119
C	1234.5	0.213243	—	—	—	—	1225.0	-0.776
D	1582.8	0.30008	ν_{16}	1584.8	0.126	ν_{16}	1586.2	0.214
E	1620.9	0.274122	$(\nu_2 + \nu_{18})$	1606.4	-0.903	$\nu_6 + \nu_{18}$	1617.8	-0.192
F	2813.9	0.29768	—	—	—	$\nu_3 + \nu 13$	2818.9	0.177
G	2945.4	0.446001	—	—	—	—	2950.0	0.156
H	3070.9	1.75975	ν_1	3069	-0.062	ν_1	3071.5	0.020
259 nm	Center	Intensity	Assignments †	Center	%Diff	Assignments †	Center	%Diff
A	989.84	0.988966	ν_2	991.6	0.177	ν_2	992.5	0.268
C	1216.4	1.28088	$2\,\nu_{18}$	1211.2	-0.429	$2\,\nu_{18}$	—	—
I	1386.8	0.327701	$\nu_2 + \nu_{20}$	1395.6	0.631	$\nu_7 + \nu_{20}$	1393.3	0.467
J	1688.7	0.151158	$2\,\nu_{11}$	1693	0.254	$2\,\nu_{11}$	1699.6	0.641
K	1981.3	0.510602	$2\,\nu_2$	1983.2	0.096	$\nu_{16} + \nu 20$	1987.7	0.322
L	2214.3	1.4293	$\nu_{18} + (\nu_2 + \nu_{18})$	2212	-0.104	$\nu_{14} + \nu 17$	2210.5	-0.172
M	2381.6	0.411639	$2\,\nu_2 + \nu_{20}$	2387.2	0.235	$\nu_3 + \nu_{14}$	2382.2	0.025
N	3217.5	0.621232	$2\,\nu_2 + 1234.5$	3217.7	0.006	—	3217.0	-0.016

Centers are cm^{-1} and intensities are arbitrary units. †: Possible assignments, based on ground state vibrational energies.

5.4 Toluene Absorption and Raman Spectra

Toluene is a benzene derivative and likewise shares many similarities with benzene in terms of its structure and vibrational spectra. Toluene is a planar hexagonal ring of six carbon atoms with a hydrogen atom attached to each of five of the carbons and a methyl group (CH_3) attached to the remaining carbon with all hydrogen and the methyl group extending radially from the center of the molecule. It is aromatic as with benzene and the attached methyl group gives the molecule a small net dipole of $0.36\,D$ (Debye). Our samples were obtained from a lot of 99.8% pure anhydrous toluene (CAS# 108-88-3) purchased from Sigma Aldrich (item# 244511-2L). For the sample preparation the vessel was throughly washed with ethanol then rinsed with spectroscopic grade methanol followed by a rinse with toluene before filling to full sample volume. Sample volume was usually between $10\,mL$ and $15\,mL$ with the vessel tighly capped. The local experimental area was ventilated to remove accumulated toluene vapors. The signal acquisition time was 120 seconds with slit widths of $4.0\,mm$, $3.0\,mm$, and $250\,\mu m$ for the input, filter, and main slits respectively.

Like benzene, our selection of toluene for resonance Raman study is motivated primarily by the available absorption spectra features in the OPO tuning range. Our investigations of toluene have been localized to the absorption system around $267\,nm$. Figure 5.8 shows two absorption cross-section spectra for toluene from $245\,nm$ to $280\,nm$ (vertical lines identify the local maximum wavelength of the $267\,nm$ absorption system). Figure 5.9 provides a closer look at the $267\,nm$ absorption system. The API series is for $3.6\,mM$ solution of liquid benzene in iso-octane with a cell thickness of $1.002\,cm$ at room temperature, wavelength uncertainty of $\pm 1.6\,nm$, and no reported cross-section uncertainty [API, 1970]. The Etzkorn series is for vapor-phase toluene with a cell thickness of $6.22\,m$ at room temperature, wavelength uncertainty of $\pm 0.146\,nm$, and cross-section uncertainty of $\pm 0.24 \cdot 10^{-18}\,cm^2$ [Etzkorn et al., 1999]. Additional absorption spectra are available as with benzene varying in degrees of utility [Perkampus, 1992; Láng, 1961, 1970]. The choice of this spectral region is motivated by our experiences with benzene. Toluene shares a similarly positioned and intense fundamental vibration for the carbon ring breathing at $\sim 1004\,cm^{-1}$ and is the focus of our tuning exploration. While not as prominent as those in benzene, toluene exhibits similar overlapping absorption features that swamp the Raman signal for the ring breathing vibrational mode so we have restricted our studies to the absorption

system at 267 nm. Also the overall absorption intensity of toluene is approximately five times more intense than benzene. The Etzkorn series was utilized both for the absorption correction of the Raman spectra and the precision tuning of the excitation wavelength about absorption features due to its high resolution ($\Delta\lambda = 0.039\,nm$). Figure 5.10 shows

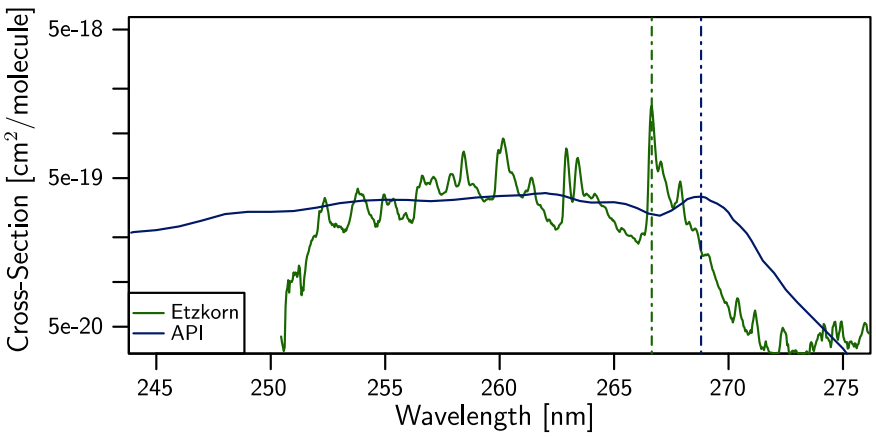

Figure 5.8: Eztkorn and API ultraviolet absorption spectra for toluene.

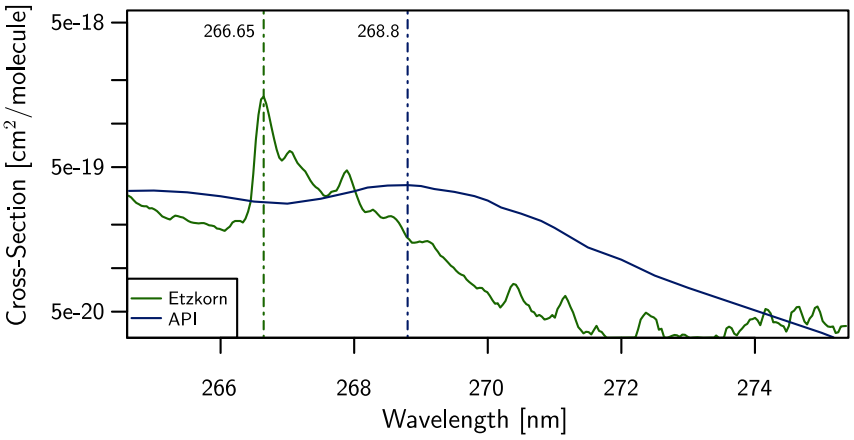

Figure 5.9: Absorption region of interest from Figure 5.8.

some typical spectra for the region around the ring-breathing mode (vertical dashed line) for various excitation wavelengths straddling resonant excitation: 266.14 nm (top panel), at the absorption maximum at 266.64 nm (middle panel), and 276.64 nm (bottom panel).

The main focus of our data analysis in toluene surrounds the $\sim \pm 2.3\,nm$ window about the ring-breathing vibrational mode on the Stokes side at $1004\,cm^{-1}$. The ring-breathing (ν_9) mode is the third most intense we have observed although other studies have shown other modes to be more intense than that of the ring-breathing vibration [Xie and Boggs, 1986; Keefe et al., 2003; Keefe and MacDonald, 2006]. The image widths for all of these spectra are within $\pm 0.1\,nm$ of each other, however the energy range becomes smaller as wavelength increases resulting in different wavenumber shift scales. These spectra have been corrected for self-absorption. Figure 5.11 shows the our most comprehensive Stokes Raman spectra

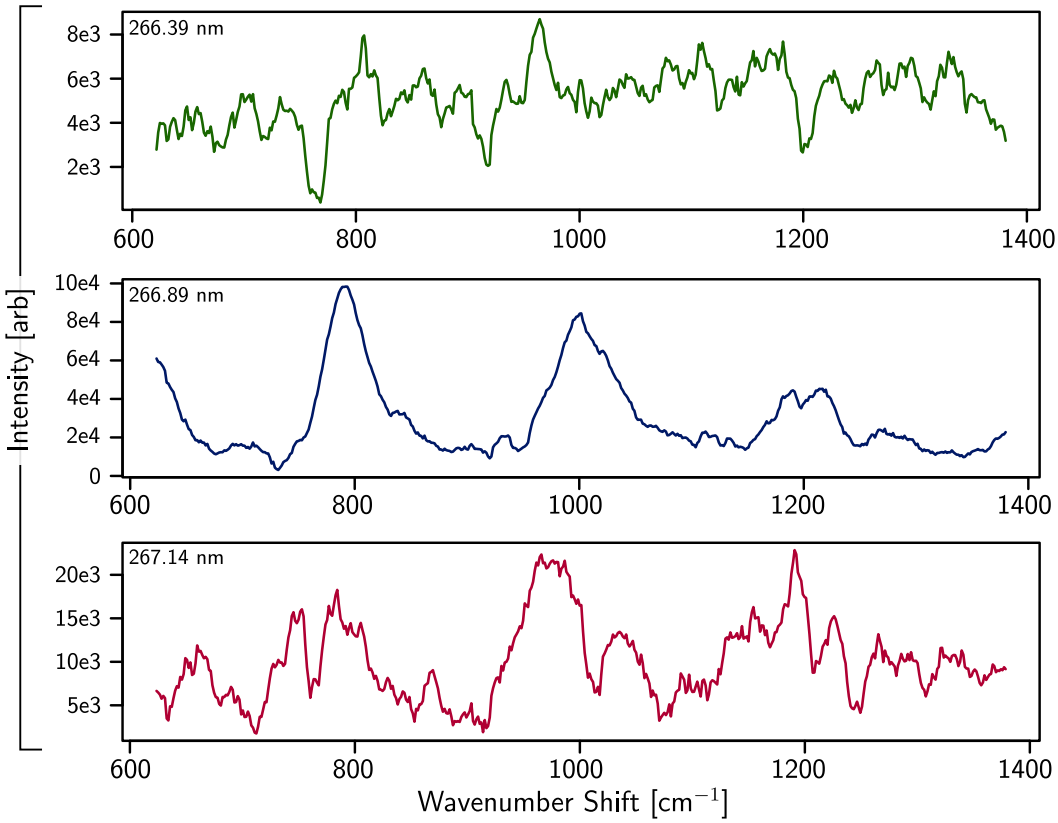

Figure 5.10: Stokes Raman spectra for liquid toluene for near resonance wavelength excitations.

for two excitation wavelengths. The top panel shows the spectra for resonant excitation at $266.83\,nm$. The data series is constructed from 8 image files with the image center positions spanning $272.19\,nm$ to $298.19\,nm$. The bottom panel shows the spectra for non-resonant excitation at $430\,nm$. The data series is constructed from 16 image files with the image

center positions spanning 439 nm to 499 nm. Common features in each of the spectra are indicated by the boxed letters above the top panel (vertical dashed lines) and the additional letters annotate the features unique to the resonant excitation spectra. The vibrational mode assignment for these spectra are presented in Table 5.2 and are based on the work done by Bertie et al. [Bertie et al., 2005]. Due to the symmetry of the toluene molecule, the total number of fundamental vibrational modes for the molecule is $3N - 6 = 45 - 6 = 39$, where N is the number of atoms in the molecule [Xie and Boggs, 1986]. Of these 39 fundamental modes, certain transitions will allow these fundamental modes to have Raman active vibration, infrared active vibration, both, or neither. There is also significant overtone and combination mode vibrational frequencies observed in the vibrational spectra [Bertie et al., 2005]. To our knowledge, studies on this excited state for toluene are sparse and we hope the experimental spectra present will motivate and supplement further theoretical examination.

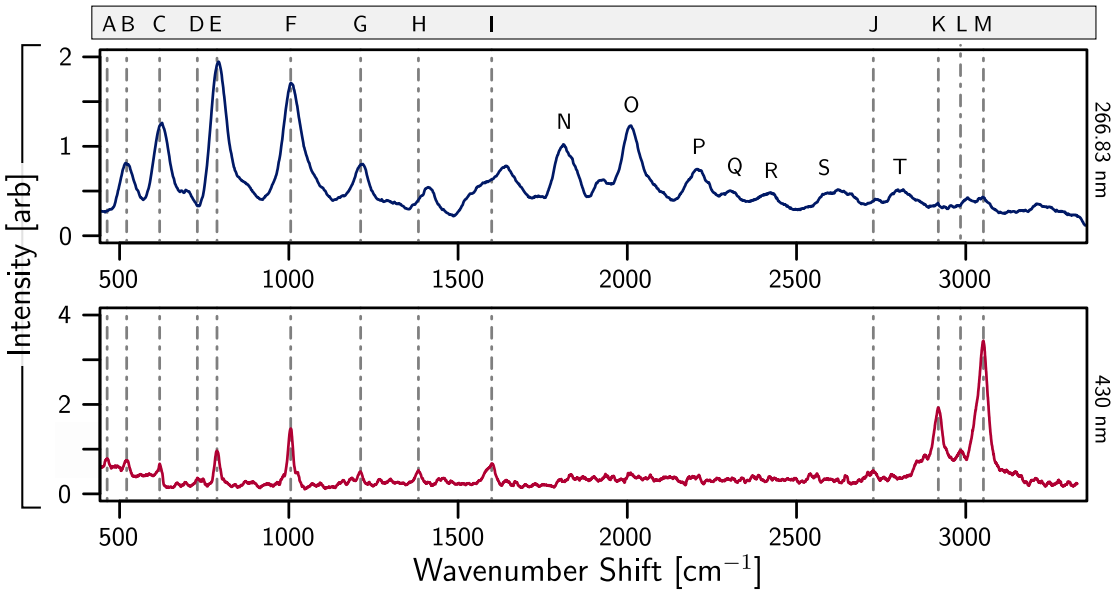

Figure 5.11: Full Stokes Raman spectra for pure toluene with 266.83 nm and 430 nm excitation wavelengths.

Table 5.2: Vibrational assignments for the experimental Raman spectra of liquid toluene, in Herzberg notation.

	This Work		From [Bertie et al., 2005]		
430 nm	Center	Intensity	Assignments	Center	%Diff
A	463.19	0.79467	ν_{19}	464.4	0.261
B	520.87	0.750046	ν_{11}	521	0.025
C	618.26	0.674136	ν_{29}	622	0.601
D	729.71	0.358942	ν_{17}	729.9	0.026
E	787.74	0.966395	ν_{10}	785.6	-0.272
F	1005.5	1.46189	ν_{9}	1002.3	-0.319
G	1212.1	0.500785	ν_{6}	1210.2	-0.157
H	1382.9	0.527995	ν_{32}	1378.9	-0.290
I	1599.3	0.6803	ν_{4}	1604.6	0.330
J	2726.9	0.524987	—	2737	0.369
K	2919	1.93005	ν_{31}	2919.9	0.031
L	2984.1	0.962895	$\nu_4 + \nu_{32}$	2979.1	-0.168
M	3052.2	3.42411	ν_{2}	3055	0.092
266.83 nm	Center	Intensity	Assignments †	Center	%Diff
B	518.09	0.812517	ν_{11}	521	0.559
C	625.73	1.26018	ν_{29}	622	-0.600
E	792.76	1.94672	ν_{10}	785.6	-0.911
F	1005.7	1.70762	ν_{9}	1002.3	-0.339
G	1218.7	0.802317	ν_{6}	1210.2	-0.702
H	1411.3	0.542322	$\nu_{29} + \nu_{10}$	1407.6	-0.263
I	1641.5	0.781517	$\nu_{9} + 633$	1635.3	-0.379
N	1810.8	1.01347	$\nu_{12} + \nu_{13}$	1809.1	-0.094
O	2011.2	1.23171	$\nu_{12} + \nu_{36}$	2008	-0.159
P	2206.2	0.74473	$\nu_7 + \nu_8$ or $\nu_{23} + \nu_{29}$	2209	0.127
Q	2318	0.211491	$2\nu_{27}$	2312	-0.260
R	2422.7	0.482271	$3\,(2\nu_{14})$	2430	0.300
S	2621.3	0.514685	$\nu_7 + \nu_{24}$	2621	-0.011
J	2731.8	0.138118	—	2737	0.190
T	2815	0.515024	$\nu_4 + \nu_6$	2815	0.000
K	2918.1	0.246769	ν_{31}	2919.9	0.062
L	2992.4	0.263396	$3\,\nu_9$	3007	0.486
M	3051.9	0.416385	ν_{2}	3055	0.101

Centers are in cm^{-1} and intensities are in arbitrary units. †: Possible assignments, based on ground state vibrational energies.

5.5 Raman Spectra of Benzene-Heptane Solutions

One of the primary interests in resonance Raman scattering is the enhanced scattering intensity when on or very close to the resonance absorption feature. The potential enhancement is beneficial to small concentration and small sample volume species. These regimes provide an immediate improvement in trace species detection in remotes sensing and signal level enhancement in near-field optical microscopy. A discussion on this utility and analysis of the solution species data is presented in Chapter 7. Presented here are the Raman spectra for four solutions of liquid benzene dissolved in liquid heptane. Table 5.3 lists the solution concentrations and excitation wavelengths. Our benzene solutions were prepared from a lot of 99% pure benzene (CAS# 71-43-2) purchased from Alfa Aesar (item# L14012) and a lot of 99% pure heptane (CAS# 142-82-5) purchased from Sigma Aldrich (item# 650536-1L). For the sample preparation the vessel was throughly washed with ethanol then rinsed with spectroscopic grade methanol followed by a rinse with heptane before filling with benzene solution to full sample volume. Sample volume was usually between $10\,mL$ and $15\,mL$ with the vessel tighly capped. The local experimental area was ventilated to remove accumulated benzene and heptane vapors. The signal acquisition time is 120 seconds with slit widths of $4.0\,mm$, $3.0\,mm$, and $250\,\mu m$ for the input, filter, and main slits respectively. Based on our previous trials with pure benzene, we selected the $260\,nm$

Table 5.3: Summary of benzene solution concentrations and excitation wavelengths.

	Concentration $[M]$			
Excitation $[nm]$	0.25 ± 0.003	1.13 ± 0.014	4.98 ± 0.062	11.25 (99% pure)
258.88	★	★	★	★
259	—	★	—	★
259.12	—	—	—	★
259.25	—	★	★	—
275	—	★	★	—
430	—	—	★	★
450	★	★	★	—

—: no data, ★: data available

absorption system for benzene choosing the ring-breathing mode (ν_2) as a Raman spectral feature reference. Due to the differences in benzene concentration we expect the Raman scattering intensity to decrease with a decrease in concentration. This is the motivation for

choosing the more intensely scattering ring-breathing mode for benzene as our reference. The excitation wavelength was tuned from 258.88 nm to 450 nm in irregular steps. Figure 5.12 shows four of these spectra for resonant excitation at 258.88 nm, with the spectra data series corrected for absorption. For the analysis in Chapter 7 the integrated intensities are considered. These integrated intensity values have an uncertainty of ±3% and wavelength uncertainty of ±0.05 nm. The spectra shows some Raman features for the heptane solute which are well documented [Dollish et al., 1974; Kavitha and Narayana, 2006; Cleveland and Porcelli, 1950]. The benefit of utilizing heptane for these benzene solution studies is lack of absorption features for heptane in our excitation range. Also we have observed that the Raman features of heptane do not show significant changes in energy position or intensity (aside from ω^4 dependence) over this same region.

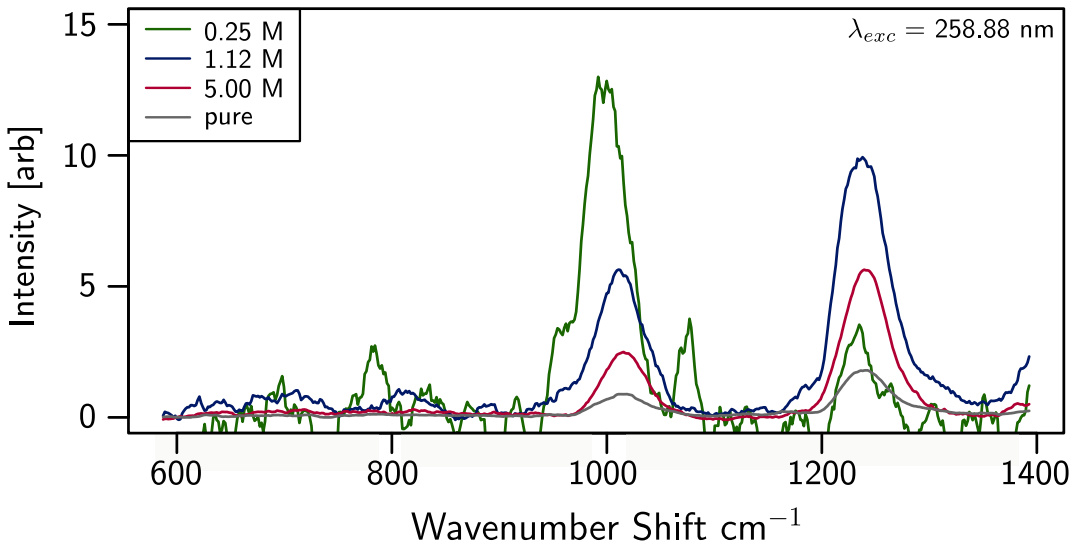

Figure 5.12: Stokes Raman spectra for various concentrations of benzene in heptane solution for 258.88 nm resonant excitation.

Chapter 6

Resonance Raman Scattering from Vapor-Phase Absorption in Liquids

6.1 Overview

The use of high pulse energy laser sources for Raman scattering studies are a necessity for tunable ultraviolet excitation. Typical tunable ultraviolet sources, such as optical parametric oscillators, require high pulse energies ($\sim 0.25\, J\, cm^{-2}$) to achieve adequate ultraviolet light output ($\sim 0.3\, mJ\, cm^{-2}$). Resonance Raman studies utilizing high pulse energy laser excitation sources can be complicated by photo-degradation of the sample material. Photo-degradation is likely occur when the incident light is at or near the high absorption wavelength required to realize resonance enhancement of the Raman scattering intensity. To attempt a remedy, fluid materials are usually flowed or circulated within the interaction region to avoid the localized heating that results in photo-degradation [Asher and Johnson, 1984; Asher, 1993a,b; Chen et al., 1997; Sedlacek et al., 2001]. However, interesting and unexpected behavior is observed when the sample material remains static. We have observed that when the excitation wavelength corresponds to the vapor phase absorption maximum, the sample undergoes a rapid liquid-vapor phase change while simultaneously, recorded the peak intensity Raman signal for both pure liquid benzene and pure liquid toluene. We suggest that the Raman scattering observed is originating from the metastable phase material present as the sample is changing from liquid to vapor. We present a simple model that describes the accumulated pulse energy in the sample for different absorption parameters.

Within a high absorption region, the energy deposited into the sample is sufficient to create a metastable liquid phase material that is responsible for the Raman scattering intensity. Our explanation is supported by the $2\,nm$ to $3\,nm$ discrepancy between the maxima in the liquid and vapor phase absorption spectra for both benzene and toluene. Missing from the previous work in resonance Raman scattering is an explanation of this phenomenon.

6.2 Laser Induced Bubble Formation

High pulse energy laser light is known to break down liquid materials and is commonly referred to as laser induced cavitation [Byun and Kwak, 2004; Felix and Ellis, 1971]. While this breakdown can involve decomposition of the material molecules (photo-degradation), commonly this process is a rapid phase change of the irradiated liquid generating an acoustic shock wave or *popping* sound. Previous work on laser induced breakdown and laser induced bubble formation focus on the time evolution of the bubble formation and subsequent bubble collapse [Dietzel and Poulikakos, 2007; Noack and Vogel, 1999]. For this work, the need for a precise model of the bubble growth is unnecessary. However, the result for our simple qualitative explanation of the bubble formation agrees well established bubble behavior models and provides a reasonable estimate of the observed sound pressure level [Young, 1989]. Figure 6.1 illustrates the bubble formation region inside the sample container. To develop the acoustic radiation model, the following assumptions are made:

- the sample material is static (no flow or circulation) and small scale turbulence due to convection are negligible,
- the liquid surface tension provides a membrane between the bulk liquid and the newly formed vapor,
- the liquid's hydrostatic pressure provides the restoring force on the membrane,
- the oscillation frequency of the membrane's average displacement is the laser pulse repetition rate, and
- the sample container window is considered to be a moving piston which radiates the acoustic intensity that is measured in the lab space.

The model starts with the Young-Laplace equation (Equation (6.2.1)) to relate the internal pressure of the bubble to the surface tension; the driven-circular membrane (Equation (6.2.2)) to describe the displacement of the membrane driven by the hydrostatic pressure,

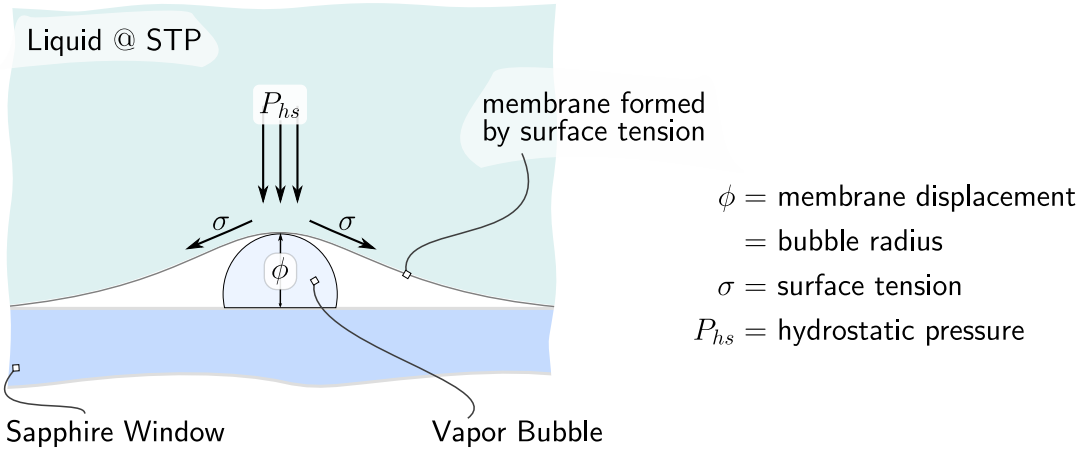

Figure 6.1: Schematic of the liquid-vapor-window interface region.

and the far-field acoustic radiation of a piston (Equation (6.2.3)). Equation (6.2.4) will be use to define the sound pressure level as a function of pressure. Table 6.1 lists the parameter definitions and constant values.

$$\Delta P = \sigma\Big(\frac{1}{R_1} + \frac{1}{R_2}\Big) + P_{atm} \tag{6.2.1}$$

$$\langle\phi\rangle_s = \frac{Pa^2}{\sigma}\frac{1}{ka}\frac{J_2(ka)}{J_0(ka)} \tag{6.2.2}$$

$$P_{ax} = \frac{1}{2}(\rho_0 c_0)U_0\Big(\frac{d}{r}\Big)(kd) \tag{6.2.3}$$

$$SPL = 20\log\Big(\frac{P}{P_{ref}}\Big) \tag{6.2.4}$$

The immediate layer of liquid next to the container window rapidly vaporizes as the laser pulse irradiates the sample producing the bubble. The surface tension of the liquid provides a temporary membrane enclosing the vapor. The bubble is considered spherical and its minimum radius is given the Young-Laplace equation. The membrane diameter is large compared to the bubble diameter which is consistent with the small displacement argument of the driven-membrane equation. The bubble collapses after a short time ($< 1\,\mu s$) before the next laser pulse.[1] The bubble growth displaces the membrane and after the bubble collapses, the hydrostatic pressure of the liquid restores the membrane to the window surface

[1]The time scale for laser induced bubble formation is dependent on temperature, incident power, viscosity and heat capacity of the liquid and these parameters have a very significant effect on time development of

Table 6.1: List of acoustic model parameter definitions and physical constants.

Parameter	Definition	Units
diameter of membrane, a		m
diameter of piston, d		m
pressure across interface, ΔP		Pa
driving pressure, P		Pa
driving frequency, ω		rad/s
wave vector, k	ω/c	$1/m$
speed of piston, U_0	$\langle\phi\rangle_s\omega$	m/s
Bessel functions of the first kind, J_i		
speed of sound in air, c_0	343	m/s
speed of sound in benzene, c_b	1295	m/s
density of air, ρ_0	1.21	kg/m^3
density of benzene, ρ_b	870	kg/m^3
surface tension: benzene, σ_b	28	N/m
vapor pressure: benzene, P_{vap}	12211	Pa
acoustic impedance: air, $\mathbb{Z}_0$	409.8	$Rayls$
acoustic impedance: benzene, $\mathbb{Z}_b$	$1.126e^6$	$Rayls$
reference pressure for SPL, P_{ref}	20	μPa

All values for standard temperature and pressure; from [Kinsler et al., 2000; Sugden, 1922, 1924a,b].

and the process repeats with the next laser pulse.

In our trials we estimate the sound pressure level (SPL) of approximately 20 to 30 dB for the bubble *popping* at approximately $1\,m$. The calculation algorithm follows as:

- calculate the minimum diameter of bubble given the hydrostatic conditions,
- calculate the piston pressure from the estimated SPL,
- calculate the average membrane displacement oscillating at the laser repetition rate,
- recalculate the window's (piston) acoustic radiation using the membrane oscillation as the piston driver, and
- compare the SPL of the calculated piston radiation with the observed SPL (20 to $30\,dB$) estimate.

a bubble [Young, 1989]. Typically time scale measurements rely on shock front measurements not obtained in this work.

Table 6.2 lists these results and given the underlying assumptions presented earlier, these appear reasonable.

Table 6.2: List of calculated bubble acoustic model parameters.

Parameter	Value	Units
Volume of benzene	10.00	mL
P_{hs}	101514	Pa
ΔP	89300	Pa
R (bubble radius)	0.64	μm
a $(50 \times R)$	31.9	μm
$\langle \phi \rangle_s$	453.47	μm
d (piston radius)	20	mm
r (distance from piston)	0.75	m
P_{ax} (calculated pressure)	0.00057	Pa
SPL (calculated from P_{ax})	29.10	dB
SPL (observed)	30.00	dB

Our qualitative model of bubble formation and the mechanism for radiating sound energy is in agreement with more detailed and rigorous quantitative models [Noack et al., 1998; Vogel et al., 1989; Young, 1989]. Understanding the dynamics of the bubble radius will offer improvements to the model we have proposed. Our model assumes that the bubble forms on the inside surface of the window, up to the maximum radius given by the Young-Laplace equation (6.2.1); this may not be strictly true. Vogel et al. [Vogel et al., 1989] show that, depending on the bubble shape (spherical or aspherical), the sound emission can vary significantly depending on the proximity of the bubble to the container surface. They find that a spherical bubble located within its maximum radius (but not necessarily of its maximum radius) to the surface will couple sound energy efficiently to the surface ($\approx 73\%$). Also, they observed that the sound emission process acts as a mechanical damping mechanism impacting the bubble growth. During rapid evaporation, the steady-state assumption of pressure equilbrium across the liquid-vapor boundary for which the Young-Laplace equation is valid no longer applies.

Our results show an appreciable difference between the Young-Laplace radius R and the membrane displacement $\langle \phi \rangle_s$ ($0.64 \mu m$ versus $453.47 \mu m$ respectively). Based on

previous work on bubble formation, our estimated membrane displacement is in better agreement with observed spherical bubble sizes [Noack et al., 1998]. Our assumption of the bubble's radius governed by the Young-Laplace model can be replaced by more rigorous models that incorporate thermodynamic properties of the sample fluid as well as the time evolution of the bubble radius. Additionally, the sound pressure level observed may distort our model calculations. Vogel and Lauterborn [Vogel and Lauterborn, 1988] have shown that the collapse shock has an almost equal contribution to the acoustical emissions as the initial rapid vaporization. Using an acoustical spectrum of the shock, we can determine the bubble's maximum radius from the Rayleigh collapse time [Young, 1989]. However, our SPL measurements do not provide a means to extract an acoustic spectrum. Utilizing a transducer submerged in the fluid would allow an accurate spectrum to be produced as well as eliminate interference from external noise.

6.3 Metastable Phase Model

We have observed a maximum in the Raman scattering intensity from liquid benzene and liquid toluene when these materials are excited with light corresponding to high absorption intensities in their respective vapor phase absorption spectra. Comparison of the liquid and vapor phase absorption spectra show significant offset of the absorption spectral peaks. High resolution ($\sim 0.04\,nm$) vapor phase absorption data from Etzkorn et al. [Etzkorn et al., 1999] and liquid phase absorption data from Inagaki [Inagaki, 1972] and the American Petroleum Institute [API, 1970] show a separation of $3.03\,nm$ (Inagaki-Etzkorn) and $2.03\,nm$ (API-Etzkorn) for benzene and a separation of $2.15\,nm$ (API-Etzkorn) for toluene. The data from API are for liquid solutions of benzene and toluene dissolved in iso-octane and the data from Inagaki is for pure liquid benzene. These absorption spectra are presented in Figures 5.4 (benzene) and 5.8 (toluene) of Chapter 5.

Due to our observation of the maximum Raman scattering occurring on the vapor phase absorption profile and the observation of bubble production during resonant excitation, the scattering medium is expected to be vapor phase. However, the bubble formation model presented in the prior section, as well as other studies on laser induced bubble formation, poses as problem. Should the Raman scattering originate from a true vapor, the bubble will need to developed for a majority of the laser pulse lifetime. Bubble formation is

a function of the time evolution of the energy deposited into the illuminated volume [Noack et al., 1998; Byun and Kwak, 2004; Noack and Vogel, 1999]. Noack et al. [Noack et al., 1998] have shown that the pulse energy required to produce laser induced breakdown in liquid water decreases as pulse width decreases. They show that short pulse durations on the order of a few picoseconds yield small bubble radii ($\sim 80\,\mu m$) whereas longer durations of $\sim 6\,ns$ yield larger bubble radii ($\sim 800\,\mu m$). Bubble expansion is determined from shock front measurements and the shock signal intensities typically peak approximately $40\,ns$ after the incident light pulse begins (for $\sim 6\,ns$ pulse duration) [Vogel et al., 1996]. This suggests that a vapor bubble may not be fully developed within the pulse lifetime.

While it is certain a vapor bubble is forming, there is little reason to suspect the observed scattering intensity is from the vapor state. From previous measurements using our system, the likelihood of observing any detectable scattering signal level from a small volume of vapor is small for a few reasons. Using the OPO system's pump laser ($355\,nm$, $\sim 27\,mJ/pulse$) to illuminate the laboratory air, we were able to weakly detect Rayleigh scattering intensity (90 degree scattering configuration) from the laboratory air (nitrogen, oxygen, air particulates). Given that the Rayleigh scattering cross-section is approximately 3 to 4 orders of magnitude larger than than of non-resonant Raman scattering cross-section, this does not offer much promise to capturing Raman intensity for the small number densities inside laser induced bubbles. Considering the ideal gas approximation, the number density of vapor phase molecules available to scatter are approximately 3 orders of magnitude smaller than that in liquid phase. Table 6.3 lists the estimated number densities for a bubble with a radius of $800\,\mu m$, similar to that depicted in Figure 6.1). Also, the mean ultraviolet OPO pulse energies for resonance excitation in benzene ($259 \pm 4\,nm$) and toluene ($266.7 \pm 4\,nm$) are $\sim 0.18\,mJ/pulse$ and $\sim 0.3\,mJ/pulse$, respectively, further reducing available Raman scattering intensity. Finally, the images obtained for the laboratory air Rayleigh scattering utilized an image integration time of $5\,min$ whereas the images obtained for Raman scattering in both benzene and toluene utilized image integration times of $2\,min$.

Due to the rapid phase change the liquid undergoes during the pulse lifetime when the excitation wavelength is within a highly absorbing region, a metastable phase fluid is very likely. The increased local heat would result in a grouping of molecules with increased intermolecular spacing whose Raman scattering intensity becomes shifted toward that ob-

Table 6.3: Estimated number densities and mean free paths for benzene, toluene, and air.

	Number Density			Mean Free Path $[m]$		
	gas (g)	liquid (l)	l/g ratio	gas (g)	liquid (l)	l/g ratio
benzene	4.2553e+16	1.0834e+19	254.6	1.6264e-8	7.7424e-11	0.0048
toluene	4.5183e+16	9.0638e+18	200.6	1.3166e-8	8.2168e-11	0.0062

Number density is calculated from the van der Waals equation of state for gas phase and molar volume for liquid [Lide, 2008]. The bubble volume is $1.6085e-9\,m^3$, the temperature is $298\,K$, and the bubble pressure is $101.51\,kPa$.

served in the vapor phase. As a first approximation, the mean-free path length for a gas is about 200 times larger than for liquid (210 for benzene and 160 for toluene) indicating a large range for which a metastable fluid may exist before the liquid-vapor phase change occurs [Stowe, 1984]. To gain insight into the metastable fluid and the shift of the Raman line toward vapor, consider the temporal evolution of the energy deposited into the scattering interaction region. The time development of the power of a single laser pulse can be represented by a *sine*-squared function such that:

$$P_{las}(t) = P_{las,0}\sin^2\Big(\frac{\pi}{2\tau}t\Big), \quad \text{for } 0 \le t \le 2\tau, \tag{6.3.1}$$

where $P_{las,0}$ is the average pulse power and 2τ is the laser pulse width (FWHM). Time integration of the power gives the time evolution of the laser pulse energy giving:

$$E_{las}(t) = \int_0^t P_{las,0}\sin^2\Big(\frac{\pi}{2\tau}t\Big)dt = P_{las,0}\Big\{\frac{t}{2} - \frac{\tau}{2\pi}\sin\Big(\frac{\pi}{\tau}t\Big)\Big\}. \tag{6.3.2}$$

The energy will be deposited into the effective volume enclosed by the laser beam. As previously discussed, the effective volume (described equivalently by EPL_d, Equation (4.3.2)) is dependent on the excitation wavelength (see Section 4.3). Table 6.4 lists a selection of the calculated penetration depths for benzene as determined earlier from our absorption correction model for some experimental wavelengths and corresponding average laser power. For the listed ultraviolet wavelengths, bubble formation was easily observed in pure liquid benzene and observed at $259\,nm$ in the $4.99\,M$ solution of diluted benzene. For the lower concentration solutions, no bubble formation was detectable. Similar behavior was observed for pure toluene.

Figures 6.2 and 6.3 show the pulse energy deposited into the effective volume for benzene for different excitation wavelengths for pure benzene and a $1.12\,[M]$ solution of

Table 6.4: Calculated penetration depth for experimental excitation wavelengths and average laser power in pure liquid benzene.

excitation wavelength $[nm]$	258.75	259.00	259.25	260.00	430.00
average laser power $[\mu W]$	1750	1400	2100	1990	5500
penetration depth (EPL_d) $[\mu m]$	11.000	0.507	2.390	1.810	195.0
laser repetition rate	$10\,Hz$				
laser pulse width (FWHM)	$\approx 8\,ns$				

benzene in heptane. Figure 6.4 shows the pulse energy deposited into the effective volume for pure toluene for different excitation wavelengths. The energy deposited is normalized to units of enthalpy of vaporization of the species ($\Delta_v H = 33.83\,kJ\,mol^{-1}$ for pure liquid benzene and $\Delta_v H = 38.01\,kJ\,mol^{-1}$ for pure liquid toluene, both at $298\,K$) [Lide, 2008]. For all three figures, the average laser power is $1\,mW$, the laser pulse width is $8\,ns$, and utilize the vapor phase absorption data from [Etzkorn et al., 1999]. Figure 6.5 shows the pulse energy deposited into pure benzene for the experimental values listed in Table 6.4. All figures show an overlay of the laser pulse approximated as a Gaussian distribution with FWHM of $8\,ns$ for reference. When the excitation wavelength is on the peak absorption, the energy sunk into the effective volume is several times larger than the enthalpy of vaporization before the majority of the pulse has developed. A study of laser-induced breakdown in liquid water by Vogel et al. [Vogel et al., 1996] has shown that for energy densities of approximately 20 times that of the enthalpy of vaporization are more than sufficient to form cavitation bubbles for similar pulse widths $6\,ns$. This suggests that for those excitations very close to the absorption peak, the Raman scattering signal may originate from the highly disordered, metastable fluid undergoing a phase transition. Also, this provides an explanation of the possible shifting of the Raman peak profile toward the Raman line center attributable to vapor phase scattering, away from the line center for liquid phase scattering.

6.4 Mass Spectroscopy Examination and Results

There is currently no assessment of the effect that laser-induced breakdown may have on Raman scattering spectra of a sample. Studies on laser ablation in benzene and other hydrocarbons suggest that with significant laser fluence, samples not only exhibit

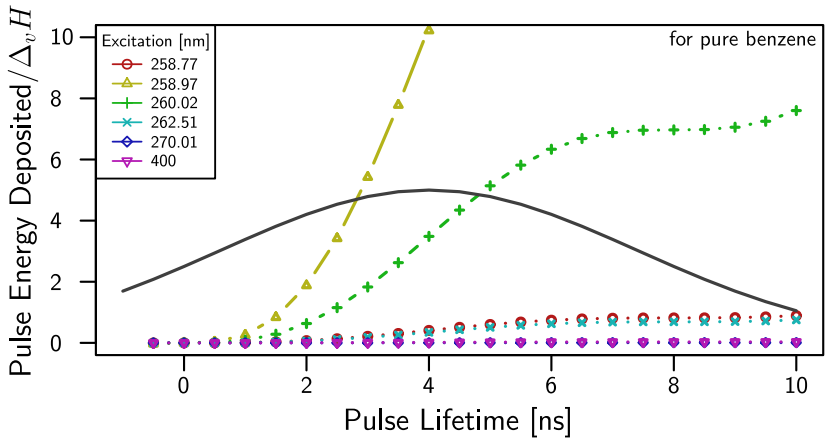

Figure 6.2: Time evolution of the energy deposited into the effective volume of pure toluene for average laser power of $1\,mW$ and pulse width of $8\,ns$ for several excitation wavelengths.

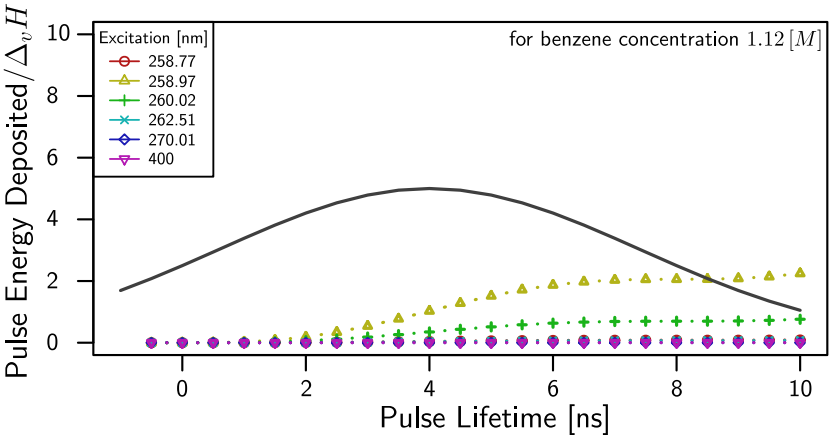

Figure 6.3: Time evolution of the energy deposited into the effective volume of pure toluene for average laser power of $1\,mW$ and pulse width of $8\,ns$ for several excitation wavelengths.

cavitation bubbles, but may experience photochemical reactions [Toyota et al., 2000, 2001; Katoh et al., 1998; Tsuboi et al., 1994]. Toyota et.al. [Toyota et al., 2000] has shown that under irradiation with nanosecond, $1064\,nm$ laser light, fractured components are produced in liquid benzene. The mechanism for the laser induced breakdown in their work relies on the microwave breakdown theory; the strong electric field of the laser is sufficient to ionize a benzene molecule. They observed laser induced breakdown in liquid benzene at $1064\,nm$

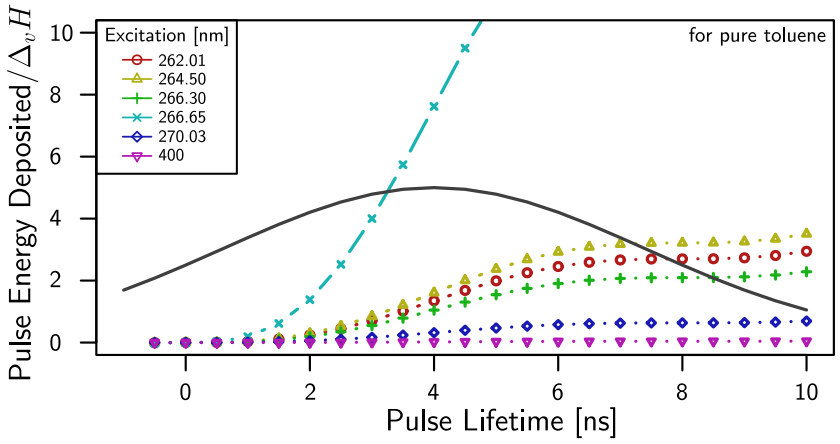

Figure 6.4: Time evolution of the energy deposited into the effective volume of pure toluene for average laser power of $1\,mW$ and pulse width of $8\,ns$ for several excitation wavelengths.

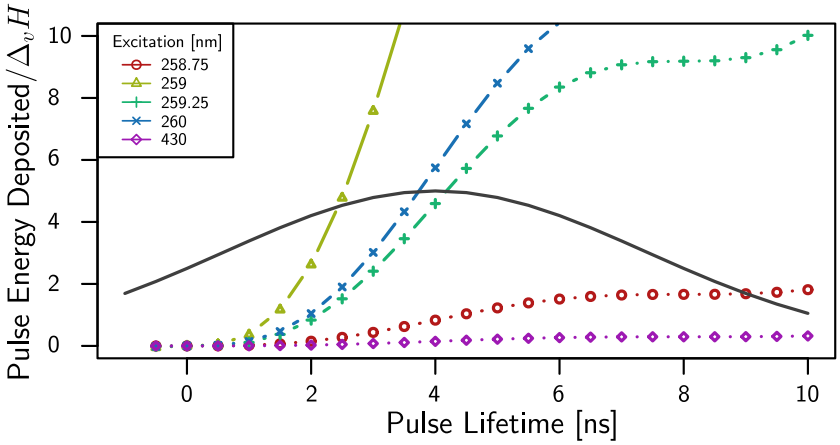

Figure 6.5: Time evolution of the energy deposited into the effective volume of benzene for the experimental values in Table 6.4.

with an electric field strength at the focal point of $4.5 \times 10^9\,V\,m^{-1}$ [Toyota et al., 2000]. By comparison, with our unfocused beam, the electric field strength is expected to be close to $4.3 \times 10^5\,V\,m^{-1}$, suggesting fractured components may not be produced in the viewpoint of this mechanism. An alternative picture is presented by Tsuboi et.al. [Tsuboi et al., 1994] investigating laser ablation in liquid hydrocarbons utilizing a $248\,nm$ KrF excimer laser. They observe ablation and decomposition with moderate laser fluences, $\sim 100\,mJ\,cm^{-2}$ for benzene and $\sim 35\,mJ\,cm^{-2}$ for toluene. They concluded that explosive boiling and vapor-

ization are unlikely candidates for the ablation, and that photochemical fragmentation of the sample is a more reasonable mechanism as explained by the positive correlation between the photochemical reactivity and the laser fluence threshold of the ablation [Tsuboi et al., 1994]. These results were also confirmed by Katoh et.al [Katoh et al., 1998] in their investigation of photo-decomposition of liquid benzene using a $193\,nm$ ArF excimer laser.

We have attempted to classify, using mass spectrometry, the level of fractured components produced in a $1.12\,[M]$ diluted benzene (in heptane) solution after illuminated with light tuned onto the $259\,nm$ absorption resonance. We have previously observed the laser-induced breakdown in pure and $5.00\,[M]$ solutions of benzene while on this absorption resonance. We choose a lower concentration of $1.12\,[M]$ to take advantage of a longer penetration depth into the sample to increase the probability of generating measurable quantities of fractured components without limiting the interaction region to layers close to the vessel window. For the solution preparation, we heated approximately $250\,mL$ of heptane to $\sim 70\,^{\circ}C$ over a period of 2 hours before making the benzene solution. The solution was then divided into three $50\,mL$ vessels. For exposure, $10\,mL$ of each solution was transfered to the PTFE $10\,mL$ sample holder (same holder for each exposure, thoroughly cleared between each sample) and placed lengthwise in the beam path. Two samples were exposed, one for 30 minutes and one for 90 minutes with the remaining sample as a control. The average laser power over these exposures was $2.5\,mW$. After exposure the samples were returned to their respective containers and refrigerated until mass spectrography was performed (less than 36 hours).

Our mass spectrometry results are inconclusive, for several reasons. Benzene and heptane were clearly identified in the spectrogram of all samples. No significant fractured components such as methyl group or phenyl ring fragments were observed in the exposed samples not also observed in the control. Smaller atoms, specifically hydrogen, were not observed in any significant level over the expected mass spectrometer instrument generated cracking residues. These results seem to suggest that no significant generation of fractured molecules is occurring. Considering the results given by Katoh et.al, two likely explanations arise. One, our laser fluence is small. As we are not focusing the light into the sample space, our laser fluence is $\sim 0.25\,mJ\,cm^{-2}$, as compared to their laser fluence, ~ 80 times larger

than our system. For a fluence of $2.6\,mJ\,cm^{-2}$, they have shown very small production yield for biphenyl (relative yield of ~ 0.25), whereas for a larger fluence of $34\,mJ\,cm^{-2}$, biphenyl production yield is much larger (relative yield of > 300) [Katoh et al., 1998]. Two, the concentration of our solution may not be conducive to fragment production. They show that for sufficient laser fluence ($34\,mJ\,cm^{-2}$), the production yield for biphenyl decreases as the solution concentration is reduced. Given our mass spectrometer results, laser fluence, and low concentration, production of fractured components is unlikely.

Chapter 7

Utility and Limitations of Resonance Raman Scattering

7.1 Article Abstract

The utility of the resonance Raman effect in terms of the real measured signal level is investigated using a tunable light source. The strong $1332\,cm^{-1}$ vibrational mode of diamond and the $992\,cm^{-1}$ ring-breathing mode of benzene (pure and diluted solutions) are used to probe signal strength and resonant Raman signal enhancement as the excitation energy is tuned over an ultraviolet absorption line. A trade-off is shown between the inherent wavelength dependent species absorption and the magnitude of the resonance enhancement in determining the real measured signal level. The full magnitude of the enhancement is realized in the per-molecule cross-section, but not the real signal levels. This trade-off is identified by comparing the absorption corrected signal level to the real measured signal level for diluted benzene in heptane. For strongly absorbing materials, resonance enhancement in the real Raman signal level is likely to be overcompensated by the species absorption. Using naphthalene dissolved in heptane, no Raman signal was observed, as expected when absorption wins the trade-off for a highly absorbing material. Two different regimes have been identified where resonance Raman dramatically increases the real signal level despite the presence of strong absorption. Materials identification in trace species such in remote sensing and tiny working volumes such as near-field optical microscopy.

7.2 Article Introduction

Resonance Raman spectroscopy can provide signal enhancements several orders of magnitude over that seen with normal Raman on a molecule by molecule cross-section basis [Kudelski, 2008; Asher, 1993b; Clark and Dines, 1986]. Recent work has documented many of the benefits of resonance Raman. These include: species identification with specificity that exceeds non-resonant Raman and signal enhancement that rivals fluorescence [Asher and Johnson, 1984; Asher, 1984; Efremov et al., 2008]. Much of the current use of resonance Raman techniques utilize visible and infrared portions of the spectrum, which limit the types of molecules that can be studied. Ultraviolet light can provide resonances in more materials, but investigations are hampered by available tunable light sources, complications relating to sample damage, and fluorescence [Asher and Johnson, 1984; Kudelski, 2008]. The deep ultraviolet (DUV) resonance Raman regime escapes fluorescence background from both the species examined and the local environment, as very few species have significant fluorescence emission below $\sim 280\,nm$, even for shorter wavelength excitation, due to pre-fluorescence electron relaxation. Probing in the DUV region also allows access to a range of potentially interesting electronic absorption features [Asher and Johnson, 1984; Ziegler and Albrecht, 1979; Gerrity et al., 1985; Asher et al., 1983].

A drawback of probing in the DUV region, not emphasized in previous work, is the increase in species absorption. When the excitation wavelength is tuned to an absorption feature to instigate resonance, the wavelength is always within an absorbing band. Additionally, the Raman shifted wavelengths are usually within the absorption band, so absorption occurs both as the excitation light enters and as the signal light exits the sample space. This is why raw, measured Raman intensities for bulk species typically do not increase in the resonance Raman regime. While scattering cross-sections are larger than normal Raman, the effective number of molecules observed is significantly reduced, to those within a thin surface layer. In this paper, we examine the trade-off between resonance enhancement and absorption to illustrate when resonance-Raman is beneficial. In particular, we find: *a)* resonance enhancement can be obtained in high absorption species where normal Raman signals are very weak, *b)* due to this enhancement, low number densities can be probed effectively, which benefits trace sample and small volume measurements, and *c)* the trade-off existing between resonance enhancement and absorption is the determining factor in utilizing resonance Raman enhancement.

The application of the resonance enhancement to remote sensing has taken recent interest, largely in the application to Raman light ranging and detection (Raman-LIDAR) [Willitsford et al., 2008]. Preresonance enhanced Raman LIDAR has been used to profile and identify trace atmospheric species (sulfur dioxide, carbon tetrachloride, nitrogen dioxide, nitrobenzene) [Rosen et al., 1975; Chen and III, 1996; Sedlacek et al., 1994; Chen et al., 1997]. A recent examination on the use of ultraviolet resonance Raman for stand-off detection of roadside bombs and improvised explosive devices indicates that the enhancement may be limited by heavy absorption [Johansson et al., 2008]. We present here an accounting of the limitations imposed by the absorption character of the analyte being probed, how the limitations will modify the signal, and use diluted solutions of benzene in heptane as example cases. These results suggest use of this enhancement mechanism in near-field scanning optical microscopy (NSOM). Previous work on NSOM Raman has shown considerable limitations due to tiny signals that give long signal integration time, extending the instrument design and stability requirements not necessary in normal NSOM systems [Jahncke et al., 1995; Ayars et al., 2001]. Since NSOM Raman yields additional information not obtained with far-field Raman techniques [Jahncke and Hallen, 1996; Hallen et al., 2003] any significant enhancements in signal are advantageous [Jahncke et al., 1996].

7.3 Experimental Description

Continuously tunable light from $700\,nm$ to $420\,nm$ is generated utilizing an optical parametric oscillator (OPO) [U-Oplaz OPO BBO-3B (Type I, Model S)] pumped by the third harmonic of a Nd:YAG laser [Spectra-Physics Quanta Ray INDI-50-10]. The visible signal output of the OPO is then frequency doubled by a second harmonic stage [U-Oplaz OPO BBO-SHG (Type I, Model S)] to yield continuously tunable output from $355\,nm$ to $210\,nm$. The average power across this wavelength range is $2\,mW$. The OPO uses Type-I phase matching rendering an average bandwidth of $30\,cm^{-1}$ between $355\,nm$ to $210\,nm$. The pulse length is $8\,ns$, with a $10\,Hz$ repetition rate, and a beam diameter of approximately $8\,mm$. An unfocused excitation beam provided the Raman signal that was collected in a standard 90 degree scattering arrangement and transfered into a triple stage $0.6\,m$ spectrometer [SPEX Triplemate 1877]. The system resolution is limited by the bandwidth of our OPO.

Sample selection was based on absorption features within our OPO tuning range. Diamond was selected since the absorption increases dramatically at its band gap energy at $\sim 205\,nm$. Benzene has several absorption features within this range and is a good reference material due to significant previous work. Toluene and naphthalene were also selected. Both have higher absorption intensities than benzene, but have many chemical similarities. Absorption data in vapor-phase benzene by Etzkorn, et al. provided us with a sufficient resolution [Etzkorn et al., 1999] that fine resolution steps could be taken without missing Raman features. Knowledge of the absorption features at high resolution is also used to predict the absorption of the Raman signal as it exits the sample. The benzene and toluene samples were liquid-phase and housed in a custom made polytetrafluoroethene (Teflon) container with a sapphire window. The sample holder was arranged in a 90 degree scattering configuration, with both the incident and collected light passed through the sample holder window. Loss introduced by the spectrometer and camera are estimated to give an overall efficiency of 5%. Measurement error in wavelength, relative intensity and concentration are $\pm\,0.05\,nm$, $\pm\,2.5\%$, and $\pm\,0.03\%$ respectively and are within the dimensions of the point labels in the figures. Our measurements fell into three main thrusts: *a)* observation of resonance enhancement in a pure sample environment, *b)* observation of resonance enhancement in diluted sample environments, and *c)* tuning on and off resonance.

7.4 Results and Discussion

To gain insight as to what happens as we approach a strong absorption feature, diamond (rough faceted) is a good sample, due to its well known Stokes shifted Raman line at $1332\,cm^{-1}$. A naive expectation is that an increase in the Raman intensity should be observed as we tune closer to the band gap. Indeed, this is the extrapolation of previous pre-resonance Raman studies with tuned excitation wavelengths [Calleja et al., 1978]. However, we observed the opposite, as detailed in Figure 7.1. Calleja et al. observed a mild increase in Raman intensity as the excitation wavelength was tuned from $647\,nm$ to $257\,nm$ [Calleja et al., 1978]. Instead, we observed a strong decrease in the Raman signal below $300\,nm$, Figure 7.1, that corresponds to that expected from the absorption coefficient, [Edwards and Philipp, 1985], also shown (scaled $10\times$). For reference, the band gap is indicated by A, and

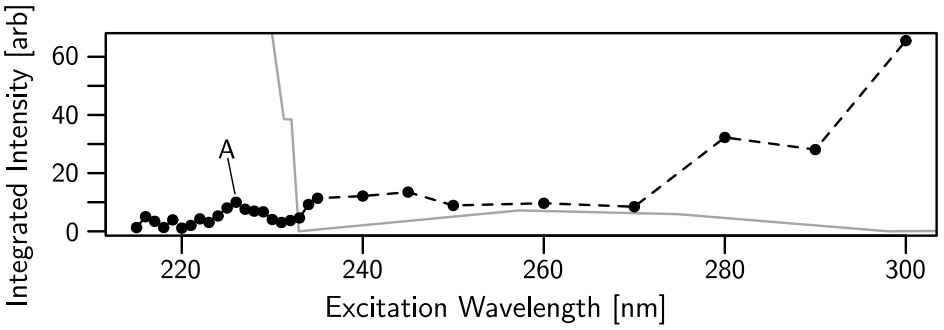

Figure 7.1: Solid points connected by dashed line: integrated Stokes Raman intensities for diamond, centered on $1332\,cm^{-1}$ as the excitation is tuned from $215\,nm$ to $235\,nm$ in $1\,nm$ steps and to $300\,nm$ in larger steps. Solid line: absorption coefficient (scaled $10\times$), from [Edwards and Philipp, 1985]. The A indicates the band gap edge at $\sim 5.5\,eV$.

appears to produce some resonant gain. Our interpretation of the additional features in Figure 7.1 is that the intensity variation is due to surface/bulk contaminates inherent in natural diamond and possible indirect band transitions. Graphite is known to have Raman features in the range of $\sim 1300\,cm^{-1}$ to $\sim 1450\,cm^{-1}$ (Stokes) [Leeds et al., 1998] so graphite contamination may be visible.

Benzene and toluene were probed about their first set of absorption features at $259\,nm$ and $267\,nm$, respectively. These features represent spectra assigned to the fundamental C-C stretching mode of the phenyl ring with Stokes Raman shifts at $\sim 992\,cm^{-1}$ and $\sim 1004\,cm^{-1}$, respectively. While probing benzene around the higher energy $253\,nm$ and $247\,nm$ absorption features, we found that the resultant Raman signal tended to overlap with the lower energy absorption features (for excitation wavelengths less than $255\,nm$). It should be noted that these absorption features are spaced by the vibrational levels of the same C-C stretch in benzene [Callomon et al., 1966]. Toluene shows similar spacing with different peak intensities due to the attached methyl group [Etzkorn et al., 1999]. This additional absorption resulted in far less intense signal than the lowest energy absorption feature, illustrating the importance of resonance feature choice in the resonance/absorption trade-off.

The high absorption of benzene in the DUV region generally limits probing to a layer thickness of a few hundred nanometers for a pure sample. Conversely, the full sample

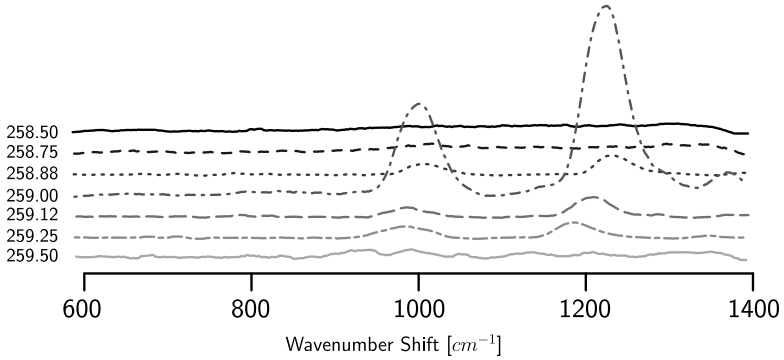

Figure 7.2: Stokes Raman spectra for pure liquid benzene, centered on $\sim 992\,cm^{-1}$. Tuning from $258.5\,nm$ to $259.5\,nm$, excitation wavelength indicated left of the spectra.

depths ($5\,mm$ to $15\,mm$) can be probed in the visible wavelengths due to weaker absorption at longer excitation wavelengths. The sampled volume is limited by the collection scheme. In the pure sample case, our typical Raman peak height as we tuned the excitation wavelength $\pm 1\,nm$ over an absorption peak at $258.88\,nm$ was approximately 9 times larger at the absorption peak than off it clearly marking the resonant enhancement and is shown in Figure 7.2. This enhancement does not take into consideration the self absorption. Similar narrow band enhancements are observed for diluted benzene. While increasing our interaction depth within the sample volume, we still probe only a rather small volume (ranging from several hundred nanometers to a few microns in depth) due to the intense absorption.

Previous work [Asher, 1984; Jones et al., 1985] has shown that low concentration environments can be probed via resonance Raman due to the appreciable enhancement yielded as an electronic absorption is approached. We should emphasize that in these studies, what is typically described as resonance enhancement is actually pre-resonance enhancement. We have observed resonant behavior, as we have tuned the excitation wavelength across absorption features. Figure 7.3 (top panel) compares the peak area of four different concentrations of benzene dissolved in heptane across a range of excitation wavelengths. As concentration is reduced, the resonant enhancement begins to dominate over the non-resonant Raman as the trade-off shifts from absorption to resonance. Important to note is that these data are only corrected for the instrument effects. Sample self absorption and the well known Raman frequency dependence (ω^4) are not included. This suggests

that when sample concentration or volume is small, the resonant enhancement can allow for Raman studies where non-resonant Raman signals are negligible or maybe masked by fluorescence or Raman signals from the ambient matrix, since real, uncorrected, signal levels are increased. As concentration is increased, non-resonant Raman signal begins to become comparable to those resonantly enhanced. Without absorption, the enhancement allows one to access Raman information in environments where non-resonant Raman signals are too weak due to a lower number of potential scattering agents. This suggests applications in low sample volume environments such as encountered in NSOM, where probe properties and operational parameters lead to tiny sampling volumes, typically of order $(\lambda/3)^3$ or less [Huerth et al., 2000; Jahncke et al., 2002] as well as sparse sample environments like those encountered in LIDAR where typical number densities can be small (ppm to ppt) [Toriumi et al., 1996; Rosen et al., 1975].

Alternatively Figure 7.3 (bottom panel) shows the same data corrected for absorption, giving effectively a per-molecule cross-section comparison. As expected, the resonant enhancement dominates at all concentrations relative to the non-resonant case, note the ordinate scale. By adjusting for the self-absorption of the species, the magnitude of the resonant enhancement becomes more clear, suggesting that the enhancement becomes more significant when concentration is increased as with pure benzene. The presence of overtone enhancements, the additional species discrimination provided by excitation resonance, and the Raman fingerprint offer further advantages to resonance Raman in either case.

Figure 7.4 gives another comparison of when resonant enhancement is useful. Plotted is the ratio of the UV to visible Raman signal levels; again both measured signal levels and absorption-corrected data are shown. When concentrations are high, no significant gains in measured signal level over that obtained in non-resonant Raman are apparent (ratio values close to unity). However, lower concentrations begin to show very significant enhancements over non-resonant Raman. While not obvious from Figure 7.3 (bottom panel), the gain over non-resonant is most significant when on top of the absorption peak ($258.88\,nm$, indicated by the up-pointed arrow). When self-absorption is taken into consideration, the domination is even more pronounced as detailed in the right panel (note the different ordinate scales). The right panel contains just the enhancement, so a compari-

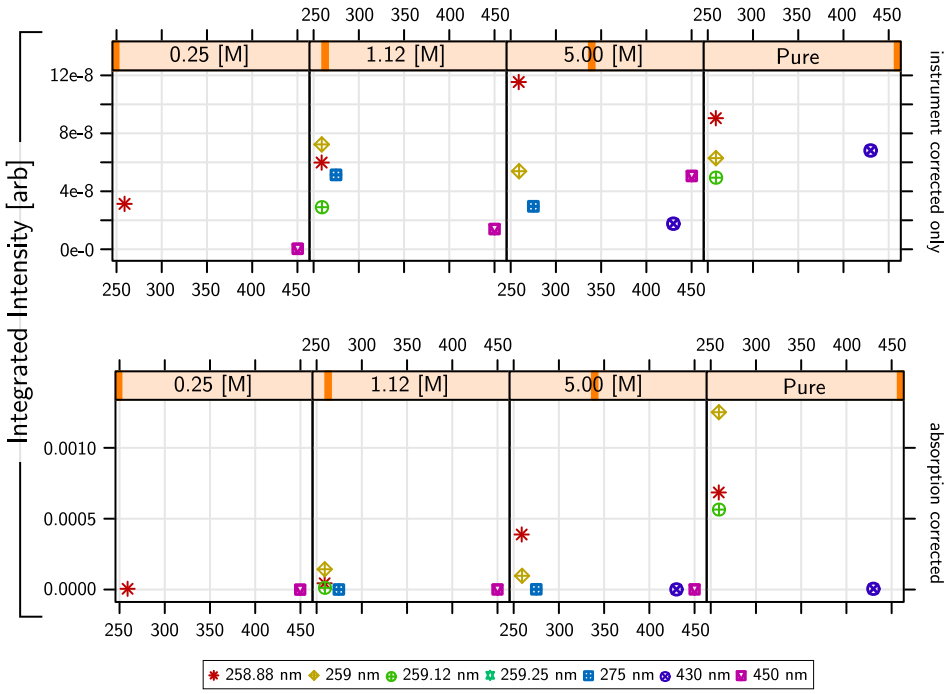

Figure 7.3: Two methods of quantifying resonance gain. Top: integrated Stokes Raman intensities for benzene in heptane at various concentrations for different excitation wavelengths adjusted only for instrument variation. This is referred to the 'raw' or real measured signal. Bottom: integrated Stokes intensities where both the instrument variation and species self-absorption are corrected.

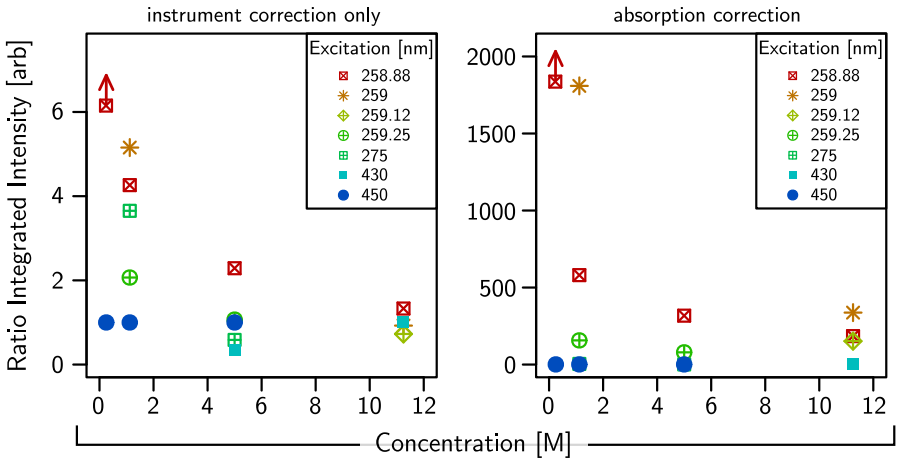

Figure 7.4: The ratio of all integrated intensities to the non-resonant integrated intensity across concentration provides a normalized indication of signal gain. Left: indicates the real measured signal gain by adjusting only for the instrument variation. Right: also adjusts for the species self-absorption for cross-section comparison. The arrow indicates a point outside of the vertical scale.

son of the two shows the dramatic trade-off between absorption and enhancement: higher concentration means higher absorption and in turn less enhancement of real measure signals.

A final confirmation of the absorption-resonance trade-off is observed in a highly absorbing species, naphthalene. As previously noted, naphthalene has a significantly higher absorption than benzene (approximately 30 times that of benzene at the same wavelength). We were unable to obtain any UV Raman signals for milli-molar concentration naphthalene-heptane solutions or for naphthalene in vapor phase. Naphthalene's high absorption combined with the effective smaller number densities, our conclusion is not that obtaining a signal enhancement is not possible but rather there appears to be a diminishing return that is dependent on intensity of absorption and the inherent difficulty of obtaining Raman signals with vapor-phase materials. We believe the lack of more intense pre-resonance enhancement in our benzene and toluene trials confirms this assertion as well.

The trade-off between high absorption reduction of the Raman and excitation signals and the potential enhancement opportunity is both material and absorption line dependent. Not all materials are amenable to gains in measured resonant Raman signal even at low densities, since the resonance never surpasses the absorption. The situation

is similar for the 247 nm and 253 nm absorption lines of benzene; the absorption of the Raman-shifted light is too large. The more properly chosen 259 nm absorption places the Raman-shifted light in a lower absorption region, where the trade-off is favorable.

7.5 Conclusions

Resonance-Raman scattering in the DUV region has been shown to provide significant enhancement over non-resonant Raman in species that exhibit high absorption. However, this enhancement is tempered by the loss caused by the strong absorption of the same absorption feature responsible for resonance. When the concentration/volume of heavily absorbing molecules is large the real (raw) measured UV resonance Raman signal is not significantly larger than non-resonant Raman with visible excitation. We have observed with different concentrations of benzene dissolved in heptane that Raman signal enhancements become more significant as the concentration is reduced and maximized when an electronic absorption band is chosen for minimal absorption of the Raman-shifted light. Also, we have confirmed the enhancement/absorption trade-off with a more intensely absorbing species, naphthalene. With the enhancement, low sample density environments, as in trace gas analysis with LIDAR, and low sample volumes, as with NSOM, will be studied much more easily. Species identification will also be improved as the Raman fingerprint is augmented by the material-dependent excitation energies of resonance.

Chapter 8

Conclusion

Much of the previous work in experimental resonance Raman scattering utilize discrete excitation wavelengths to investigate a molecular system. The restriction on excitation wavelengths means that many examinations only realize preresonance Raman signal enhancements and may overlook important spectrographic information available when tuning the excitation wavelength through a system's absorption band. Utilizing an optical parametric oscillator to provide continuously tunable ultraviolet light, we have examined resonance Raman scattering in several materials. Our most impressive and detailed results involve resonance scattering in liquid benzene about the $260\,nm$ benzene absorption system. We have found sharply increasing Raman scattering intensity, as much as six orders of magnitude, within a small range of $\pm 0.25\,nm$ about the $259\,nm$ absorption peak in liquid benzene as shown in Figure 5.6. This rapid increase in scattering intensity has immediate application to remote sensing signal detection enhancements as well as signal enhancement in nano-scale NSOM Raman studies. We have also confirmed similar behavior in liquid toluene. In toluene, we have observed sharply increasing Raman scattering intensity, as much as four orders of magnitude, within a range of $\pm 0.25\,nm$ about $266.83\,nm$ as shown in Figure 5.10. Additionally, we have compiled as comprehensive list of potential excited state vibrational assignments for liquid benzene, Table 5.1 and liquid toluene, Table 5.2 not previously reported. These excitation tuning results in benzene and toluene serve as a base to expand future tunable excitation studies in other materials and initiate an understanding the underlying physical processes occurring in the narrow widths about absorption band peaks.

Paramount to our interpretation of the experimental spectra is understanding the role of absorption in the sample material. We have presented an intuitive model of the excitation and signal light attenuation within the sample. The model allows us to describe the overall effect of species absorption as a single parameter, the effective path length EPL_d (Equation (4.3.2)). When estimating the level of resonance enhancement, the effective path length is used to normalize the sampling space such that we compare the scattering intensities on a per molecule basis. Using three solutions of liquid benzene in heptane and pure benzene, we have demonstrated the limitation absorption can affect on the resonance enhancement. Looking at the ratio of resonant to non-resonant integrated Raman intensities for different concentrations (Figure 7.4), we have shown that if the influence of absorption is considered, the resonance gain is an appreciable four to five orders of magnitude for low concentration samples. However, if the absorption is not considered, the intensities of resonant and non-resonant signals are comparable. Also, we have confirmed the utility of resonance Raman for small sample concentration and tiny sampling volume Raman studies by showing that the signal level in a low concentration environment is similar to higher concentration non-resonant signal levels.

One of the most interesting aspects of this work is absent from the prior literature. We have found that when the excitation wavelength is tuned to an feature in the vapor phase absorption profile, we realize the maximum resonance enhancement. This has been observed in both liquid benzene and liquid toluene. When the absorption spectra of liquid phase and vapor phase benzene are compared, the absorption maxima are significantly offset, between $2\,nm$ to $3\,nm$. Toluene shows the same absorption spectra offset. To explain this unexpected behavior, a model of the time evolution of the energy per pulse deposited into the sample space is introduced. The effective volume of the sample space is dependent on the sample's absorption profile; on resonance the effective volume is small, off resonance the volume becomes larger. What is clear from our model is that the energy deposited into the smaller on-resonance volume is sufficient to promote a liquid-vapor phase transition. For off-resonance excitation at $259.25\,nm$, the energy deposited in $4\,ns$ in liquid benzene is approximately 1.5 times the enthalpy of vaporization of benzene. Whereas on-resonance excitation at $259\,nm$, the energy deposited in $4\,ns$ is approximately five times the enthalpy

of vaporization. We suggest that this highly disorganized fluid is responsible for the Raman scattering we have observed. Also for both benzene and toluene, when the excitation light is on their vapor phase absorption peaks, an audible acoustic shock (popping) is observed. This popping confirms that a rapid phase is occurring. A crude qualitative model of this vapor bubble is presented.

8.1 Future Work

The findings in this work provide several starting points that may be valuable to future experimental and theoretical studies. There are several aspects that would be fruitful to explore.

- The preliminary data presented for benzene and toluene serve to motivate additional resonance Raman study of these molecules. What is not clear from the current studies is the nature of the excited state active when the systems are under resonance excitation. Investigation of these molecules with finer resolution excitation tuning will extend the knowledge base not only of these materials, but also of the underlying physical processes while on resonance. Also, to our knowledge, comprehensive experimental data on the first excited states in benzene and toluene are not presented in the current literature. Our results should provide motivation for a detailed theoretical examination of the excited states of these molecules.
- To further bolster our explanation of vapor phase Raman scattering in a liquid sample presented in Chapter 6, molecular dynamics simulations may offer new insights. While our description offers a solid qualitative and semi quantitative model of the physics, molecular dynamics simulation may help formulate a more robust general model of the scattering medium.
- The one facet of this work was to determine what materials may show resonance enhancement and at what level these may be detectable using resonance Raman. Certainly more materials warrant study. A group of materials of interest to the defense and homeland security communities is double and triple bonded nitrogen compounds. These compounds and related by-products are commonly found in many commercial and improvised explosives. Preliminary study of these materials will serve as a necessary step in developing any field instrument.

- Resonance Raman scattering is also of significant interest in expanding the experimental techniques of near-field scanning optical microscopy (NSOM). The NSOM laboratory at North Carolina State University is currently developing a first generation resonance Raman NSOM system.

While our experimental apparatus has yielded valuable and promising results, a retrospective analysis of our experimental configuration and procedure suggests some improvements that should be included in future studies.

- One main area of improvement involves determining the actual spectrometer spectral efficiency and instrument function. Accounting for these parameters will allow the proper calculation of the Raman scattering intensities and bandwidths as well as increase the accuracy of our spectra vibrational assignments.
- Another consideration, addressed in Section 3.2.2 of Chapter 3, is the coupling of the scattered signal light into the spectrometer system. Presently, a viable solution to the coupling is unclear. To utilize focused excitation light, the sample material needs to be circulated or cooled to avoid excess heating due to the high pulse energy density.
- Measurement of the scattering depolarization ratios should be performed. The depolarization ratios will assist in the vibrational assignments and calculation of the spectral intensities and complete a material's set of Raman scattering data.
- Utilizing a tighter bandwidth excitation source will yield an improvement in the precision of the sample spectra compared to the current system. Also a narrower bandwidth will increase the tuning resolution. Finer tuning resolution will allow more detailed study of absorption peak regions. The current system has a tuning resolution limit of approximately $0.1\,nm$ using a Type I phase matching scheme for the OPO UV source. Moving to a Type II phase matching scheme could improve the tuning resolution ten-fold.

Bibliography

A. C. Albrecht. On the theory of Raman intensities. *J. Chem. Phys.*, 34(5):1476–1484, May 1961.

A. Anderson, editor. *The Raman Effect: In Two Volumes*, volume Voulme 1: Principles. Marcel Dekker, Inc., New York, 1971.

Andor. *iXon^{EM} DU-897 (back illuminated) Camera Technical Specifications*. Andor Technology, February 2008. URL `http://www.andor.com`.

W. R. Angus, C. K. Ingold, and A. H. Leckie. 213. Structure of benzene. part III. Raman spectra of liquid benzene and liquid hexadeuterobenzene. *J. Chem. Soc.*, pages 925–931, 1936. doi: 10.1039/JR9360000925.

API. Selected Ultraviolet Spectral Data (American Petroleum Institute Research Project 44). Technical report, Thermodynamics Research Center, Department of Chemistry, Texas A & M University, College Station, Texas, October 1970.

S. A. Asher. Ultraviolet resonance Raman spectrometry for detection and speciation of trace polycyclic aromatic hydrocarbons. *Analytical Chemistry*, 56(4):720–724, 1984.

S. A. Asher. UV resonance Raman spectroscopy for analytical, physical, and biophysical chemistry part 1. *Anal. Chem.*, 65(2):59–66, January 1993a.

S. A. Asher. UV resonance Raman spectroscopy for analytical, physical, and biophysical chemistry part 2. *Anal. Chem.*, 65(4):201–210, February 1993b.

S. A. Asher and C. R. Johnson. Raman spectroscopy of a coal liquid shows that fluorescence interference is minimized with ultraviolet excitation. *Science*, 225(4659):311–313, July 1984. doi: 10.1126/science.6740313.

S. A. Asher and C. R. Johnson. UV resonance Raman excitation profile through the $^1B_{2u}$ state of benzene. *Journal of Physical Chemistry*, 89(8):1375–1379, 1985.

S. A. Asher, C. R. Johnson, and J. Murtaugh. Development of a new UV resonance Raman spectrometer for the 217–400-nm spectral region. *Review of Scientific Instruments*, 54 (12):1657–1662, 1983. doi: 10.1063/1.1137305. URL http://link.aip.org/link/?RSI/54/1657/1.

E. J. Ayars, C. L. Jahncke, M. A. Paesler, and H. D. Hallen. Fundamental differences between micro- and nano-Raman spectroscopy. *Journal of Microscopy*, 202(1):142–147, April 2001.

J. Belyea, C. M. Belyea, S. Lappi, and S. Franzen. Resonance Raman study of ferric heme adducts of dehaloperoxidase from *amphitrite ornata*. *Biochemistry*, 45(48):14275–14284, December 2006. doi: 10.1021/bi0609218.

J. M. Benevides, S. A. Overman, and G. J. T. Jr. Raman, polarized Raman and ultraviolet resonance Raman spectroscopy of nucleic acids and their complexes. *J. Raman Spectrosc.*, 36(4):279–299, April 2005. doi: doi:10.1002/jrs.1321.

J. E. Bertie and C. D. Keefe. Infrared intensities of liquids XXIV: optical constants of liquid benzene-h_6 at 25° C extended to 11.5 cm^{-1} and molar polarizabilities and integrated intensities of benzene-h_6 between 6200 and 11.5 cm^{-1}. *Journal of Molecular Structure*, 695–696:39–57, June 2004. URL http://www.sciencedirect.com/science/article/B6TGS-4CDYG0K-2/2/2781bacd76eaf10af23c5ab329312891.

J. E. Bertie, Y. Apelblat, and C. D. Keefe. Infrared intensities of liquids xxv: Dielectric constants, molar polarizabilities and integrated intensities of liquid toluene at 25° between 4800 and 400 cm^{-1}. *Journal of Molecular Structure*, 750(1–3):78–93, August 2005. URL http://www.sciencedirect.com/science/article/B6TGS-4GD4SWT-1/2/f845eb1fb1a981f18003bcbc561134ee.

P. R. Bevington and D. K. Robinson. *Data Reduction and Error Analysis for the Physical Sciences*. McGraw-Hill Companies, Inc., Boston, Massachusetts, 2nd edition, 1992.

A. Blanco, L. C. P.-L. no, A. J. P. na Quevedo, and S. P. Hernández-Rivera. UV Raman

detection of 2,4-DNT in contact with sand particles. volume 6217, page 621737. SPIE, 2006. doi: 10.1117/12.666281. URL http://link.aip.org/link/?PSI/6217/621737/1.

M. Born and E. Wolf. *Principles of Optics: Electromagnetic theory of propagation, interference, and diffraction of light*. Pergamon Press, Oxford, 6th edition, 1980.

R. W. Boyd. *Nonlinear Optics*. Academic Press, Inc., San Diego, 1992.

W. R. Browne and J. J. McGarvey. The Raman effect and its application to electronic spectroscopies in metal-centered species: Techniques and investigations in ground and excited states. *Coordination Chemistry Reviews*, 251(3–4):454–473, February 2007. doi: doi:10.1016/j.ccr.2006.04.019.

K.-T. Byun and H.-Y. Kwak. A model of laser-induced cavitation. *Jpn. J. Appl. Phys., Part 1*, 43(2):621–630, February 2004. doi: 10.1143/JJAP.43.621. URL http://jjap.ipap.jp/link?JJAP/43/621/.

J. M. Calleja, J. Kuhl, and M. Cardona. Resonant raman scattering in diamond. *Phys. Rev. B*, 17(2):876–883, Jan 1978. doi: 10.1103/PhysRevB.17.876.

J. H. Callomon, T. M. Dunn, and I. M. Mills. Rotational analysis of the 2600 å absorption system of benzene. *Philos. Trans. Roy. Soc.*, 259:499–532, May 1966.

J. Chaves. *Introduction to Nonimaging Optics (Optical Science and Engineering)*. CRC Press, 2008. ISBN 1420054295.

C. G. Chen and A. J. S. III. Revisiting Raman LIDAR: application of new techniques to improve system performance. volume 2833, pages 182–192. SPIE, 1996. doi: 10.1117/12.258154. URL http://link.aip.org/link/?PSI/2833/182/1.

C. G. Chen, D. L. Heglund, M. D. Ray, D. Harder, R. Dobert, K. P. Leung, M. T. Wu, and A. J. S. III. Application of resonance Raman LIDAR for chemical species identification. volume 3065, pages 279–285. SPIE, 1997. doi: 10.1117/12.281019. URL http://link.aip.org/link/?PSI/3065/279/1.

R. J. H. Clark and T. J. Dines. Resonance Raman spectroscopy, and its applications to inorganic chemistry. *Angew. Chem. Int. Ed. Engl.*, 25(2):131–158, February 1986.

F. F. Cleveland and P. Porcelli. Raman spectra of hydrocarbons. v. n-hexane, n-heptane, 2-methylpentane, 3-methylpentane, 2,4-dimethylpentane, and 2,3-dimethylbutane. *The Journal of Chemical Physics*, 18(11):1459–1461, 1950. doi: 10.1063/1.1747513. URL http://link.aip.org/link/?JCP/18/1459/1.

T. M. Cotter, M. E. Thomas, and W. J. Tropf. *Handbook of Optical Constants of Solids II*. Academic Press, Inc., Orlando, Florida, 1991.

M. Dietzel and D. Poulikakos. On vapor bubble formation around heated nanoparticles in liquids. *International Journal of Heat and Mass Transfer*, 50(11-12): 2246–2259, 2007. ISSN 0017-9310. doi: DOI:10.1016/j.ijheatmasstransfer.2006.10.035. URL http://www.sciencedirect.com/science/article/B6V3H-4MR1K8D-3/2/906f58b27d4633e75c1226f34edb3766.

V. G. Dmitriev, G. G. Gurzadyan, and D. N. Nikogosyan. *Handbook of Nonlinear Optical Crystals*. Springer-Verlag, Berlin, 3rd edition, 1999.

F. R. Dollish, W. G. Fateley, and F. F. Bentley. *Characteristic Raman Frequencies of Organic Compounds*. John Wiley & Sons Ltd., New York, 1974.

J. M. Dudik, C. R. Johnson, and S. A. Asher. UV resonance Raman studies of acetone, acetamide, and N-methylacetamide: models for the peptide bond. *Journal of Physical Chemistry*, 89(18):3805–3814, 1985.

D. F. Edwards and H. R. Philipp. *Handbook of Optical Constants of Solids*. Academic Press, Inc., Orlando, Florida, 1985.

E. V. Efremov, F. Ariese, and C. Gooijer. Achievements in resonance Raman spectroscopy: Review of a technique with a distinct analytical chemistry potential. *Analytica Chimica Acta*, 606(2):119–134, January 2008. doi: 10.1016/j.aca.2007.11.006. URL http://www.sciencedirect.com/science/article/B6TF4-4R3C085-7/1/407fad8ef0c7eaa36a55335400867a2c.

A. M. Ellis, M. Feher, and T. G. Wright. *Electronic and Photoelectron Spectroscopy: Fundamentals and Case Studies*. Cambridge University Press, United Kingdom, 2005.

A. Esposito, C. Foster, R. Beckman, and P. Reid. Excited-state dynamics of chlorine dioxide in the condensed phase from resonance Raman intensities. *Journal of Physical Chemistry*

A, 101(29):5309–5319, 1997. URL http://pubs3.acs.org/acs/journals/doilookup?in_doi=10.1021/jp9637035.

T. Etzkorn, B. Klotz, S. Sørensen, I. V. Patroescu, I. Barnes, K. H. Becker, and U. Platt. Gas-phase absorption cross sections of 24 monocyclic aromatic hydrocarbons in the UV and IR spectral ranges. *Atmos. Environ.*, 33:525–540, 1999.

M. P. Felix and A. T. Ellis. Laser-induced liquid breakdown-a step-by-step account. *Applied Physics Letters*, 19(11):484–486, 1971. doi: 10.1063/1.1653783. URL http://link.aip.org/link/?APL/19/484/1.

G. R. Fowles. *Introduction to Modern Optics*. Dover Publications, Inc., New York, 2nd edition, 1968.

F. Galluzzi. Weak vibronic coupling in resonance Raman scattering: a unifying approach. *Il Nuovo Cimento D*, 5(1):100–110, 1985.

W. George and H. Willis, editors. *Computer Methods in UV, Visible, and IR Spectroscopy*. The Royal Society of Chemistry, Cambridge, 1990.

D. P. Gerrity, L. D. Ziegler, P. B. Kelly, R. A. Desiderio, and B. Hudson. Ultraviolet resonance Raman spectroscopy of benzene vapor with 220–184 nm excitation. *The Journal of Chemical Physics*, 83(7):3209–3213, 1985. doi: 10.1063/1.449178. URL http://link.aip.org/link/?JCP/83/3209/1.

J. G. Grasselli, M. K. Snavely, and B. J. Bulkin. *Chemical applications of Raman spectroscopy*. John Wiley & Sons, Inc., New York, 1981.

D. J. Griffiths. *Introduction to Electrodymanics*. Prentice-Hall, Inc., New Jersey, 2nd edition, 1989.

M. Grimsditch, M. Cardona, J. M. Calleja, and F. Meseguer. Resonance in the Raman scattering of CaF_2, SrF_2, BaF_2 and diamond. *Journal of Raman Spectroscopy*, 10(1): 77–81, January 1981.

H. Gross, editor. *Handbook of Optical Systems*, volume 1: Fundamentals of Technical Optics. Wiley-VCH Verlag GmbH & Co. KGaA, Weinheim, Germany, 2005.

J. Grun, C. Manka, S. Nikitin, D. Zabetakis, G. Comanescu, D. Gillis, and J. Bowles. Identification of bacteria from two-dimensional resonant-Raman spectra. *Analytical Chemistry*, 79(14):5489–5493, 2007.

D. T. Haar. The vibrational levels of an anharmonic oscillator. *Phys. Rev.*, 70(3-4):222–223, Aug 1946.

H. D. Hallen, E. J. Ayars, and C. L. Jahncke. The effects of probe boundary conditions and propagation on nano-Raman spectroscopy. *Journal of Microscopy*, 210(3):252–254, June 2003. doi: 10.1046/j.1365-2818.2003.01138.x. URL 10.1046/j.1365-2818.2003.01138.x.

G. Hass and J. E. Waylonis. Optical constants and reflectance and transmittance of evaporated aluminum in the visible and ultraviolet. *J. Opt. Soc. Am.*, 51(7):719–722, July 1961.

E. Hecht. *Optics*. Addison Wesley Longman, Inc., Reading, Massachusetts, 4th edition, 2002.

G. Herzberg. *Molecular Spectra and Molecular Structure*, volume II. Infrared and Raman Spectra of Polyatomic Molecules. D. Van Nostrand Company, Inc., Princeton, New Jersey, 9th edition, 1960.

G. Herzberg. *Molecular Spectra and Molecular Structure*, volume III. Electronic Spectra and Electronic Structure of Polyatomic Molecules. D. Van Nostrand Company, Inc., Princeton, New Jersey, 1966.

A. Y. Hirakawa and M. Tsuboi. Molecular geometry in an excited electronic state and a preresonance Raman effect. *Science*, 188(4186):359–361, April 1975. doi: 10.1126/science.188.4186.359.

S. H. Huerth, M. P. Taylor, H. D. Hallen, and B. H. Moeckly. Electromigration in $YBa_2Cu_3O_7 - \delta$ using a metal clad near-field scanning optical microscope probe. *Applied Physics Letters*, 77(14):2127–2129, 2000. doi: 10.1063/1.1314296. URL http://link.aip.org/link/?APL/77/2127/1.

H. Inaba. *Laser Monitoring of the Atmosphere*, volume 14 of *Topics In applied physics*. Springer-Verlag, New York, 1976.

T. Inagaki. Absorption spectra of pure liquid benzene in the ultraviolet region. *The Journal of Chemical Physics*, 57(6):2526–2530, 1972. doi: 10.1063/1.1678619. URL http://link.aip.org/link/?JCP/57/2526/1.

C. Jahncke and H. Hallen. Near-field raman spectra: surface enhancement, z-polarization, fiber raman background and rayleigh scattering. *Lasers and Electro-Optics Society Annual Meeting, 1996. LEOS 96., IEEE*, 1:176–177, Nov 1996. doi: 10.1109/LEOS.1996.565182.

C. L. Jahncke, M. A. Paesler, and H. D. Hallen. Raman imaging with near-field scanning optical microscopy. *Applied Physics Letters*, 67(17):2483–2485, 1995. doi: 10.1063/1.114615. URL http://link.aip.org/link/?APL/67/2483/1.

C. L. Jahncke, H. D. Hallen, and M. A. Paesler. Nano-Raman spectroscopy and imaging with a near-field scanning optical microscope. *Journal of Raman Spectroscopy*, 27(8):579–586, August 1996.

C. L. Jahncke, S. H. Huerth, B. C. III, and H. D. Hallen. Dynamics of the tip–sample interaction in near-field scanning optical microscopy and the implications for shear force as an accurate distance measure. *Applied Physics Letters*, 81(21):4055–4057, 2002. doi: 10.1063/1.1520711. URL http://link.aip.org/link/?APL/81/4055/1.

R. M. Jarvis and R. Goodacre. Ultra-violet resonance Raman spectroscopy for the rapid discrimination of urinary tract infection bacteria. *FEMS Microbiology Letters*, 232(2):127–132, March 2004. doi: 10.1016/S0378-1097(04)00040-0.

I. Johansson, M. Norrefeldt, A. Pettersson, S. Wallin, and H. Östmark. *Detection of Liquid Explosives and Flammable Agents in Connection with Terrorism*, chapter Close-Range and Standoff Detection and Identification of Liquid Explosives by Means of Raman Spectroscopy, pages 143–153. Springer Netherlands, 2008. doi: 10.1007/978-1-4020-8466-9_14. URL http://www.springerlink.com/content/x37816x6m24638n2.

K. C. Johnson. Coupled scalar wave diffraction theory. *Applied Physics*, 24:249–260, October 1981.

C. M. Jones, T. A. Naim, M. Ludwig, J. Murtaugh, P. L. Flaugh, J. M. Dudik, C. R. Johnson, and S. A. Asher. Analytical applications of ultraviolet resonance Raman spectroscopy. *Trends in Analytical Chemistry*, 4(3):75–80, March 1985. doi: 10.

1016/0165-9936(85)87089-8. URL http://www.sciencedirect.com/science/article/B6V5H-44FNBM1-MR/1/2676fb827bc68c332ae7a0ac6e72518f.

W. Kaiser and W. L. Bond. Nitrogen, a major impurity in common Type-I diamond. *Phys. Rev.*, 115(4):857–863, Aug 1959. doi: 10.1103/PhysRev.115.857.

R. Katoh, H. Yokoi, S. Usuba, Y. Kakudate, and S. Fujiwara. Excitation density effect on the decomposition of liquid benzene by arf excimer laser (193 nm) irradiation. *Chemical Physics Letters*, 291(3–4):305–310, 1998. ISSN 0009-2614. doi: DOI:10.1016/S0009-2614(98)00625-3. URL http://www.sciencedirect.com/science/article/B6TFN-3VW73FX-8/2/df8bd66198f6dc70f857bb04e6d4cc1e.

G. Kavitha and C. Narayana. Raman scattering studies on n-heptane under high pressure. *The Journal of Physical Chemistry B*, 110(17):8777–8781, 2006. doi: 10.1021/jp056176a. URL http://pubs.acs.org/doi/abs/10.1021/jp056176a.

C. D. Keefe and J. E. Bertie. Liquid-phase force field and dipole moment derivatives with respect to internal coordinates of benzene. *Spectrochimica Acta Part A: Molecular and Biomolecular Spectroscopy*, 65(3–4):638–649, November 2006. URL http://www.sciencedirect.com/science/article/B6VNG-4JF997C-D/2/608ef0a02ca68d8a14342b376d87d3a6.

C. D. Keefe and J. L. MacDonald. Vibrational assignment integrated intensities of liquid toluene-d8 from 4000 and 450 cm^{-1} at 25° c. *Spectrochimica Acta Part A: Molecular and Biomolecular Spectroscopy*, 64(2):483–494, May 2006. URL http://www.sciencedirect.com/science/article/B6VNG-4HX47S7-6/2/5c9ca616bd53cc1023a60fca03924bf1.

C. D. Keefe, J. K. Pearson, and A. MacDonald. Optical constants and vibrational assignment of liquid toluene-d_8 between 4000 and 450 cm^{-1} at 25° C. *Journal of Molecular Structure*, 655(1):69–80, July 2003. URL http://www.sciencedirect.com/science/article/B6TGS-48N2WPF-1/2/dc4b75ab0228c500648d814f16da1651.

L. E. Kinsler, A. R. Frey, A. B. Coppens, and J. V. Sanders. *Fundamentals of Acoustics*. John Wiley & Sons Ltd., New York, 4th edition, 2000.

D. S. Knight and W. B. White. Characterization of diamond films by Raman spectroscopy. *Journal of Materials Research*, 4(2):385–393, March–April 1989. doi: 10.1557/JMR.1989.0385.

A. Kudelski. Analytical applications of Raman spectroscopy. *Talanta*, 76(1):1–8, February 2008. doi: 10.1016/j.talanta.2008.02.042. URL http://www.sciencedirect.com/science/article/B6THP-4S0JMX1-2/1/d57d6f4d7a4249f21c9b5d97a8fb139d.

K. J. Kuhn. *Laser Engineering*. Prentice-Hall, Inc., Upper Saddle River, New Jersey, 1998.

R. J. Lacey, I. P. Hayward, H. S. Sands, and D. N. Batchelder. Characterization and identification of contraband using UV resonant Raman spectroscopy. volume 2937, pages 100–105. SPIE, 1997. doi: 10.1117/12.266763. URL http://link.aip.org/link/?PSI/2937/100/1.

L. Láng, editor. *Absorption Spectra in the Ultraviolet and Visible Region*, volume I. Academic Press, Inc., New York, 1961.

L. Láng, editor. *Absorption Spectra in the Ultraviolet and Visible Region*, volume XIV. Academic Press, Inc., New York, 1970.

S.-Y. Lee. Placzek-type polarizability tensors for Raman and resonance Raman scattering. *J. Chem. Phys.*, 78(2):723–734, January 1983.

S. M. Leeds, T. J. Davis, P. W. May, C. D. O. Pickard, and M. N. R. Ashfold. Use of different excitation wavelengths for the analysis of CVD diamond by laser Raman spectroscopy. *Diamond and Related Materials*, 7(2-5):233–237, 1998. ISSN 0925-9635. doi: 10.1016/S0925-9635(97)00261-6. URL http://www.sciencedirect.com/science/article/B6TWV-3SYPJ2F-1C/2/bf0d03b8ebfbdde56899820c9a291b7b.

L. Li. Multilayer modal method for diffraction gratings of arbitrary profile, depth, and permittivity. *J. Opt. Soc. Am. A*, 10(12):2581–2591, December 1993.

L. Li. Use of Fourier series in the analysis of discontinuous periodic structures. *J. Opt. Soc. Am. A*, 13(9):1870–1876, September 1996.

L. Li, J. Chandezon, G. Granet, and J.-P. Plumey. Rigorous and efficient grating-analysis method made easy for optical engineers. *Appl. Opt.*, 38(2):304–313, January 1999.

D. R. Lide, editor. *CRC Handbook of Chemistry and Physics, 89th Edition (Internet Version 2008)*. CRC Press/Taylor and Francis, 89th edition, 2008. URL `http://www.hbcpnetbase.com/`.

M. A. Linne. *Spectroscopic Measurement: An Introduction to the Fundamentals*. Academic Press, Inc., London, 2002.

E. G. Loewen and E. Popov. *Diffraction Gratings and Applications*. Marcel Dekker, Inc., New York, 1997.

D. A. Long. *Raman Spectroscopy*. McGraw-Hill Book Company, Inc., Great Britian, 1977.

D. A. Long. *The Raman Effect: A unified treatment of the theory of Raman scattering by molecules*. John Wiley & Sons Ltd., West Sussex, 2002.

J. Maindonald and W. J. Braun. *Data Analysis and Graphics Using R: An example-based approach*. Cambridge University Press, Cambridge, 2nd edition, 2003.

M. Margelevičius, V. Grigaliūnas, H. Pranevičius, and J. Margelevičius. Modelling of relief of phase reflection diffraction grating. *Appl. Math. Modelling*, 27:1035–1049, 2003.

R. M. Measures. *Laser Remote Sensing: Fundamentals and applications*. John Wiley & Sons, Inc., New York, 1984.

D. H. Menzel, editor. *Fundamental Formulas of Physics*, volume One. Dover Publications, Inc., New York, 1960a.

D. H. Menzel, editor. *Fundamental Formulas of Physics*, volume Two. Dover Publications, Inc., New York, 1960b.

J. R. Meyer-Arendt. *Introduction To Classical & Modern Optics*. Prentice-Hall, Inc., New Jersey, 3rd edition, 1989.

M. G. Moharam, D. A. Pommet, E. B. Grann, and T. K. Gaylord. Stable implementation of the rigorous coupled-wave analysis for surface-relief gratings: enhanced transmittance matrix approach. *J. Opt. Soc. Am. A*, 12(5):1077–1086, May 1995.

J. H. Moore, C. C. Davis, and M. A. Coplan. *Building Scientific Apparatus: A practical guide to design and construction*. Addison-Wesley, Inc., Redwood City, California, 2nd edition, 1989.

Y. Nakata and M. Koshiba. Boundary-element analysis of plane-wave diffraction from groove-type dielectric and metallic gratings. *J. Opt. Soc. Am. A*, 7(8):1494–1502, August 1990.

D. N. Nikogosyan. Beta barium borate (BBO). *Applied Physics A: Materials Science & Processing*, 52(6):359–368, June 1991. doi: 10.1007/BF00323647.

J. Noack and A. Vogel. Laser-induced plasma formation in water at nanosecond to femtosecond time scales: calculation of thresholds, absorption coefficients, and energy density. *IEEE Journal of Quantum Electronics*, 35(8):1156–1167, August 1999. URL http://ieeexplore.ieee.org/search/wrapper.jsp?arnumber=777215.

J. Noack, D. X. Hammer, G. D. Noojin, B. A. Rockwell, and A. Vogel. Influence of pulse duration on mechanical effects after laser-induced breakdown in water. *Journal of Applied Physics*, 83(12):7488–7495, 1998. doi: 10.1063/1.367512. URL http://link.aip.org/link/?JAP/83/7488/1.

S. A. Oladepo and G. R. Loppnow. Ultraviolet resonance Raman spectroscopy as a robust spectroscopic tool for *in situ* sunscreen analysis. *Analytica Chimica Acta*, 2008. doi: doi:10.1016/j.aca.2008.08.031.

H.-H. Perkampus. *UV-VIS Atlas of Organic Compounds*. Number 2. VCH, Weinheim, 2nd edition, 1992.

R Development Core Team. *R: A Language and Environment for Statistical Computing*. R Foundation for Statistical Computing, Vienna, Austria, 2008. URL http://www.R-project.org. ISBN 3-900051-07-0.

W. F. Radle and C. A. Beck. An experimental study of the near ultraviolet absorption spectrum of benzene. *The Journal of Chemical Physics*, 8(7):507–513, 1940. doi: 10.1063/1.1750702. URL http://link.aip.org/link/?JCP/8/507/1.

L. J. Radziemski. Calculation of dispersion for a plane grating in a Czerny-Turner mount: a comment. *Appl. Opt.*, 20(11):1948–1950, June 1981.

C. V. Raman. The diamond. *Proc. Indian Acad. Sci. A*, 44:99–110, September 1956.

C. V. Raman and K. S. Krishnan. A new type of secondary radiation. *Nature*, 121:501–502, March 1928. doi: 10.1038/121501c0.

L. Rayleigh. On the light from the sky, its polarization and color. *Philosophical Magazine*, 41:447–454, 1871.

D. G. Rea. On the theory of the resonance Raman effect. *J. Mol. Spectrosc.*, 4:499–506, 1960.

H. Rosen, P. Robrish, and O. Chamberlain. Remote detection of pollutants using resonance Raman scattering. *Appl. Opt.*, 14(11):2703–2706, 1975. URL `http://www.opticsinfobase.org/abstract.cfm?URI=ao-14-11-2703`.

A.-M. Saariaho, D. S. Argyropoulos, A.-S. Jääskeläinen, and T. Vuorinen. Development of the partial least squares models for the interpretation of the UV resonance Raman spectra of lignin model compounds. *Vibrational Spectroscopy*, 37(1):111–121, January 2005. doi: 10.1016/j.vibspec.2004.08.001.

J. J. Sakurai. *Modern Quantum Mechanics*. Addison Wesley Longman, Inc., Reading, Massachusetts, revised edition, 1994.

M. R. Salehpour and S. Satpathy. Comparison of electron bands of hexagonal and cubic diamond. *Phys. Rev. B*, 41(5):3048–3052, Feb 1990. doi: 10.1103/PhysRevB.41.3048.

C. J. Sansonetti and J. Reader. Spectrum and energy levels of singly-ionized mercury (Hg II). *Physica Scripta*, 63:219–242, 2001.

J. E. Sansonetti and W. C. Martin. Handbook of basic atomic spectroscopic data. *J. Phys. Chem. Ref. Data*, 34(4):1559–2259, 2005. doi: 10.1063/1.1800011.

SBIG. *CCD Camera Operating Manual for the Model ST-4X, ST-5 and ST-6*. Santa Barbara Instrument Group, 1482 East Valley Road Santa Barbara, CA 93108, January 1996.

A. J. Sedlacek, D. Harder, K. P. Leung, P. B. Z. Jr., D. Burr, and C. L. Chen. Remote sensing of the atmosphere by resonance Raman LIDAR. Upton, New York, December 1994. Brookhaven National Laboratory, Optical Society of America. BNL–61283.

A. J. Sedlacek, III, and C. Finfrock. UV Raman spectral signature acquisition: UV Raman spectal fingerprints. Yearend Report BNL-69453, Brookhaven National Laboratory, Upton, New York, September 2001. Submitted to Edgewood Chemical Biological Center.

W. Siebrand and M. Z. Zgierski. Effect of solvent-induced line broadening on resonance Raman excitation profiles and depolarization ratios. *Journal of Physical Chemistry*, 86 (24):4718–4725, 1982.

D. Y. Smith, E. Shiles, and M. Inokuti. *Handbook of Optical Constants of Solids*. Academic Press, Inc., Orlando, Florida, 1985.

E. Smith and G. Dent. *Modern Raman Spectroscopy: A practical approach*. John Wiley & Sons, Ltd., West Sussex, 2005.

Quanta-Ray INDI Pulsed Nd:YAG Laser User's Manual. Spectra-Physics Lasers, Inc., 5 edition, June 1998.

Spex. *Instructions 1877 Triplemate*. Spex Industries, Inc., 1985.

Spex. *Spectral Efficiency Curve 530-25*. Jobin Yvon Horiba, June 1999. 1200 gr/mm, unpolarized.

Spex. *Spectal Efficiency Curve 530-13*. Jobin Yvon Horiba, June 2000. 2400 gr/mm, TE, TM, unpolarized.

T. G. Spiro and T. C. Strekas. Resonance Raman spectra of heme proteins. effects of oxidation and spin state. *J. Am. Chem. Soc.*, 96(2):338–345, January 1974. doi: 10.1021/ja00809a004.

K. S. Stowe. *Introduction to Statistical Mechanics and Thermodynamics*. John Wiley & Sons Ltd., New York, 1984.

S. Sugden. The determination of surface tension from the maximum pressure in bubbles part I. *J. Chem. Soc., Trans.*, 121:858–866, 1922. doi: 10.1039/CT9222100858.

S. Sugden. The variation of surface tension with temperature and some related functions. *J. Chem. Soc., Trans.*, 125:32–41, 1924a.

S. Sugden. The determination of surface tension from the maximum pressure in bubbles part II. *J. Chem. Soc., Trans.*, 125:27–31, 1924b. doi: 10.1039/CT9242500027.

R. L. Sutherland. *Handbook of Nonlinear Optics*. Marcel Dekker, Inc., New York, 2nd edition, 2003.

J. Szczepanski, J. Fuller, S. Ekern, and M. Vala. Electronic absorption and resonance Raman spectra of large linear carbon clusters isolated in solid argon. *Spectrochimica Acta Part A*, 57(4):775–786, March 2001. doi: 10.1016/S1386-1425(00)00443-1.

R. Toriumi, H. Tai, H. Kuze, and N. Takeuchi. Tunable solid state uv lidar system for no monitoring. volume 2833, pages 62–69. SPIE, 1996. doi: 10.1117/12.258141. URL http://link.aip.org/link/?PSI/2833/62/1.

A. Toyama, M. Hamuara, and H. Takeuchi. Correlation between vibrational frequencies and hydrogen bonding states of the guanine ring studied by UV resonance Raman spectroscopy of 2'-deoxy-3',5'-bis(triisopropylsilyl)guanosine dissolved in various solvents. *Journal of Molecular Structure*, 379(1-3):99–108, June 1996. doi: 10.1016/0022-2860(95)09159-9.

A. Toyama, K. Ohta, and H. Takeuchi. Correlation between the UV resonance Raman intensity and hydrogen bonding of the adenine ring. *Journal of Molecular Structure*, 735–736:235–241, November 2005. doi: 10.1016/j.molstruc.2004.11.004.

K. Toyota, S. Nakashima, and T. Okada. Near-infrared laser-induced breakdown of liquid benzene. *Chemical Physics Letters*, 323(3–4):323–328, 2000. ISSN 0009-2614. doi: DOI:10.1016/S0009-2614(00)00532-7. URL http://www.sciencedirect.com/science/article/B6TFN-40GHS59-M/2/10a7fa43381ff807d6e24cbe5f6e1216.

K. Toyota, T. Tanaka, S. ichi Nishiwaki, S. Nakashima, and T. Okada. Analysis of products from breakdown of liquid benzene, toluene and cyclohexane caused by nd3+:yag pulsed laser irradiation. *Journal of Photochemistry and Photobiology A: Chemistry*, 141(1):9–16, 2001. ISSN 1010-6030. doi: DOI:10.1016/S1010-6030(01)00433-6. URL http://www.sciencedirect.com/science/article/B6TGY-435M6W6-2/2/057b664e1e54b9af122ef4e9657b390d.

Y. Tsuboi, K. Hatanaka, H. Fukumura, and H. Masuhara. The 248 nm excimer laser ablation of liquid benzene derivatives: A relation between ablation threshold and molecular photochemical reactivity. *The Journal of Physical Chemistry*, 98(44):11237–11241, 1994. doi: 10.1021/j100095a001. URL http://pubs.acs.org/doi/abs/10.1021/j100095a001.

Operation Manual: OPO BBO-3B + BBO-SHG (Type I, Model S). U-Oplaz Technologies, August 1999.

J. H. Van Vleck. On the vibrational selection principles in the Raman effect. *Proc. Natl. Acad. Sci. U. S. A.*, 15(9):754–764, September 1929.

A. Vogel and W. Lauterborn. Acoustic transient generation by laser-produced cavitation bubbles near solid boundaries. *The Journal of the Acoustical Society of America*, 84(2): 719–731, 1988. doi: 10.1121/1.396852. URL http://link.aip.org/link/?JAS/84/719/1.

A. Vogel, W. Lauterborn, and R. Timm. Optical and acoustic investigations of the dynamics of laser-produced cavitation bubbles near a solid boundary. *Journal of Fluid Mechanics*, 206:299–338, 1989. doi: 10.1017/S0022112089002314. URL http://journals.cambridge.org/action/displayAbstract?fromPage=online&aid=395526&fulltextType=RA&fileId=S0022112089002314.

A. Vogel, S. Busch, and U. Parlitz. Shock wave emission and cavitation bubble generation by picosecond and nanosecond optical breakdown in water. *The Journal of the Acoustical Society of America*, 100(1):148–165, 1996. doi: 10.1121/1.415878. URL http://link.aip.org/link/?JAS/100/148/1.

D. C. Wells, E. W. Greisen, and R. H. Harten. FITS - a Flexible Image Transport System. *Astronomy and Astrophysics Supplement Series*, 44:363–+, June 1981.

R. Widenhorn, L. Mündermann, A. Rest, and E. Bodegom. Meyer–neldel rule for dark current in charge-coupled devices. *Journal of Applied Physics*, 89(12):8179–8182, 2001. doi: 10.1063/1.1372365. URL http://link.aip.org/link/?JAP/89/8179/1.

A. Willitsford, C. T. Chadwick, H. Hallen, and C. R. Philbrick. Resonance Raman measurements utilizing a deep UV source. volume 6950, page 69500A. SPIE, 2008. doi: 10.1117/12.778253. URL http://link.aip.org/link/?PSI/6950/69500A/1.

A. H. Willitsford. *Resonance Raman spectroscopy in the ultraviolet using a tunable optical parametric oscillator*. PhD thesis, Pennsylvania State University, 2008.

E. B. Wilson. A partial interpretation of the Raman and infrared spectra of benzene. *Phys. Rev.*, 46(2):146–147, Jul 1934a. doi: 10.1103/PhysRev.46.146.2.

E. B. Wilson. The normal modes and frequencies of vibration of the regular plane hexagon model of the benzene molecule. *Phys. Rev.*, 45(10):706–714, May 1934b. doi: 10.1103/PhysRev.45.706.

M. Wojdyr. *Fityk 0.8.2 User's Manual*, 2007. URL `http://www.unipress.waw.pl/fityk/`.

Y. Xie and J. E. Boggs. The computed force constants and vibrational spectra of toluene. *Journal of Computational Chemistry*, 7(2):158–164, April 1986. doi: 10.1002/jcc.540070209.

A. Yaman, A. B. Bayrakçeken, O. J. Demir, and F. Bayrakçeken. Electronic absorption and Raman resonance scattering of spectroscopically pure SiO2. *Spectrochimica Acta Part A*, 56(10):1901–1903, September 2000. doi: 10.1016/S1386-1425(00)00247-X.

A. Yariv. *Quantum Electronics*. John Wiley & Sons, Inc., 2nd edition, 1975.

F. R. Young. *Cavitation*. McGraw-Hill Book Company, Inc., Great Britian, 1989.

L. D. Ziegler. Rotational Raman excitation profiles of symmetric tops: Subpicosecond rotation dependent lifetimes in the $\tilde{A}$ state of ammonia. *The Journal of Chemical Physics*, 86(4):1703–1714, 1987. doi: 10.1063/1.452169. URL `http://link.aip.org/link/?JCP/86/1703/1`.

L. D. Ziegler and A. C. Albrecht. Preresonance Raman scattering of overtones: The scattering of two overtones of benzene in the ultraviolet. *J. Raman Spectrosc.*, 8(2):73–80, April 1979.

L. D. Ziegler and B. Hudson. Resonance Raman scattering of benzene and benzene-d_6 with 212.8 nm excitation. *The Journal of Chemical Physics*, 74(2):982–992, 1981.

APPENDICES

Appendix A

Electronics Designs

This appendix contains several of the electronics schematics and printed circuit board (PCB) patterns designed primarily for my previous near-field scanning optical microscopy (NSOM) work. The schematic capture and PCB layout was done utilizing Protel DXP from Altium Limited and represents the first attempt to implement surface-mount components into the NCSU Optics Group's laboratory apparatus. The motivation for these electronics was to measure the very small photocurrent expected on the NSOM probe due to photo-electron emission from a sample. Additionally, during the resonance Raman spectroscopy work, a modified version of these electronics was also utilized in-route to determining appropriate signal detection schemes (subsequently an alternative method was used). Currently, these electronics have been re-implemented into the photocurrent measurement scheme in the original NSOM apparatus. I present these without explanation of their operation. I encourage any interested party to correspond to me via my email (ctchadwick@hotmail.com) for explanation of these electronics' operation and design considerations.

- NSOM probe signal integrator/peak-hold (page 132): the purpose of this circuit is to collect (integrate) the very small expected photocurrent at its input and hold the peak value (now a voltage) for computer acquisition. The peak-hold circuit is reset by a delayed TTL pulse obtained from the current laser pulse responsible for the photocurrent;
- Photodiode discriminator (page 133): the purpose of this circuit is to generate a TTL pulse from the signal output of a photodiode. Some adjustment on the pulse width is

handled by the potentiometer;

- Adjustable digital pulse delay (page 134): the purpose of this circuit is to transform the TTL pulse at its input to another TTL pulse at its output. The output pulse has an adjustable pulse width and an adjustable delay from the leading edge of the input pulse; and
- Bill of materials for these circuit designs (page 135).

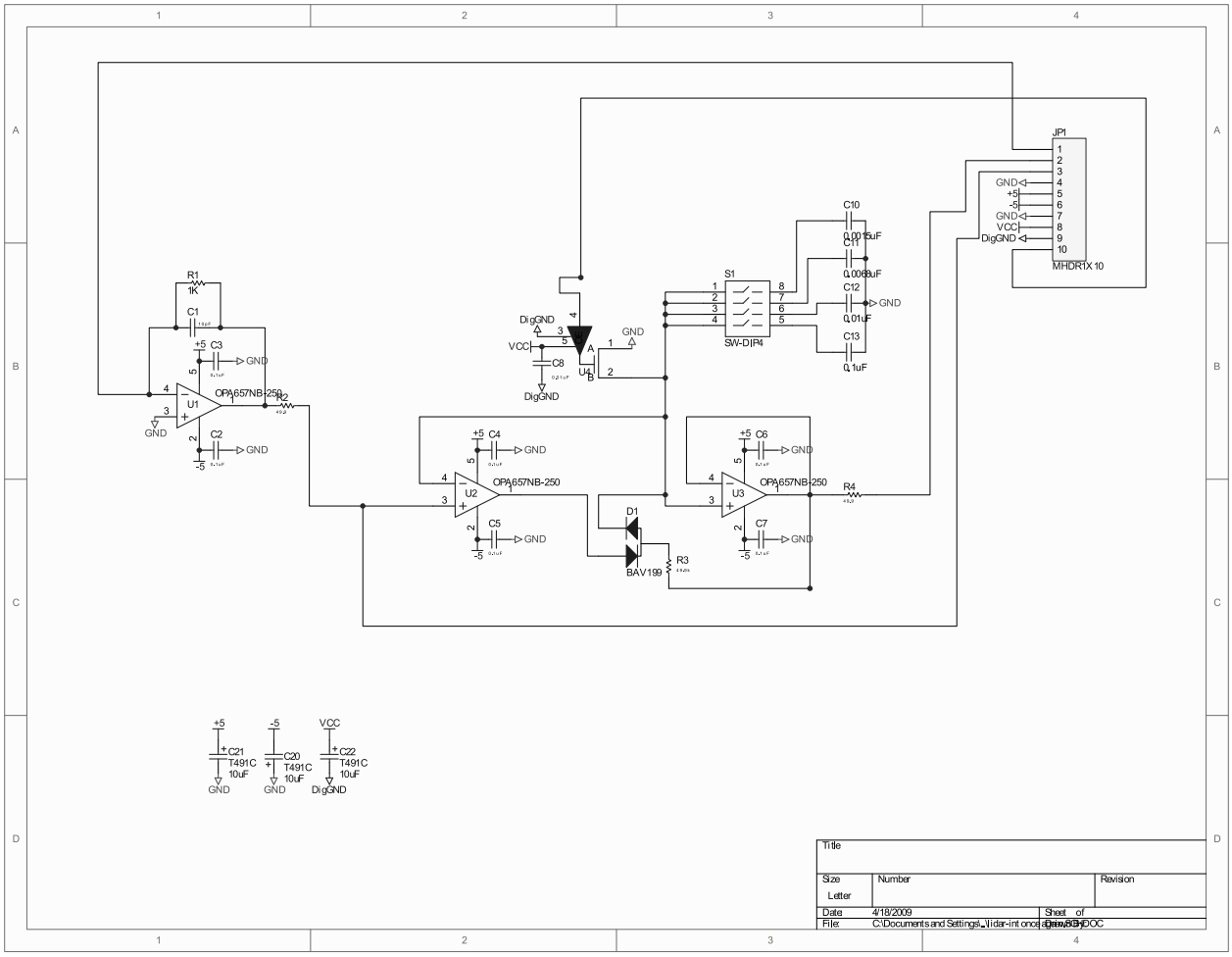
JP1
MHDR1X 10
R1
1K
C1
C2
C3
C4
C5
C6
C7
C8
C10
0.0015uF
C11
0.0068uF
C12
0.01uF
C13
0.1uF
S1
SW-DIP4
U1
U2
U3
U4
OPA657NB-250
R2
R3
R4
D1
BAV199
DigGND
VCC
GND
+5
-5
C21
C20
C22
T491C
10uF
Title
Size
Letter
Number
Revision
Date
4/18/2009
Sheet of
File:
C:\Documents and Settings\...\lidar-int onoc.SchDoc


59.38 (mm)
39.37 (mm)

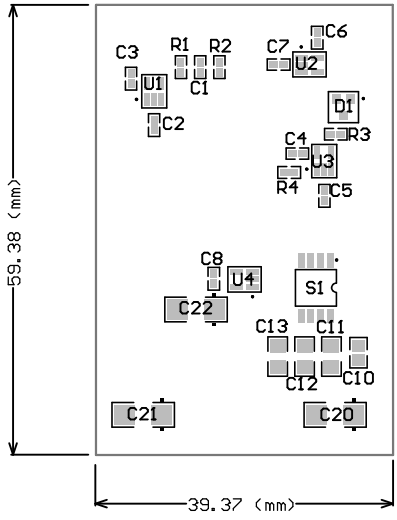
59.38 (mm)
39.37 (mm)
C3
R1
R2
C7
C6
U1
U2
C1
C2
D1
R3
C4
U3
R4
C5
C8
U4
S1
C22
C13
C11
C12
C10
C21
C20

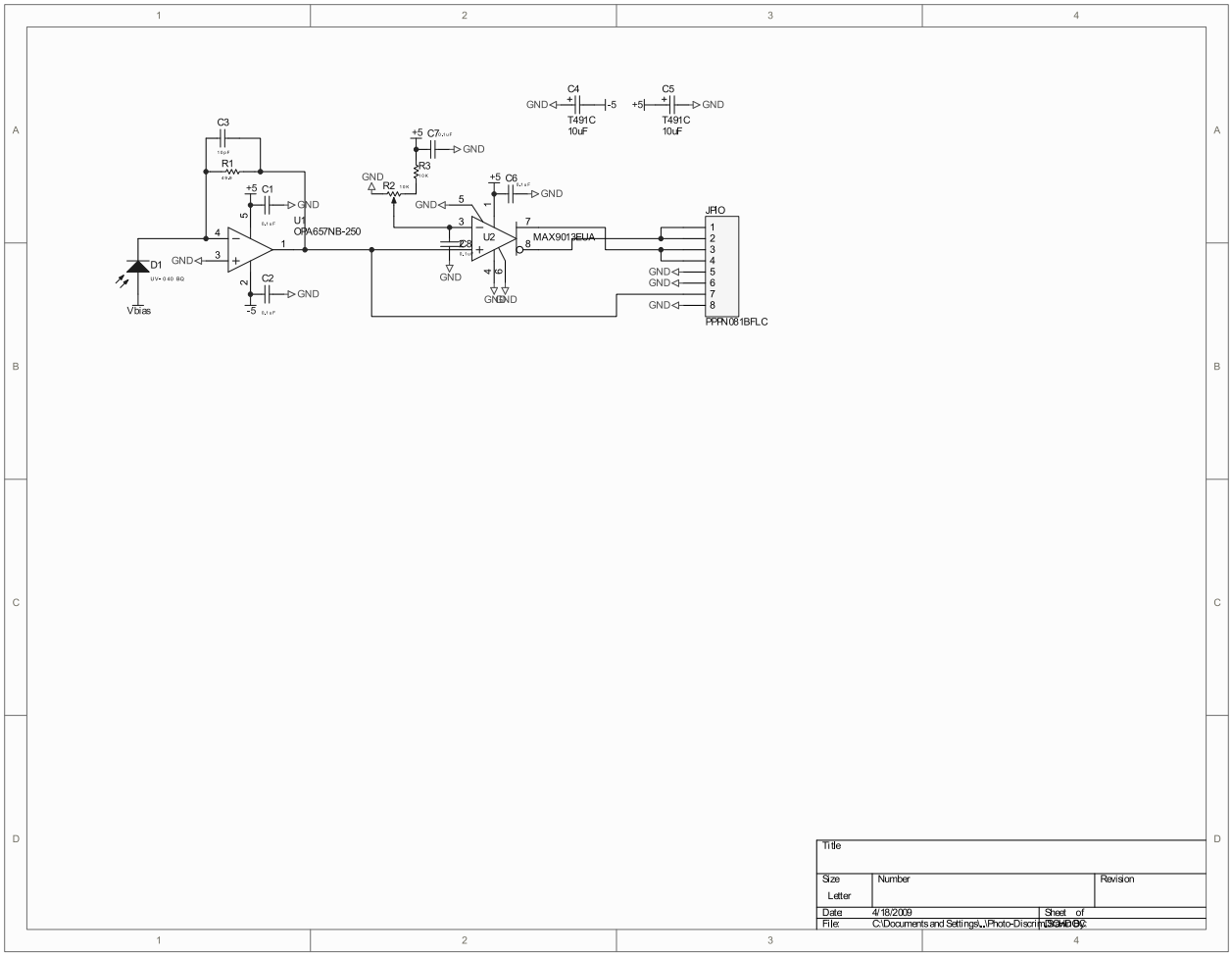
C4
T491C
10uF
C5
T491C
10uF
C3
R1
C1
U1
OPA657NB-250
D1
C2
R3
R2
C7
C6
U2
MAX9012EUA
C8
JP1O
PPPN081BFLC
Vbias
GND
+5
-5
Title
Size
Letter
Number
Revision
Date
4/18/2009
File:
C:\Documents and Settings\...\Photo-Discrimination.SchDoc
Sheet of

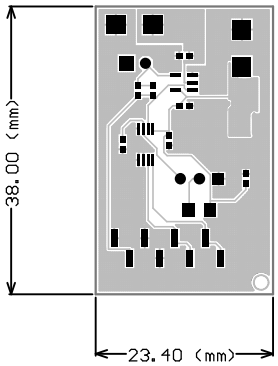
38.00 (mm)
23.40 (mm)

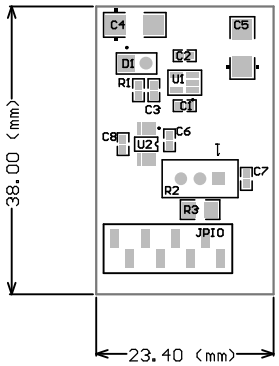
C4
C5
D1
C2
R1
U1
C3
C1
C8
U2
C6
C7
R2
R3
JP1O
38.00 (mm)
23.40 (mm)

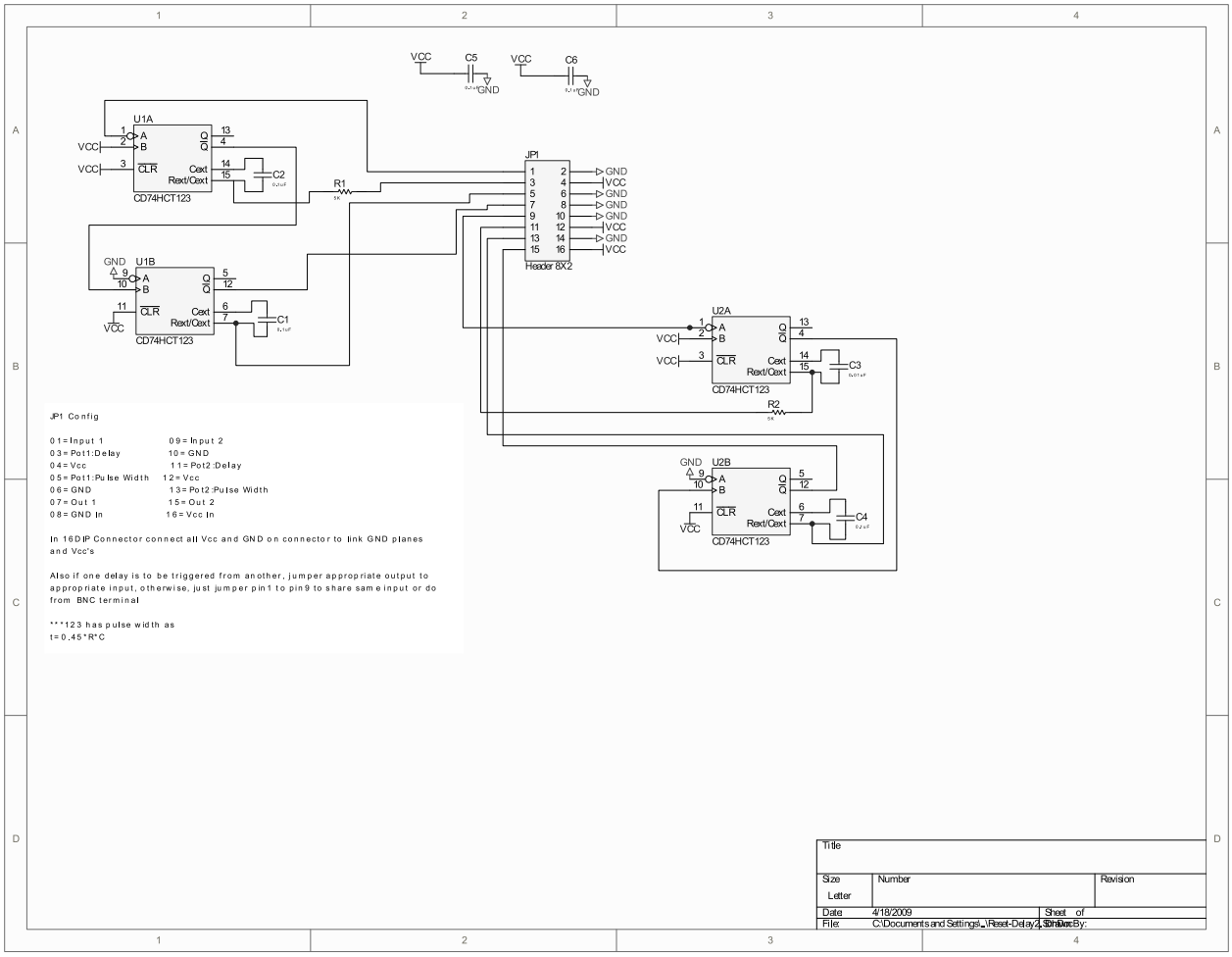
VCC
C5
GND
VCC
C6
GND
U1A
CD74HCT123
R1
JP1
Header 8X2
GND
VCC
U1B
CD74HCT123
C1
U2A
CD74HCT123
C3
R2
U2B
CD74HCT123
C4
JP1 Config
01 = Input 1
03 = Pot1:Delay
04 = Vcc
05 = Pot1:Pulse Width
06 = GND
07 = Out 1
08 = GND In
09 = Input 2
10 = GND
11 = Pot2:Delay
12 = Vcc
13 = Pot2:Pulse Width
15 = Out 2
16 = Vcc In
In 16DIP Connector connect all Vcc and GND on connector to link GND planes and Vcc's
Also if one delay is to be triggered from another, jumper appropriate output to appropriate input, otherwise, just jumper pin1 to pin9 to share same input or do from BNC terminal
***123 has pulse width as
t = 0.45*R*C
Title
Size
Letter
Number
Revision
Date
4/18/2009
File:
C:\Documents and Settings\...\Reset-Delay2.SchDoc
Sheet of
Drawn By:

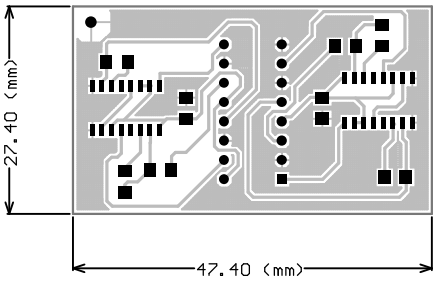
27.40 (mm)
47.40 (mm)

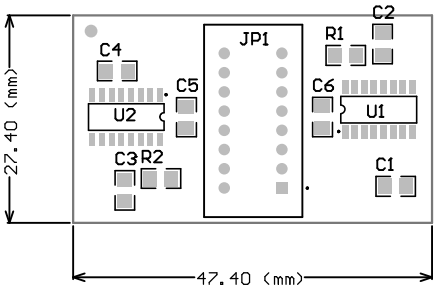
C2
C4
JP1
R1
C5
C6
U2
U1
C3
R2
C1
27.40 (mm)
47.40 (mm)

Table A.1: Electronics bill of materials associated with the three prior schematic and PCB designs.

Designator	Value	Description	Footprint
		NSOM tip signal integrator/pre-amplifier	
C1	10 pF	Non-polarized Capacitor	C1005-0402
C2	0.1 μF	Non-polarized Capacitor	C1005-0402
C3	0.1 μF	Non-polarized Capacitor	C1005-0402
C4	0.1 μF	Non-polarized Capacitor	C1005-0402
C5	0.1 μF	Non-polarized Capacitor	C1005-0402
C6	0.1 μF	Non-polarized Capacitor	C1005-0402
C7	0.1 μF	Non-polarized Capacitor	C1005-0402
C8	0.01 μF	Non-polarized Capacitor	C1005-0402
C10	0.0015 μF	Non-Polarized Capacitor	R2012-0805
C11	0.0068 μF	Non-Polarized Capacitor	C3216-1206
C12	0.01 μF	Non-Polarized Capacitor	C3216-1206
C13	0.1 μF	Non-Polarized Capacitor	C3216-1206
C20	10 μF	Solid Tantalum Chip Capacitor (Polarized)	SO-C2/X2.5
C21	10 μF	Solid Tantalum Chip Capacitor (Polarized)	SO-C2/X2.5
C22	10 μF	Solid Tantalum Chip Capacitor (Polarized)	SO-C2/X2.5
D1	BAV 199	Dual SMD Series Diode	SO-G3/C2.25
JP1	MHDR1X10	Header, 10-Pin	MHDR1X10
R1	1 $k\Omega$	Resistor	C1005-0402
R2	49.9 Ω	Resistor	C1005-0402
R3	49.9 $k\Omega$	Resistor	C1005-0402
R4	49.9 Ω	Resistor	C1005-0402
S1	SW-DIP4	DIP Switch	SO-G8
U1	OPA657NB	Wideband, FET-Input Op-Amp	SO-G5/P.95
U2	OPA657NB	Wideband, FET-Input Op-Amp	SO-G5/P.95
U3	OPA657NB	Wideband, FET-Input Op-Amp	SO-G5/P.95
U4	NC7SZ384	UHS 1 Bit Switch	SO-G5/P.95
		Photodiode discriminator	
C1	0.1 μF	Non-Polarized Capacitor	C1005-0402
C2	0.1 μF	Non-polarized Capacitor	C1005-0402
C3	10 pF	Non-polarized Capacitor	C1005-0402
C4	10 μF	Solid Tantalum Chip Capacitor (Polarized)	SO-C2/X2.5
C5	10 μF	Solid Tantalum Chip Capacitor (Polarized)	SO-C2/X2.5
C6	0.1 μF	Non-polarized Capacitor	C1005-0402
C7	0.1 μF	Non-polarized Capacitor	C1005-0402
C8	0.1 μF	Non-polarized Capacitor	C1005-0402
D1	EGG UV-040 BQ	Photodiode	—
JPIO	PPPN081BFLC	Header, 8-Pin	PPPN081BFLC
R1	49.9 Ω	Resistor	C1005-0402
R2	10 $k\Omega$	Potentiometer	SIP-P3/X1.5
R3	10 $k\Omega$	Resistor	C3216-1206
U1	OPA657NB	Wideband, FET-Input Op-Amp	SO-G5/P.95
U2	MAX9013EUA	Single, Precision TTL comparator	TSSO3X5-G8/X.35
		Adjustable digital pulse delay	
C1	0.1 μF	Non-Polarized Capacitor	C3216-1206
C2	0.1 μF	Non-Polarized Capacitor	C3216-1206
C3	0.01 μF	Non-Polarized Capacitor	C3216-1206
C4	0.1 μF	Non-Polarized Capacitor	C3216-1206
C5	0.1 μF	Non-Polarized Capacitor	C3216-1206
C6	0.1 μF	Non-Polarized Capacitor	C3216-1206
JP1	16 Pin Header	Header, 8-Pin, Dual row	DIP-P16
R1	5 $k\Omega$	Resistor	C3216-1206
R2	5 $k\Omega$	Resistor	C3216-1206
U1	CD74HCT123	Dual Retriggerable Monostable Multivibrator	SO-G16/G6.9
U2	CD74HCT123	Dual Retriggerable Monostable Multivibrator	SO-G16/C5.85

Appendix B

Mechanical Designs

This appendix contains several of my more interesting mechanical designs utilized in the current resonance Raman spectroscopy work and in previous near-field scanning optical microscopy (NSOM) work. These were designed using Pro-Engineer from Parametric Technology Corporation. The machined components of some of these drawings are currently (as of April 24, 2009) being utilized in my previous NSOM apparatus and others are scattered throughout the NSCU Optical Lab in other apparatus and may or may not have additional modifications. I present these without explanation of their operation. I encourage any interested party to correspond to me via my email (ctchadwick@hotmail.com) for explanation of these mechanical components' operation and design considerations.

- Stainless steel vapor cube (page 137),
- PTFE sample holder base (page 138),
- ANDOR to SPEX camera adapter (page 139),
- Aluminum base plate for Faraday box (page 140) with the assistance of Michael Chadwick,
- Copper Faraday box input panel (page 141), and
- Toy motor mounting bracket for vacuum deposition system (page 142).

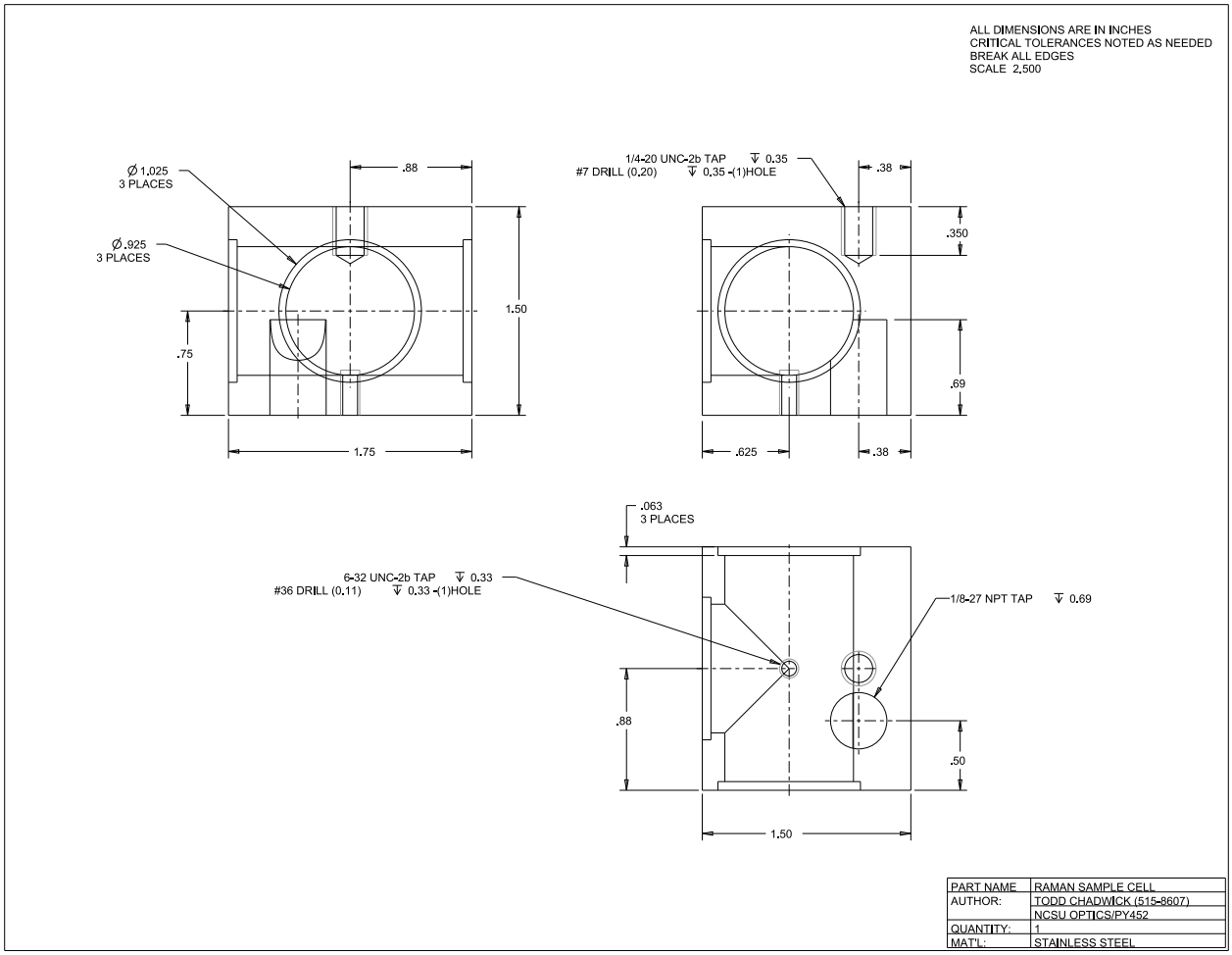
ALL DIMENSIONS ARE IN INCHES
CRITICAL TOLERANCES NOTED AS NEEDED
BREAK ALL EDGES
SCALE 2.500
Ø 1.025
3 PLACES
Ø .925
3 PLACES
.88
1.50
.75
1.75
1/4-20 UNC-2b TAP ↧ 0.35
#7 DRILL (0.20) ↧ 0.35 -(1)HOLE
.38
.350
.69
.625
.38
.063
3 PLACES
6-32 UNC-2b TAP ↧ 0.33
#36 DRILL (0.11) ↧ 0.33 -(1)HOLE
1/8-27 NPT TAP ↧ 0.69
.88
.50
1.50
PART NAME RAMAN SAMPLE CELL
AUTHOR: TODD CHADWICK (515-8607)
NCSU OPTICS/PY452
QUANTITY: 1
MAT'L: STAINLESS STEEL

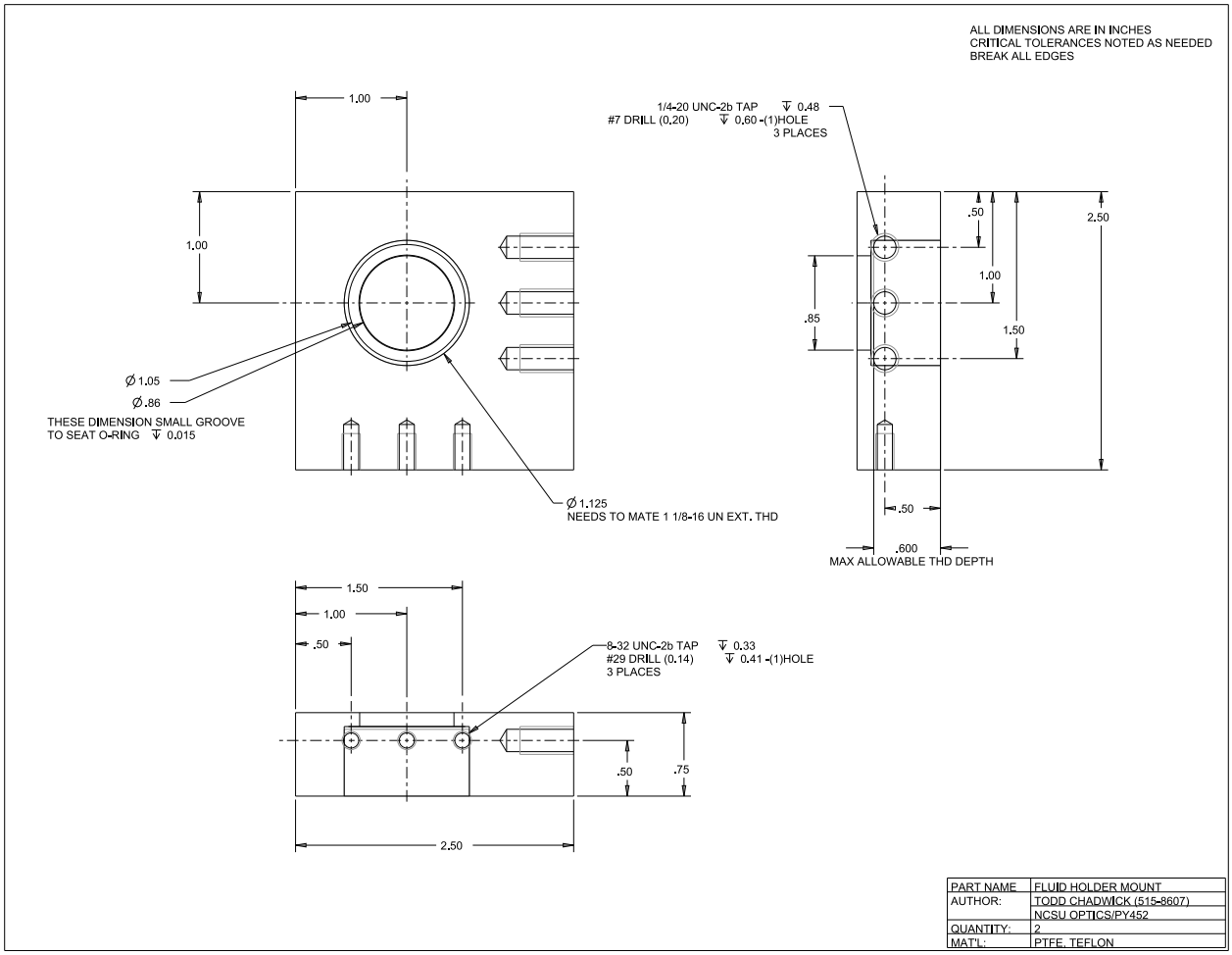
ALL DIMENSIONS ARE IN INCHES
CRITICAL TOLERANCES NOTED AS NEEDED
BREAK ALL EDGES
1.00
1.00
Ø 1.05
Ø .86
THESE DIMENSION SMALL GROOVE
TO SEAT O-RING ↧ 0.015
Ø 1.125
NEEDS TO MATE 1 1/8-16 UN EXT. THD
1/4-20 UNC-2b TAP ↧ 0.48
#7 DRILL (0.20) ↧ 0.60 -(1)HOLE
3 PLACES
.50
2.50
1.00
.85
1.50
.50
.600
MAX ALLOWABLE THD DEPTH
1.50
1.00
.50
8-32 UNC-2b TAP ↧ 0.33
#29 DRILL (0.14) ↧ 0.41 -(1)HOLE
3 PLACES
.50
.75
2.50
PART NAME FLUID HOLDER MOUNT
AUTHOR: TODD CHADWICK (515-8607)
NCSU OPTICS/PY452
QUANTITY: 2
MAT'L: PTFE, TEFLON

ALL DIMENSIONS ARE IN INCHES
CRITICAL TOLERANCES NOTED AS NEEDED
BREAK ALL EDGES

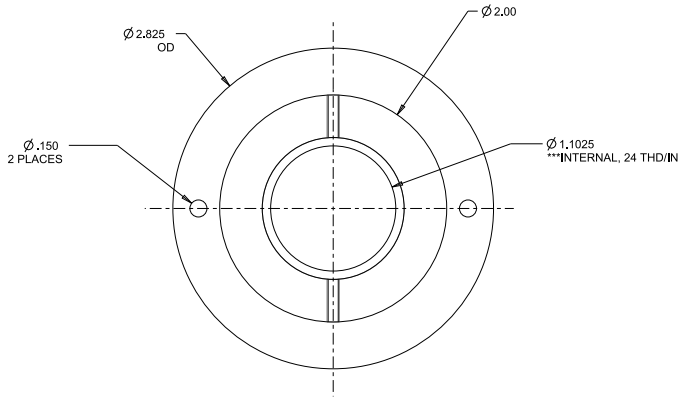

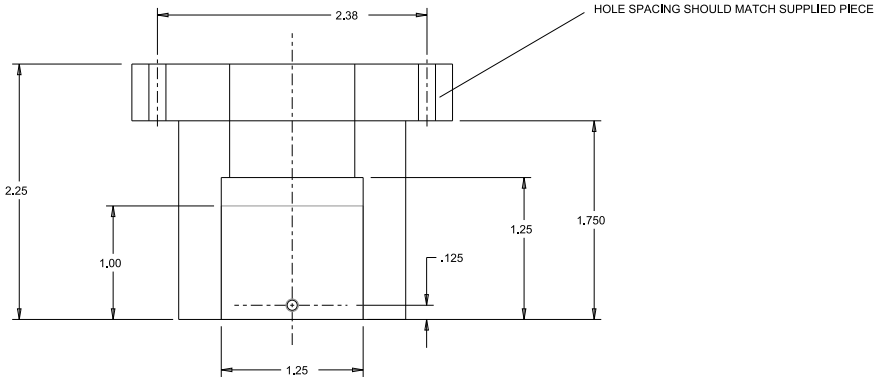

***
PROPER THD NOT KNOWN, SEE SUPPLIED MATING PIECE (INTERNAL)}

INTERNAL SURFACE FINISH: SANDBLAST

PART NAME	SPEX LENS ADAPTER
AUTHOR:	TODD CHADWICK (515-8607)
	NCSU OPTICS/PY452
QUANTITY:	1
MAT'L:	ALUMINUM

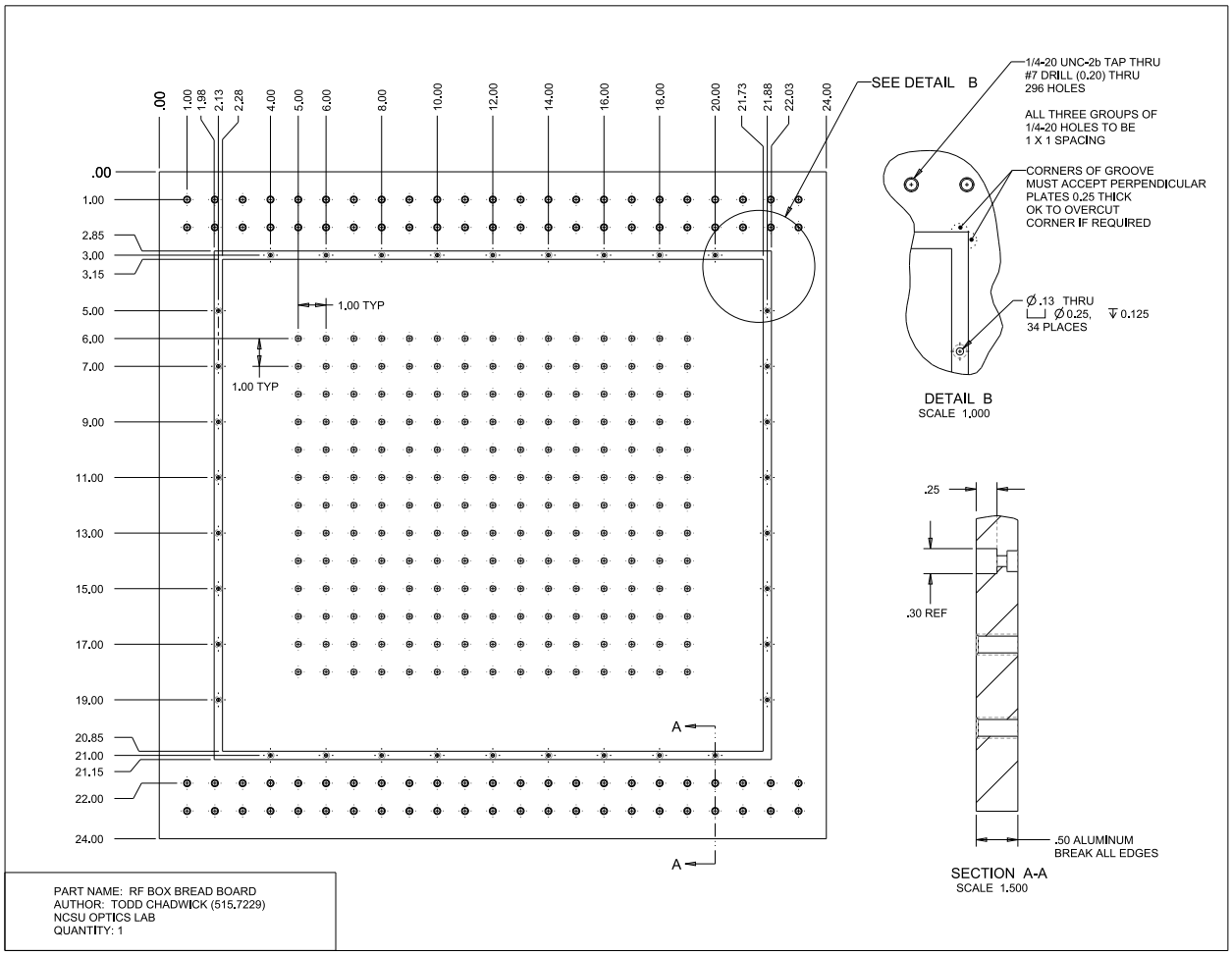
.00
1.00
1.98
2.13
2.28
4.00
5.00
6.00
8.00
10.00
12.00
14.00
16.00
18.00
20.00
21.73
21.88
22.03
24.00
SEE DETAIL B
.00
1.00
2.85
3.00
3.15
5.00
6.00
7.00
9.00
11.00
13.00
15.00
17.00
19.00
20.85
21.00
21.15
22.00
24.00
1.00 TYP
1.00 TYP
A
A
1/4-20 UNC-2b TAP THRU
#7 DRILL (0.20) THRU
296 HOLES
ALL THREE GROUPS OF
1/4-20 HOLES TO BE
1 X 1 SPACING
CORNERS OF GROOVE
MUST ACCEPT PERPENDICULAR
PLATES 0.25 THICK
OK TO OVERCUT
CORNER IF REQUIRED
Ø.13 THRU
⌴ Ø0.25, ↧0.125
34 PLACES
DETAIL B
SCALE 1.000
.25
.30 REF
.50 ALUMINUM
BREAK ALL EDGES
SECTION A-A
SCALE 1.500
PART NAME: RF BOX BREAD BOARD
AUTHOR: TODD CHADWICK (515.7229)
NCSU OPTICS LAB
QUANTITY: 1

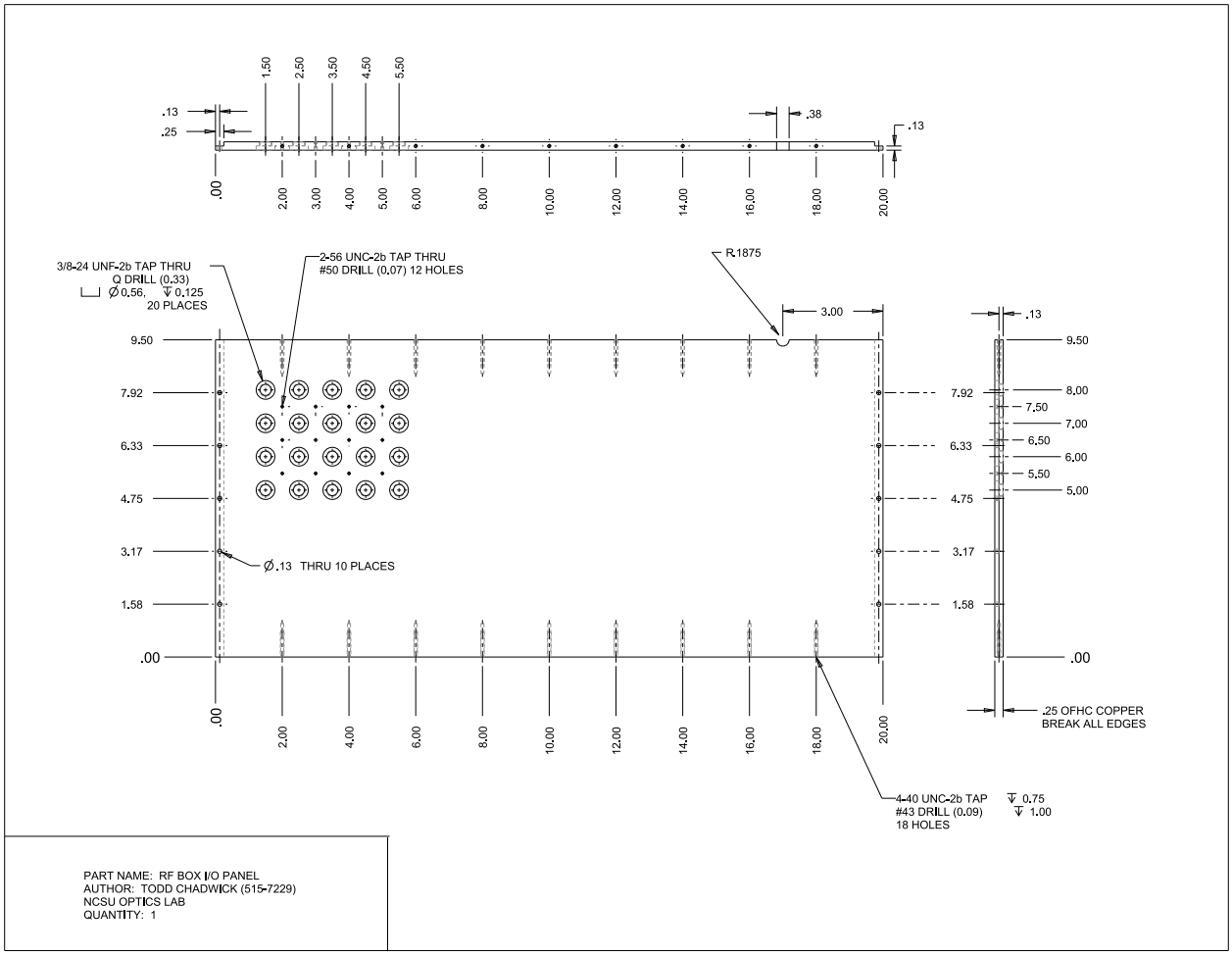
1.50
2.50
3.50
4.50
5.50
.13
.25
.38
.13
.00
2.00
3.00
4.00
5.00
6.00
8.00
10.00
12.00
14.00
16.00
18.00
20.00
3/8-24 UNF-2b TAP THRU
Q DRILL (0.33)
⌴ Ø 0.56, ↧ 0.125
20 PLACES
2-56 UNC-2b TAP THRU
#50 DRILL (0.07) 12 HOLES
R.1875
3.00
.13
9.50
7.92
6.33
4.75
3.17
1.58
.00
Ø.13 THRU 10 PLACES
8.00
7.50
7.00
6.50
6.00
5.50
5.00
.25 OFHC COPPER
BREAK ALL EDGES
4-40 UNC-2b TAP
#43 DRILL (0.09)
18 HOLES
↧ 0.75
↧ 1.00
PART NAME: RF BOX I/O PANEL
AUTHOR: TODD CHADWICK (515-7229)
NCSU OPTICS LAB
QUANTITY: 1

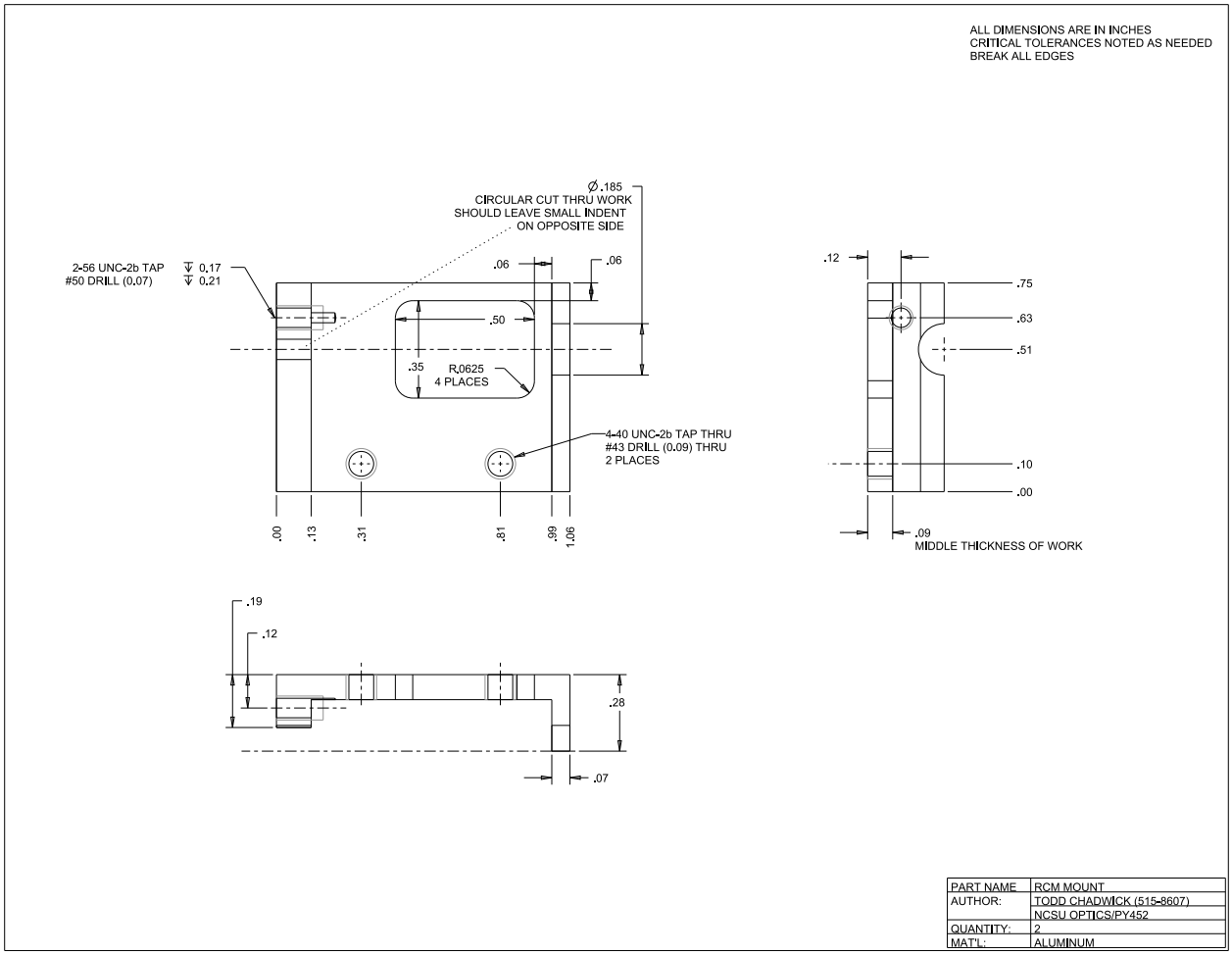
ALL DIMENSIONS ARE IN INCHES
CRITICAL TOLERANCES NOTED AS NEEDED
BREAK ALL EDGES
Ø.185
CIRCULAR CUT THRU WORK
SHOULD LEAVE SMALL INDENT
ON OPPOSITE SIDE
2-56 UNC-2b TAP
#50 DRILL (0.07)
0.17
0.21
.06
.06
.50
.35
R.0625
4 PLACES
4-40 UNC-2b TAP THRU
#43 DRILL (0.09) THRU
2 PLACES
.00
.13
.31
.81
.99
1.06
.12
.75
.63
.51
.10
.00
.09
MIDDLE THICKNESS OF WORK
.19
.12
.28
.07
PART NAME
RCM MOUNT
AUTHOR:
TODD CHADWICK (515-8607)
NCSU OPTICS/PY452
QUANTITY:
2
MAT'L:
ALUMINUM